Available online at www.sciencedirect.com
ScienceDirect
Surface Science Reports 62 (2007) 159–217
surface science reports
www.elsevier.com/locate/surfrep

Multielectron bubbles in helium as a paradigm for studying electrons on surfaces with curvature

J. Tempere[a,b], I.F. Silvera[a], J.T. Devreese[b,*]

[a] *Lyman Laboratory of Physics, Harvard University, Cambridge MA 02138, USA*
[b] *TFVS, Universiteit Antwerpen, Groenenborgerlaan 171, B2020 Antwerpen, Belgium*

Accepted 5 March 2007

Abstract

The study of two-dimensional electronic systems has revealed a host of new and startling phenomena, such as the quantum Hall effect. Although effort has gone into studying the effects of confinement in two-dimensional systems, the effects of surface curvature remain relatively unexplored. Nevertheless, curvature and surface topology are expected to have a profound influence: for example, on a sphere it is not possible to have a non-trivial current field that has no vortex structure in it. The spherical geometry also influences lattices in that topological lattice defects are always present.

In this report, we present results and recent insights into the physics of electrons on spherical surfaces. In particular, we investigate the case of multielectron bubbles. Multielectron bubbles are (micron sized) cavities inside liquid helium, containing electrons that collect in a nanometer thin film on the surface of the bubble and form a spherical two-dimensional electronic system. Different phases are identified and investigated: the electron fluid, the Wigner lattice, and the pair-correlated "superconducting" state. Uniaxial external magnetic fields (normal to the surface at the poles of the sphere, and tangential to the surface at the equator) influence the different phases and give rise to textures on the surface. In discussing the properties of the spherical electron system under various conditions, we identify the differences between flat surfaces and spherical surfaces.

The theoretical framework presented here is focused on the case of electrons on the spherical surface of a bubble in helium. We discuss how the theory can straightforwardly be generalized to investigate the case of (finite thickness) metallic nanoshells. Nanoshells consist of a non-conducting nanograin covered by a few atomic layers of metal. The physiologically compatible size and unique optical properties of these objects have led to applications in diagnostics and directed therapeutics of cancer and drug delivery. These successful biomedical applications underline the increasing interest in curved-surface electron systems treated in this report, and the necessity to supply a theoretical framework for these systems. Multielectron bubbles and nanoshells are structures that are realizable in nature. We begin this report by discussing the experimental developments and progress in producing these entities in a useful manner that allows them to be studied and utilized.

Contents

* Corresponding author. Tel.: +3238202459; fax: +3238202245.
E-mail address: jozef.devreese@ua.ac.be (J.T. Devreese).

0167-5729/$ - see front matter © 2007 Elsevier B.V. All rights reserved.
doi:10.1016/j.surfrep.2007.03.001

1. Introduction

1.1. Overview

In this review we present recent developments in the study of a two-dimensional electron structure on a curved surface. In particular we investigate surfaces that are spherical in static equilibrium. The electrons on this surface are free to move in directions parallel to the surface, but are strongly bound in the directions perpendicular to the surface. On a sphere, this means that the full (three-dimensional) wave function describing such electrons should be factorizable in a function depending only on the angles and a function depending only on the radial distance. The system can be considered two-dimensional if all

the electrons have the same radial dependence of their wave function, and if the energy required to change the radial mode is much larger than the other relevant energy scales involved. If the energy scale is such that several radial modes (be it still a limited number) participate, the system is quasi-two-dimensional.

Flat, two-dimensional systems are realized with electrons on helium and in solid state systems (such as quantum wells or surface layers). Similarly, curved two-dimensional systems can be created both with electrons on helium and with solid state systems. The former case is that of the multielectron bubble in liquid helium, and an example of the latter are metallic nanoshells. In this review we will mostly focus on multielectron bubbles (MEBs), since it is a closer realization of a two-dimensional spherical 2D electron gas, whereas thin nanoshells are better described as quasi-2D systems.

We shall start with a simple qualitative picture of the multielectron bubble and later develop these ideas analytically. The electrons in a multielectron bubble are confined to a narrow shell in space at the surface of the sphere; the electrons form a gas or liquid, free to move along the surface in angular momentum states or localized as a Wigner crystal of electrons. MEBs have a number of fascinating properties. They contain a countable number of electrons, N, and certain properties can have important differences for odd or even numbers, even if N is large. The range of N is of order tens to billions and the spherical radius is of order nanometers to millimeters for this range. The lone single-electron bubble (SEB) in helium is also an important entity and has an experimentally determined diameter of 34.4 Å [1]. The single electron is in an s-state spread out over the volume of the bubble. The large diameter of the SEB is due to the large zero-point energy of the electron, confined or limited in volume by the surface tension of the wall of the confining helium bubble.

In the MEB formed in liquid helium, electrons repel each other due to Coulomb forces; their energy is minimized if they move off to infinity. The liquid helium surface presents a potential barrier of ∼1 eV [2,3], preventing the electrons from entering the liquid. A bubble of helium vapor will collapse to zero radius to minimize surface energy. The energy of the MEB is minimized when the electron Coulomb repulsion and helium surface tension forces are balanced in a spherical bubble with the electrons residing on the surface in a thin layer about a nanometer thick. For 10^4 electrons the classical equilibrium radius, called the Coulomb radius R_C, is about 1.06 microns and scales as $N^{2/3}$. Fig. 1 visualizes an SEB and an MEB in liquid helium.

Waves on a flat helium surface are called ripplons. The surface of an MEB can have both radial and angular deformations; the radial deformations or waves are called spherical ripplons. These deformations were originally studied by Lord Rayleigh [4] for spherical droplets and play an important role in the dynamics and other properties of MEBs. Electrons are in single-particle angular momentum states. For a rigid sphere of radius R, the energy of a single electron confined

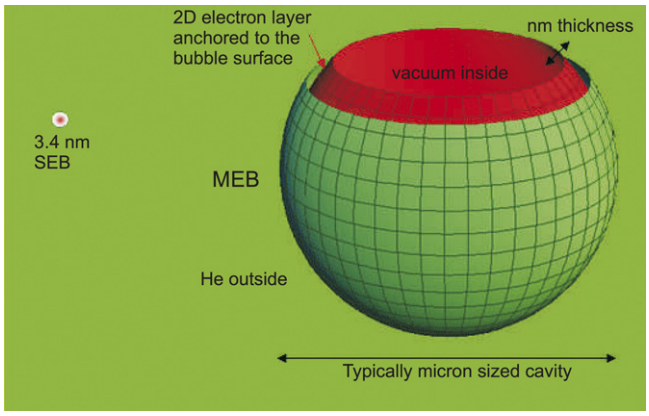

Fig. 1. Schematic representation of a multielectron bubble in liquid helium. The electrons are not smeared out over the entire bubble volume, but form a spherical film on the inner bubble surface.

to the surface is

$$E_\ell = \frac{\hbar^2\,\ell(\ell+1)}{2m_e R^2} \tag{1}$$

where ℓ is the angular momentum, m_e the mass of the electron, and $\hbar$ is Planck's constant. The electrons in the MEB interact with each other, the helium, and the ripplons. Generally, the helium vapor inside of the bubble is ignored and at very low temperatures the helium vapor density becomes negligible. MEBs can be formed in helium I or helium II, i.e., normal or superfluid helium. At the current stage of study, the properties of He II are not involved in the bubble properties and the main advantage of superfluid helium is that a more robust film of helium covers the walls of an enclosing cell. These He walls act as a barrier to the electrons, whereas electrons would rapidly disappear into bare metallic surfaces.

A number of properties of electrons on a spherical surface will be treated in this review. In Chapter 2 (and this chapter) we shall discuss some of the experimental observations, the stability of MEBs and bubble dynamics, as well as other realizations such as metal nanoshells. In Chapter 3 we set up and discuss the formalism for analyzing the Hamiltonian and excitations on a curved, mainly spherical surface. In flat space the Hamiltonian in second quantization is expressed in terms of creation annihilation operators of momentum states. In spherical space the Hamiltonian is expanded in terms of the more complicated creation annihilation operators of the angular momentum states. This formalism will be utilized throughout the remainder of this review. In this chapter we then consider the many-body problem, the dielectric response, plasmons, and magnetic properties, including magnetic ordering due to two-particle electron exchange and the interaction with a magnetic field to form Landau bands. The interaction of electrons with ripplons leads to polarons, which will be treated in Chapter 4, along with considerations of the Wigner lattice of electrons on a sphere. The electron–ripplon interaction is attractive, just as the electron–phonon interaction, which leads to pairing and superconductivity in metals. Chapter 5 treats ripplon mediated pairing and BCS superconductivity in MEBs. This chapter also considers superconducting vortices and superconductivity in

nanoshells. In the remainder of this chapter we present a short historical review and discuss some properties that will be useful in the later chapters.

1.2. Historical

MEBs were first observed by Volodin, Khaikin, and Edel'man in 1977 [5]. Studies of the electron–liquid helium system had already started more than a decade earlier. In 1971 Crandall and Williams [6] noted that electrons at a sufficiently high density should undergo Wigner crystallization [7] on a helium surface, later observed by Grimes and Adams [8]. Electrons could be created using a hot tungsten filament, a field emission tip, or a glow discharge, all at low temperature in a vessel containing liquid helium with a flat liquid surface (with helium covered walls). Using a various electrodes configurations the electrons could be found to dress the surface of the helium [9]. The electrons are attracted to the surface by their image charge. Cole and Cohen [10] calculated the attractive binding energy due to the electron's Coulomb interaction with its image charge. For ^{4}He, with dielectric constant $\varepsilon = 1.057$ at a distance $2z$ between the charge and its image, the potential is

$$V(z) = -\frac{e^2}{4\pi\varepsilon_v}\frac{\varepsilon-1}{\varepsilon+1}\frac{1}{2z}. \tag{2}$$

where ε_v is the vacuum permittivity. The binding energy has a value of $\sim$8 K.

Without an applied electric field the electron surface density is quite low. In order to increase the electron density an electrode with a positive potential could be placed under the helium surface. Already in 1964 Sommer [2] noted that a high electric field would produce a hydrodynamic instability so that the surface charge would be dumped to the submerged electrode. Gor'kov and Chernikova studied the instability theoretically [11]. At high fields the surface of the helium is visibly deformed [9]; an instability develops for a field of $\sim$4000 V/cm and for an electron surface density of $2\times 10^9/\mathrm{cm}^2$. This is the maximum density that can be achieved on a bulk ^{4}He surface. Volodin et al. [5] observed the instability at the values predicted by Gor'kov and Chernikova, observing the formation of MEBs containing $\sim 10^7$ to 10^8 electrons with diameters of 50–300 microns. The smaller MEBs moved to the submerged electrode in less than a millisecond where they were annihilated, while larger bubbles could float back up to the surface in a millisecond. A decade later, Albrecht and Leiderer [12] used high speed video photography to observe bubbles with up to 10^7 electrons. They measured bubble velocities of $\sim$10 cm/s and could observe bubble oscillations and fissioning of the bubbles. In both of these photographic measurements, the bubbles were far from an expected spherical shape due to their rather violent birth and short life, so that they did not have time to relax to their lowest energy shape. To study the equilibrium properties of MEBs in long-lived states, Albrecht and Leiderer suggested trapping them in electromagnetic or acoustic fields, but did not succeed in an attempt with EM fields.

A clear picture of the equilibrium properties of an MEB was developed by Shikin [13]. To calculate the equilibrium radius, the total energy was minimized. The main energy terms are the surface tension of the bubble and the Coulomb repulsion, the first and second terms in Eq. (3), below

$$E_{\mathrm{tot}} = 4\pi R^2\sigma + \frac{N^2e^2}{8\pi\varepsilon_0\varepsilon(R-d)} + \gamma N\frac{\hbar^2}{2m_e d^2} + p\frac{4\pi}{3}R^3 + \text{ exchange terms.} \tag{3}$$

Here R is the radius of the bubble, $\sigma = 3.6\times 10^{-4}$ J/m^2 is the surface tension of helium. The third term is the localization energy, where the electron film is located at a radial distance d. Typically this is of the order of (a few) nanometers; γ is a geometrical factor of order 1. We have include a pV term as the fourth term, with pressure p. The Coulomb repulsion energy is $(Ne)^2/[4\pi\varepsilon_v(R-d)]$. Adding in the polarization energy omitted by Shikin, $(1-\varepsilon)(Ne)^2/[4\pi\varepsilon\varepsilon_v(R-d)]$, yields the second term. The image energy of the electrons, and the exchange energy in the electron film, are omitted. For large bubbles with $p = 0$, the localization energy can be ignored after which $d \ll R$ can be set equal to zero in the Coulomb term. This yields R_C, the Coulomb radius

$$R_C = N^{2/3}\left(\frac{e^2/(4\pi\varepsilon_v)}{16\pi\varepsilon\sigma}\right)^{1/3} = 1.064\left(\frac{N}{10^4}\right)^{2/3}\text{ microns.} \tag{4}$$

The leading correction to the equilibrium radius is

$$R^3 = R_C^3(1+\Delta) \text{ with } \Delta = \frac{4}{3}\left(\frac{\gamma\varepsilon a_0}{4NR_C}\right)^{1/3}. \tag{5}$$

This small correction, an expansion of the bubble, is important for considerations of stability of a charged bubble; here a_0 is the Bohr radius. Minimizing the energy with respect to d, one finds d to be of order a few nanometers. Salomaa and Williams [14] studied the structure of the MEB using density functional theory and found the (radial) width of the density distribution of the electron film to be somewhat smaller.

In addition to the direct Coulomb interaction there is an electron exchange term contributing to the energy that will be important for small bubbles. Shung and Lin [15] studied the effect on MEBs using density functional theory; their results can be accurately represented by

$$E_{\mathrm{exch}} = -0.3176\frac{e^2N^{4/3}}{4\pi\varepsilon_v\varepsilon(R^2d)^{1/3}}. \tag{6}$$

This leads to about a 1% reduction in R_C for small bubbles. Artem'ev, Khrapak, and Yakubov [16] have refined Shikin's theory with a more fully quantum mechanical approach and find that the bubble radius is reduced from the Coulomb radius.

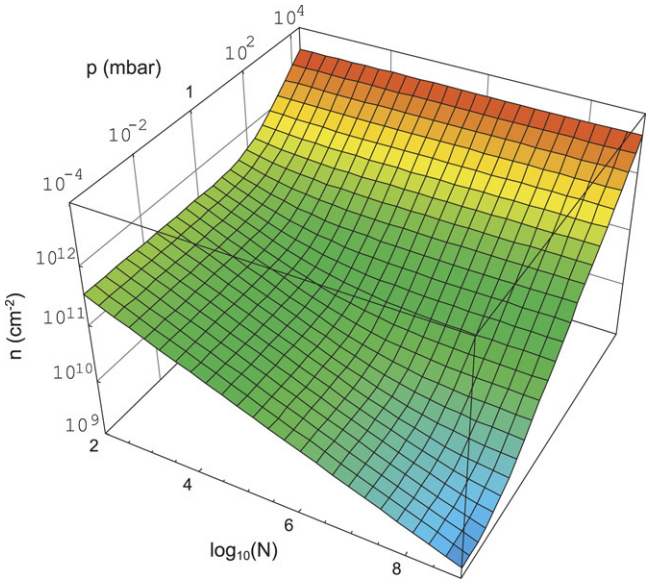

Fig. 2. The surface density of MEBs as a function of pressure p and number of electrons N. The maximum pressure taken is ∼25 bar, where helium solidifies.

1.3. Surface density tunability

Here in this introduction we discuss a few more properties of MEBs that will be useful in the later chapters. One of the important properties of the MEB is that it can have an enormous range of electron surface density. At zero pressure we have

$$n_s = \frac{N}{4\pi R_C^2} = 1.514 \times 10^{12} N^{-1/3}\ \mathrm{cm}^{-2}.$$

For MEBs with N varying from 10^2 to 10^9 electrons, this results in surface electron densities of 3.25×10^{13} to 1.51×10^9 cm^{-2}, varying by more than four orders of magnitude. Exchange corrections should be taken into account when the number of electrons is below 10^3. The result is a reduction of the density (and an increase of the radius) for these small bubbles. When pressure is applied [17], the equilibrium density is found by minimizing Eq. (3) (including Eq. (6)). Results are shown in Fig. 2.

The bubbles are also highly compressible as shown by Tempere, Silvera, and Devreese [17]. In Fig. 3 we show the variation of the bubble radius with pressure for several values of N. Here the pressure can take on small negative values until the bubble explodes. Negative pressures up to ∼9 bar can be achieved in helium [18].

One of the driving motivations for studying the electron–helium system has been the observation of the Wigner crystal or more specifically, the melting line between the electron liquid and the two-dimensional electron solid. In two dimensions on a flat surface, electrons crystallize in a hexagonal (triangular) lattice. Melting is qualitatively different in 2D than in 3D, thus there has been a great theoretical and experimental effort to understand this system. There are two regimes of melting: the classical and the quantum regimes [19,20]. The transition region is usually characterized by the plasma parameter Γ, the ratio of the potential energy to the kinetic energy. A 2D gas or

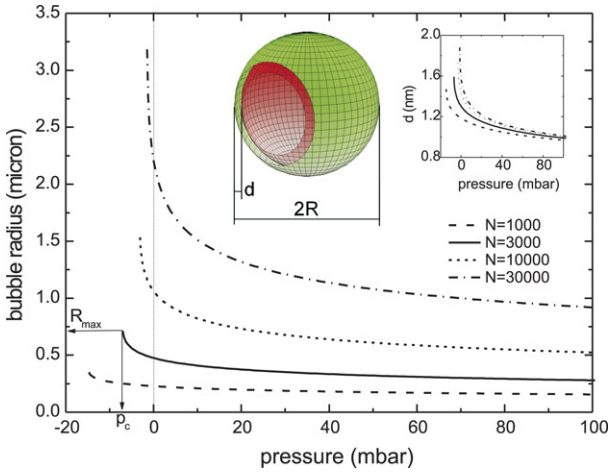

Fig. 3. The variation of a bubble's radius for modest pressures up to 100 mbar, including negative pressures. Negative pressures can provide stability to the bubble as will be discussed in Chapter 2. The inset shows the variation of d as a function of pressure.

liquid has a small plasma parameter and the more correlated liquid or solid, a large value, $\Gamma > 100$.

The localizing potential for the Wigner solid is the Coulomb potential, $\langle V\rangle = \mathrm{e}^2/r_0 = \mathrm{e}^2\pi^{1/2}n_s^{1/2}$, while in the classical regime the kinetic energy is $k_\mathrm{B}T$, so

$$\Gamma_{cl} = \mathrm{e}^2\pi^{1/2}n_s^{1/2}/(k_\mathrm{B}T). \tag{7}$$

The conditions are often given in terms of $r_s = r_0/a_0$, the ratio of a radius of an area containing 1 electron, $r_0 = 1/\sqrt{\pi n_s}$, to the Bohr radius a_0. At 1 K with $n_s = 10^9$ cm^{-2} the calculated value of the plasma parameter is 94. In the experimentally observed melting line of the Wigner lattice on a flat surface, Grimes and Adams [8] found $\Gamma = 135 \pm 15$. A number of experimental measurements scatter around this value [21]. In the classical regime, as the density is increased the melting temperature increases.

In the quantum regime for a 2DEG the kinetic energy at $T = 0$ is $\langle K\rangle = \pi\hbar^2 n_s/m_\mathrm{e}$, so that

$$\Gamma_\mathrm{quant} = \frac{m_\mathrm{e}\mathrm{e}^2}{\pi^{1/2}\hbar^2 n_s} = 1/(a_0 n_s^{1/2}).$$

As n_s increases at low temperature a transition is made to the quantum regime. With increasing n_s the melting temperature decreases until the solid melts at zero kelvins.

Quantum melting is well known in 3D, with the example of helium where the zero-point motion of the atoms is so large that liquid helium, in equilibrium with its vapor pressure, remains a liquid to $T = 0$ K and only solidifies under a pressure of ∼25 bar. This is often discussed in terms of a quantum Lindemann melting criterion, that the solid melts when the rms deviation of an atom relative to the lattice constant r_0,

$$\delta = \sqrt{|\mathbf{r} - \mathbf{r}_0|^2}/r_0 \tag{8}$$

exceeds a critical value of 0.1–0.3. In an infinite 2D system δ diverges; however in a finite system such as a bubble the infrared divergence in no longer present. Bedanov et al. [22]

introduced a modification of this criterion (also valid for infinite 2D systems) that considers fluctuations of the average distance between neighbors, and performed a simulation to find 0.3 for quantum melting in 2D. Thus, as the electron density increases, the rms deviation increases until the lattice melts.

If we set $\Gamma_{\text{quant}} = 137$, we find $n_s = 6 \times 10^{11}$ cm^{-2}; this corresponds to the density at which the melting temperature goes to $T = 0$ K, or quantum melting. After the observation of the Wigner lattice on a flat surface in the classical regime, efforts were made to observe quantum melting. These were thwarted by the surface instability for high coverage, limiting the density to $\sim 2 \times 10^9$ cm^{-2}. However, the MEB was born of this instability and it can have very high surface coverages. Wigner crystallization and quantum melting are transitions that can be attained and studied on the MEB.

The criterion or condition for quantum melting of the Wigner crystal is different for the flat surface and the spherical surface. Not only are they different, but localization of the electrons can occur due to different mechanisms. In a curved 2D electron gas, the Coulomb interactions give rise not only to a mean-field electric field confining an electron laterally, but also to a pressing field. The Coulomb energy per particle $\langle V \rangle = N\mathrm{e}^2/(8\pi\varepsilon_v\varepsilon R_C)$ depends on N and on R, affecting the relevant plasma parameter for melting in a non-trivial way. The plasma parameter will increase as R_C is decreased (either by decreasing the number of electrons in the bubble, or by increasing the pressure), so that a quantum melting transition can be expected when the bubble is compressed. However, as R_C is decreased the pressing field is increased, favoring again a localization and the Wigner lattice. When the pressing field is strong enough the resulting electron–ripplon leads to the formation of a Wigner lattice of ripplonic polarons, distinct from the Coulombic Wigner lattice.

In Chapter 4 a variational model is introduced to describe the melting of the ripplopolaronic lattice, and to derive the phase diagram for the ripplopolaron Wigner lattice. This scheme can be extrapolated to the region where the Coulomb interaction dominates the electron–ripplon interaction, in an attempt to find also the phase transition line for the Coulombic Wigner lattice on the sphere. However, a point to note is that when the Coulomb interaction dominates over the electron–ripplon interaction the variational model of Chapter 4 which is geared towards the ripplopolarons will not be a suitable variational trial model. Indeed, when the electron–ripplon model system is used to estimate the density at which quantum melting occurs in a bubble at $p = 0$, with Lindemann criterion $\delta = 0.13$, a critical density $\sim 10^9$ is found, much lower than the flat-surface critical density of $\sim 10^{11}$ cm^{-2}. The motivation for this particular choice of the Lindemann criterion will be discussed in Section 4.4.3. The melting line of the Coulombic Wigner lattice depends strongly on the Lindemann criterion in this scheme — the critical density in this model can be increased up to 10^{11} cm^{-2} by using a Lindemann criterion of $\delta \approx 0.23$. An observation of quantum melting, through capacitance spectroscopy of lattice phonons, as in the original experiment of Grimes and Adams [8], is still lacking for spherical systems, as is an experimental estimate of δ for these systems.

2. Physical realizations of curved 2D electron systems

2.1. Multielectron bubbles in liquid helium

What are the states and shapes of multielectron bubbles and their properties? Can MEBs be prepared in long-lived equilibrium states and studied to understand their properties? Under what conditions do we expect an MEB to be stable in liquid helium? How can MEBs be observed? What is the response of an MEB to a pressure shock? What are other realizations of electrons confined to a curved surface? Answers to these questions will be discussed in this chapter.

In the following chapters we shall discuss the possible phases of MEBs, which may depend on subtle values in the interaction energies, bubble size, pressure, and temperature. On the one hand, in all of our considerations we consider the electrons to be in a single layer confined to the surface of the bubble; that is, there is no layering of the electrons. For an electron density $\sim 10^{10}$ cm^{-2} the average spacing between electrons is very large, $\sim$50 nm. On the other hand, if very high densities could be achieved, the electrons might achieve a lower energy by layering, as observed in simulations of electrons confined on a flat surface by a hard wall [23].

2.1.1. Equilibrium structures and observations

As was discussed in the previous chapter the MEB in equilibrium in a gravity free region is expected from energy considerations to be spherical and have a radius given by Eq. (4) for the Coulomb radius, ignoring smaller terms. If the diameter of the MEB is larger than the wavelength of optical light one can make an image and study the bubble visually. Since liquid helium has an index of refraction of about 1.03 and the interior of the bubble is vacuum (or a very low density of He gas) with index of refraction 1, there is sufficient contrast of the light due to refraction and reflection to form an image. Smaller bubbles should also be detectable and quantitative data could be obtained, for example, by light scattering or measurement of charge. If the bubble is in a gravitational field then this potential will distort it from spherical symmetry if the potential is comparable to the surface tension energy. Shikin [13] has shown that gravity tends to flatten the bubble unless the radius satisfies

$$R \leqslant \sqrt{3\sigma/\rho g} \sim 10\,\mu\text{m}$$

where ρ is the helium density and $g = 9.81$ m/s^2. A second deformational effect can occur if the bubble is sessile, i.e. due to buoyancy the bubble is pushed up against a surface, deforming at the interface. In the following we shall continue to consider the bubble as spherical. There are also local deformations due to dimpling under the electrons. On a flat surface the bound electrons are about $\sim$100 Å from the surface. The attraction of an electron by its image force, or aided by an external electric field leads to a local deformation of the lattice under the electron. However, in the absence of external fields the depth of the dimple is only $\sim 10^{-2}$ Å [24]. In an MEB the electron not only feels its image force, but the Coulomb force of the electric field due to all of the other electrons, directed into the surface.

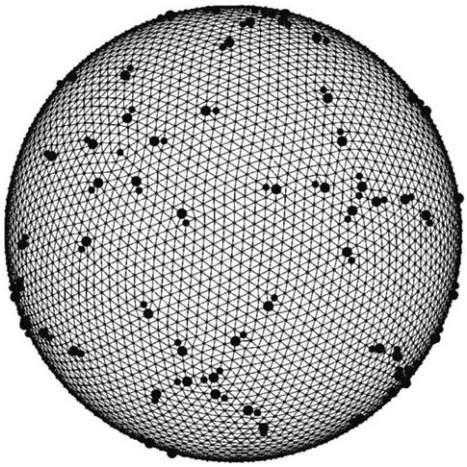

Fig. 4. The classical Wigner lattice on a spherical surface. Locally the lattice is triangular with each electron having six neighbors. The 5 and 7 neighbor defects are shown by dark spots. From Ref. [25].

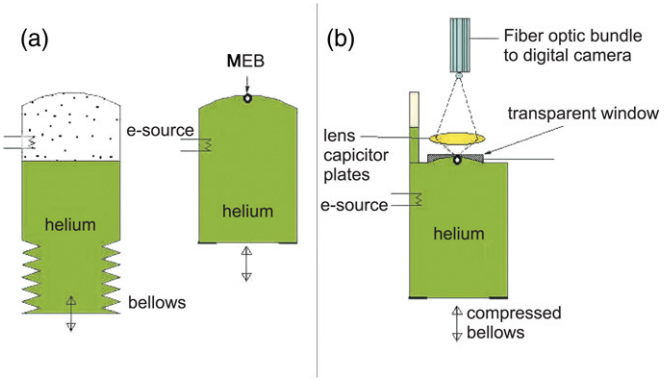

Fig. 5. A schematic of a cell for producing long-lived MEBs, described in the text. In (b) a fiber optic for illuminating the MEB from below is not shown.

This electric field can be very significant, $\sim 10^5$ V/cm, and lead to deep dimpling of the surface under the electron.

One of the important phases and areas of study of the MEB may be the Wigner lattice and quantum melting. The ground state triangular Wigner lattice of the flat surface should be the lowest energy structure for a large diameter bubble. However, the hexagonal lattice does not map onto a spherical surface. In the perfect lattice each electron has six neighbors; to fit on the spherical surface there must be defects with 5 or 7 nearest neighbors, existing in the ground state. Due to topological constraints, there has to be an excess of twelve 5-fold defects. Additional defects occur in pairs of 5- and 7-defects. These defects can be locally bound to each other; or the 5- and 7-defects can unbind. Correspondingly, additional nematic phases can be identified in the Wigner lattice state [25, 26]. A visualization of the nematic phase is shown in Fig. 4. In Chapter 4 we shall discuss this and a new mechanism due to the electron–ripplon polaron that leads to Wigner localization of the electrons onto a lattice, with deep dimples under each electron.

One of the important questions concerning MEBs is "can they be experimentally produced in long-lived states so that they can be studied in detail?" We have already seen that MEBs can be made by an instability in a flat surface in which millions of electrons are subsumed in a bubble. However, the MEB made in this manner only exists for milliseconds and is in a highly deformed excited state due to its violent chaotic creation and has no time to relax to its ground state before annihilation occurs. There have been no extended attempts to produce and trap MEBs with electromagnetic or acoustic fields.

An experimental effort is underway by collaborators of this review, following a proposal for a new approach for producing an MEB in a stable long-lived state [27]. The geometry is shown in Fig. 5. A cylindrical cell with a dome shaped roof is partially filled with liquid helium in the superfluid phase. A source of electrons, either a field emission tip or a tungsten filament, is in the vapor phase region and can be actuated to load the cell with electrons. Since the helium is superfluid, a reasonably robust film of helium covers all surfaces above the bulk liquid helium. This is very important because if a metallic surface is locally denuded of helium, the electrons can enter the metal and exit the vapor region of the cell. The helium film thickness is $d_f = \sqrt{\alpha/(\rho g h)}$ (where α is the Van der Waals coefficient, ρ is the helium density, and h is the height above the bulk helium surface) is of the order a few hundred angstroms thick, depending on h and α. Although the equilibrium state of a chamber with any bulk liquid and a vapor phase region should have a film coverage, the surfaces are usually denuded. For normal fluids with gas phase density or rate of evaporation depending exponentially on temperature, small thermal fluctuations of the surface lead to evaporation of the film and its local destruction. For superfluid helium, a film flows to warmer areas and thus levels out thermal gradients to maintain a uniform chemical potential. The film is particularly robust at subkelvin temperatures when the vapor pressure is low. As a consequence of the bulk helium, the film on all surfaces, and the barrier for helium to enter the liquid through the surface, the electrons are confined to the surfaces and the vapor phase. The cell is designed with a mechanism for raising or lowering the helium surface, shown schematically in the figure as a bellows. As the helium level is raised the electrons are confined to an ever-decreasing volume. When the level reaches the top of the dome, the volume containing the electrons form a minimum energy surface, or a sessile MEB that in principle should be in a long-lived state that can be studied by various techniques. Raising the liquid helium level above the top of the dome hydrostatically pressurizes the MEB by the liquid pressure head. By making the dome transparent (i.e., a concave lens) the bubble can be illuminated and imaged. One implementation is to use a low temperature microscope and image the bubble on a coherent fiber optic to transfer the image out of the cryostat. A number of other possibilities exist for studying properties of the bubble, but these will not be discussed here.

This new approach has been implemented and at this writing has not produced MEBs localized in the top of the dome. Very large bubbles with diameters >1 mm, containing billions of electrons have been produced and viewed for times ~ 1 s, but these move across the field of view and are not localized in the top of the dome, as expected. Furthermore, if the helium level is lowered and again raised the bubble is not seen. A possible explanation will be discussed ahead.

2.1.2. Stability with respect to electron tunneling

We first discuss the stability of electrons in a cell with bulk liquid helium and walls covered by a superfluid film. The primary question is whether the electrons produced in a cell surrounded by helium surfaces remain on the surface or in the vapor phase, or escape into the underlying walls. A number of studies discuss the rapid or slow decay of the electron density in such a cell. Sommer [2] reported that when electrons are produced in the vapor phase, and an electrode (with a potential negative relative to an electrode above in the vapor phase) initially covered by bulk helium was exposed to the vapor phase, a negative current pulse was observed and the electrons disappeared from the cell. If the voltage difference was reduced to zero and then turned back on, there was no pulse, implying that the electrons had already disappeared. In most experiments a submerged electrode with a positive potential is used to hold electrons on a surface; this charged surface is very stable. Brown and Grimes [28] reported stability of the electrons in their cell; if the holding field was lowered to release electrons and raised again, they would recover approximately the same electron density. Etz et al. [29] directly studied the stability of electrons on a flat surface, either dielectric or conducting, covered with a superfluid film whose thickness could be measured by ellipsometry. The helium surface could be charged with electrons held by an electric field and the charge density measured as a function of time, after turning off the electron source. The surface charge slowly decayed. When the holding potential was turned off so that the electrons on the helium should leave, a residual charge of order 10^{11} cm^{-2} remained if the surface was a dielectric. This was interpreted as electrons that had penetrated the He film, by tunneling. The helium film was thinned due to the image forces of the electrons attracted to the substrate, by about a factor of 2 for insulating substrates and 5 for conducting substrates. The film thickness when charged was about 100 Å. This seems to be too thick for electrons to tunnel through, but tunneling could occur at rough regions where the helium might be thinned [30]. Electrons become trapped on the dielectric substrates but flow away when the substrate is conducting. These measurements provide interesting insight into the behavior and distribution of electrons in a cell made of conducting and insulating materials filled with bulk helium, a film, and a vapor phase.

We now consider the thinning of films above an MEB such as in Fig. 6. If the film becomes very thin then the electrons can tunnel into the surface and rapidly deflate or annihilate the MEB. An interesting property for dielectric surfaces, also observed for flat surfaces, is that the tunneling and trapping of electrons in the surface is limited as the trapped electrons repel surface electrons on the helium; this is not the case for conducting surfaces.

For a sessile MEB there are three forces that affect the thickness of the helium film above it: the image force, as considered for a flat surface, the polarization force (due to replacing a sphere of helium atoms by a void), and the buoyancy force. To determine the film thickness we shall write down the energy and minimize it with respect to thickness. Consider the

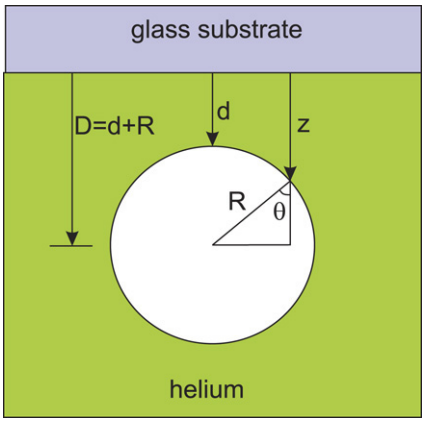

Fig. 6. A sessile bubble in helium. Various dimensions are defined in this figure for the theoretical determination of the film thickness.

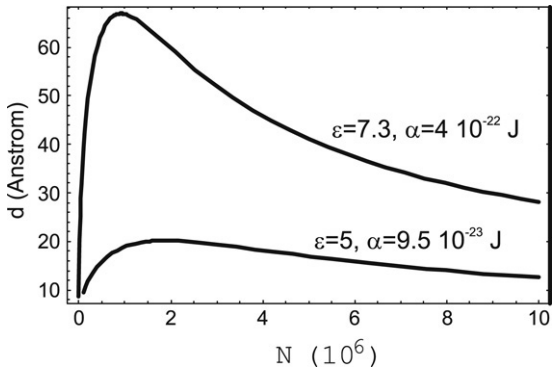

Fig. 7. Thickness of the film above a sessile bubble, for two types of glass characterized by a different ε and α. To allow for electron tunneling out into the wall, the film thickness should be 10 Å or less.

geometry of Fig. 6, where d is the thickness of the film on an insulating surface.

The depth of the bubble center is $d + R$, where we ignore the thickness of the 2DEG. The image potential for an electron at orthogonal distance z from the surface is $-\lambda/z$ with

$$\lambda = \frac{e^2}{4\pi\varepsilon_v}\frac{\varepsilon-1}{\varepsilon+1}\frac{1}{2} \tag{9}$$

for a dielectric surface as seen from (2); and $\lambda = e^2/(8\pi\varepsilon_v)$ for a conducting surface. The potential energy of the image charges is

$$\begin{aligned} V_{\text{image}} &= -R^2\int_0^{\pi} d\theta \int_0^{2\pi} d\phi \sin\theta \frac{n_s\lambda}{D+R\cos\theta} \\ &= 2\pi R n_s \lambda \log\left(\frac{D+R}{D-R}\right). \end{aligned} \tag{10}$$

The polarization energy is the increase of energy that occurs because the bubble volume is vacuum rather than helium. If α is the Van der Waals coefficient (9.5×10^{-23} for He on glass), then

$$\begin{aligned} V_{vdw} &= -\int_0^{R} dr \int_0^{\pi} d\theta \int_0^{2\pi} d\phi r^2 \sin\theta \frac{\alpha}{(D+r\cos\theta)^3} \\ &= \pi\alpha\left[\frac{1}{(D/R)^2-1} + \log\left(\frac{D+R}{D-R}\right)\right]. \end{aligned} \tag{11}$$

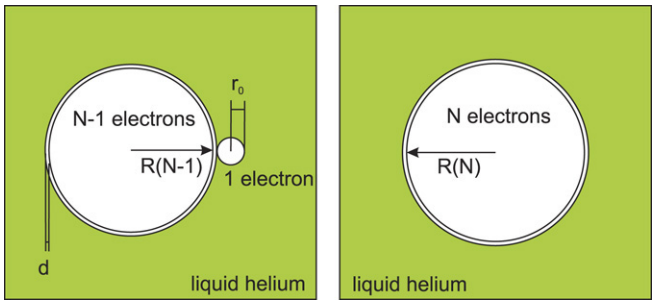

Fig. 8. The configuration for calculating the stability of an N electron MEB against boil-off of a single electron.

The third term is the buoyancy, important for large bubbles,

$$V_{\text{buoy}} = \frac{4\pi}{3} R^3 \rho g D. \tag{12}$$

The total energy $V_{\text{image}}+V_{vdw}+V_{\text{buoy}}$ is minimized with respect to d, the film thickness above the sessile bubble. Both buoyancy and image charges pull the bubble towards the wall, whereas the Van der Waals attraction between helium atoms and the wall tends to push the bubble away from the wall. The resulting equilibrium distance is shown in Fig. 7. There is a bubble size of roughly 1–2 million electrons where the film thickness is maximal. Typically, it is more than 10 Å, which should prevent electron tunneling through the film.

2.1.3. Stability with respect to electron boil-off

Is a multielectron bubble stable? We first note that a bubble can lower its energy by splitting in two. From Eq. (3) the energy of a $p = 0$ bubble behaves as $E_{\text{tot}} \propto N^{4/3}$. If a bubble splits up into two bubbles, each with $N/2$ electrons, then the energy is lowered to $0.79E_{\text{tot}}$ for infinite separation, or the MEB is at best metastable. Dexter and Fowler [31] performed a quantum mechanical study and found that the two-electron bubble should be unstable against decay to two single-electron bubbles by ~0.5 eV in energy. By fissioning, the reduction in Coulomb repulsion energy more than offsets increased surface area energy [32].

One can now extend this to larger N and ask if an MEB is unstable to single-electron boil-off. Salomaa and Williams [33] first considered this problem with a semi-classical model and found the transition to stability for $N \simeq 15$. Silvera, Blanchfield, and Tempere [34] reconsidered this problem including exchange and other factors and found the crossover to stability at $N \simeq 100$. The energy for the N electron bubble is given by Eq. (3), including the exchange, Eq. (6).

For the configuration on the left in Fig. 8, with an $N-1$ electron MEB, there is an additional term due to the repulsion of the $N-1$ electron bubble and the single-electron bubble $(N-1)e^2/(2\varepsilon(R_{N-1}-r_0))$ where r_0 is the radius of the SEB, while the energy of the SEB is $4\pi r_0^2\sigma + \hbar^2/(2mr_0^2) + p(4\pi r_0^3/3)$. The difference in energy of these two configurations changes sign for 100 electrons (at zero pressure) indicating a transition to stability.

When pressure is taken into account the interesting phase diagram shown in Fig. 9 is found. Increasing the pressure destabilizes the MEB, moving the crossover to stability to larger N. Liquid helium can support a negative pressure [35]. As shall be discussed ahead, a negative pressure can stabilize an MEB against splitting in two, and here it also increases the stability to smaller N. However, if the pressure is made too negative the MEB radius explodes, the critical pressure depending on the radius, or N. The results including this second boundary for stability are shown in Fig. 9. We point out that the analysis does not consider the possibility of a potential barrier that could inhibit single electron boil-off.

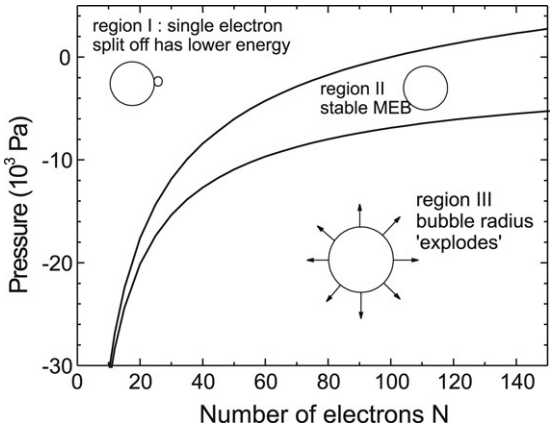

Fig. 9. The phase diagram for stability against single-electron split-off of an MEB. Here the stability fields are plotted as a function of pressure and N.

2.1.4. Deformation instability

The instability of a spherical drop with a charged surface was studied by Lord Rayleigh [4]; Shikin [24] pointed out that R_C is the radius of instability. The instability is a result of the competition between the surface tension that is minimized by having a spherical surface and the Coulomb repulsion, which lowers its energy if the bubble undergoes an angular deformation to an ellipsoidal shape that grows until the bubble fissions in two. (Recall, after Eq. (4), that in Shikin's approximation the radius is slightly larger than R_C, which might be important for stability, whereas Artem'ev et al. found a reduction from R_C).

We shall show in Section 4 that frequencies of the angular modes (spherical ripplons) can be calculated in the harmonic approximation by expanding the deformations in spherical harmonics, $Y_{\ell m}(\Omega)$. Tempere, Silvera, and Devreese [17] calculated the frequencies of these modes, including the effect of pressure. These modes have frequencies characterized by the angular momentum quantum numbers $\{\ell, m\}$ and are degenerate in m,

$$\omega_r(\ell) = \sqrt{\frac{1}{M_\ell}\left[\sigma(\ell^2+\ell+1) + 2pR_C - \frac{(Ne)^2}{4\pi\varepsilon R_C}\ell\right]} \tag{13}$$

where $M_\ell = \rho R_C^3/(\ell+1)$ is a mass term. Evaluating the $\ell = 2$ quadrupole ripplon mode gives frequency 0, or there is no restoring force for this mode. Tempere et al. pointed out that a small negative pressure stabilizes the bubble; this results in a finite restoring force or frequency (the bubble radius expands to be greater than R_C). However, as the pressure increases

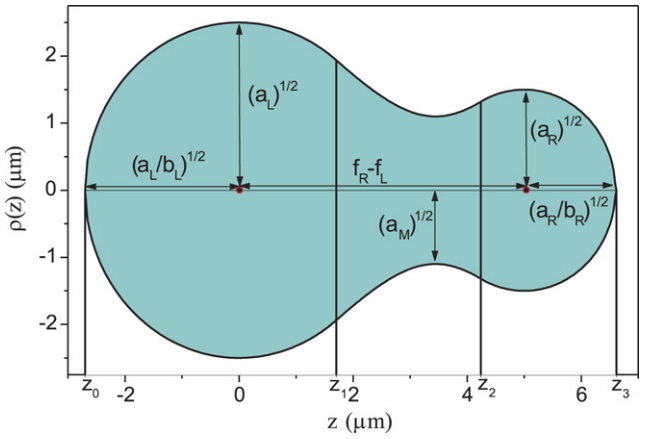

Fig. 10. A generalized shape composed of spheroids and hyperboloids to describe the fissioning of an MEB in cylindrical coordinates. The parameters a_i and b_i are the squares of the semi-major axes and the deformation parameter, respectively; the f_i define the centers of the spheroids.

the mode frequencies for $\ell > 2$ are sequentially driven to zero, the pressure for each mode instability depending on R_C (see Fig. 29, ahead in Chapter 4). Thus, in this approximation pressure can both stabilize and destabilize the bubble.

Earlier, Salomaa and Williams [14] considered the bubble at zero pressure and found a window of stability due to the coupling between the ripplon modes and the radial oscillation modes of the bubble, solving the Rayleigh–Plesset equations for the bubble dynamics. (These equations will be shown ahead). This results in a time averaged radius that is larger than R_C, depending on the oscillation amplitudes of the modes, and thus a finite restoring force to stabilize the bubble. If $R(t)$ grows larger than ∼6% of the equilibrium value the MEB becomes unstable and the amplitude of the $Y_{\ell m}$ mode grows without limit. Hannahs, Williams, and Salomaa [36] extended this analysis and found that although the $\ell = 2$ mode has a region of stabilization, with this non-linear coupling the $\ell = 3$ becomes unstable first, at a lower value of the mode amplitude.

The above discussion of instability considers the small amplitude normal modes of oscillation of the bubble and their coupling. The Bohr–Wheeler model [37] was developed to describe the fissioning of nuclei, treated as charged liquid drops. This model, whose validity is not limited to small amplitude oscillations was applied to MEBs by Tempere, Silvera, and Devreese [38] and overcomes limitations of the harmonic approximation and the Rayleigh–Plesset approach. Amongst other important results, the model shows that for zero pressure there is an energy barrier that stabilizes the MEB from bifurcation. This barrier arises from the increase of surface energy and Coulomb repulsion that accrues as a bubble is deformed from an ellipsoidal shape to two spherical bubbles.

A generalized surface, shown in Fig. 10, can be described by three quadratic forms, two spheroids connected by a hyperboloid. This corresponds to a limited number of variational parameters describing the surface. The total energy consisting of the surface tension, the pressure term, and the electrostatic term (ignoring exchange and smaller quantum localization terms) $E_{\text{tot}} = \sigma S + pV + E_C$ can be written in terms of the generalized surface S and the volume V. The

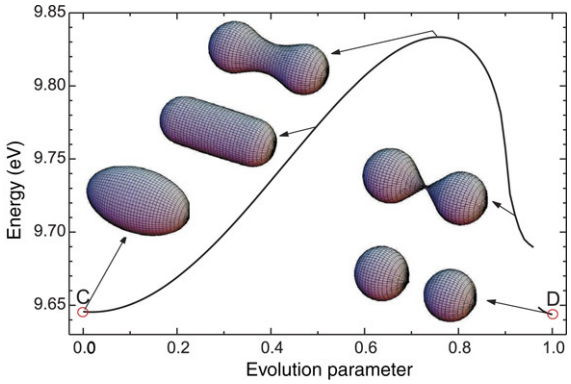

Fig. 11. The energy as a function of an interpolation parameter that traces out a trajectory starting with 0 for a distorted but unsplit bubble and ending at 1 when the bubble is split. This is for an MEB with 10^4 electrons.

energy is then minimized as a function of shape for a given elongation $d_e = z_3 - z_0$ starting with an equilibrium bubble diameter for N electrons, $z_3 - z_0 = 2R_C$. The 11 variables defined in the figure are reduced in number by constraints, such as continuity, fixing the origin, etc.; the volume and surface area are unconstrained and the surface density of electrons is homogeneous and maintained as N/S.

The stability of MEBs was studied as a function of pressure. The result of minimization procedure for zero pressure is shown in Fig. 11 for a bubble with 10^4 electrons. For small deformations there is no barrier, but as the deformation increases a barrier height 0.2 eV/electron develops. From a normal mode point of view, the necking down that is required for the splitting of the bubble requires higher ℓ modes and these are more energetic, giving rise to the barrier. Splintering into more than two pieces would involve an even higher barrier and be much less likely.

For negative pressures the barrier remains but there is a finite restoring force for small distortions. For positive pressure the barrier against bifurcation is suppressed, so that the bubble should be unstable. Recall that pressure drives the higher ℓ modes to zero frequency. In this case the deformation involves both $\ell = 2$ and 3 modes with mode 3 being driven to zero at a pressure of 3 mbar for 10^4 electrons. (Modes are driven to zero at the pressure $p = \sigma(\ell^2 - 2)/(2R_C)$). Thus, the deformation in terms of these modes does not require high energy and at a certain pressure the barrier is suppressed. When the pressure is raised to make a bubble with N electrons unstable, the resulting fission products with $N/2$ electrons may still be metastable since the critical pressure for driving a mode to zero increases as the bubble radius decreases. To fission the daughter fragments the pressure needs to be raised further. One might expect that with increasing pressure MEBs will break up into smaller and smaller bubbles, that is a froth of bubbles. If a froth is produced and the pressure then released or even made negative, it is not expected that the froth will coalesce into a large bubble again, as there will be a barrier preventing this.

We summarize the results. An MEB at zero pressure should be stable. Negative pressures increase the stability until the radius explodes. Positive pressures lead to bifurcation; the smaller the bubble the higher the pressure required for splitting.

It would be extremely interesting to experimentally test these conclusions.

2.1.5. Dynamics of the bubble surface

At this point in the discussion we consider the affect of an external force driving the MEB and its response. One can consider various external probes: electromagnetic, acoustic, or pressure. Actually an acoustic wave in helium corresponds to a time varying pressure. Here we consider the response of the bubble to a pressure step [39]; we consider the affect on both a spherical and an angularly deformed bubble. If $pR_b/\sigma \gg 1$ (where R_b is the pressurized bubble radius), then the R_b scales as $p^{-1/4}$, which follows from the equilibrium equation

$$\frac{(eN)^2}{4\pi\varepsilon R_b^3} = 2pR_b + 4\sigma. \tag{14}$$

The result is that the highly compressible MEB undergoes a collapse from a pressure step, or a large rapid reduction in radius, followed by re-expansion and high frequency oscillations. The oscillations also correspond to large accelerations of the electrons that result in pulses of electromagnetic radiation or sonoluminescence. Under certain conditions the bubble becomes unstable after collapse and the deformation amplitude rapidly grows.

In order to describe the dynamics we require the Rayleigh equation of motion for the radial component. A point on the bubble surface relative to the center can be described by

$$R(\theta,\phi,t) = R_b(t) + \sum_{\ell=1}^{\infty}\sum_{m=-\ell}^{\ell} a_{\ell m} Y_{\ell m}(\theta,\phi). \tag{15}$$

A rather complex set of equations follow from the Lagrangian equations of motion:

$$\begin{aligned}\frac{3}{2}\left(\frac{\dot R_b}{R_b}\right)^2 + \frac{\ddot R_b}{R_b} &= -\frac{1}{\rho R_b^4}\left(2\sigma R_b + pR_b^2 - \frac{(Ne)^2}{8\pi\varepsilon R_b^2}\right)\\ &+ \frac{3}{8\pi R_b}\sum_{\ell,m}\frac{|a_{\ell m}|^2}{\ell+1}\\ &- \frac{1}{4\pi\rho R_b^4}\sum_{\ell,m}\left(p - \frac{3(Ne)^2}{8\pi\varepsilon R_b^4}\ell\right)|a_{\ell m}|^2\end{aligned} \tag{16}$$

and

$$\begin{aligned}&\ddot a_{\ell m} + 3\frac{\dot R_b}{R_b}\dot a_{\ell m}\\ &= -\frac{\ell+1}{\rho R_b^3}\left[\sigma(\ell^2+\ell+1) + 2pR_C - \frac{(Ne)^2}{4\pi\varepsilon R_C}\ell\right]a_{\ell m}.\end{aligned} \tag{17}$$

The first equation is the Rayleigh equation, with an additional electronic term and the second, for the deformation, is similar to the Plesset–Prosperetti equation [40,41] for the deformational amplitudes. For the response of a spherical undeformed bubble ($a_{\ell,m} = 0$) Eq. (16) is solved for pressure steps of 1, 2, and 3 kPa, shown in Fig. 12. Details are given in Ref. [39].

With increasing pressure step, the amplitude of the collapse increases and is cyclic as there is no damping in the equations.

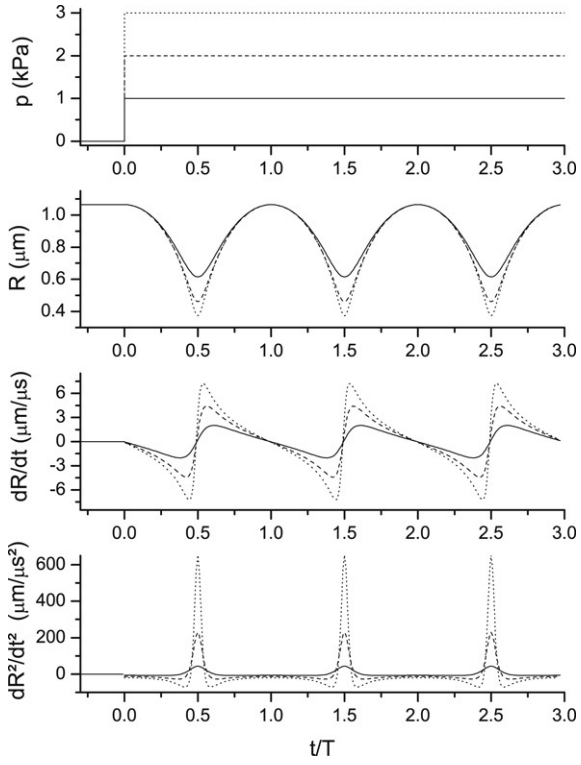

Fig. 12. The response of an MEB in helium with $N = 10^4$ electrons initially at zero pressure to the pressure steps shown in the top panel. The second panel shows the oscillation of the radius. The initial radius is 1.06 microns so the collapse is seen to be substantial. The third panel shows the radial velocity of the surface, and the fourth the radial acceleration. The quantities are cyclic as there is no damping in the equations. The time axis is scaled to the period of the oscillations with $T = 0.795, 0.570$, and 0.462 μs for the 1, 2, and 3 kPa pressure steps, respectively.

The radial acceleration is very sharp and peaked at the time when the bubble radius is at its minimum. The response times are less than a microsecond. The peaked acceleration is quite large, substantially greater than 10^6 m/s^2.

For angularly deformed bubbles (in the initial state) we expect stable or unstable modes, depending on the pressure step and the mode. The behavior is found by solving Eq. (17). To study a stable situation, a higher mode, $\ell = 25$, is chosen so that with the pressure step the ripplon frequency remains non-zero. The calculated behavior is shown in Fig. 13. For a mode with unstable conditions, i.e. the pressure step is sufficient to drive an (ℓ, m) mode to zero frequency, the mode amplitude grows larger than the bubble diameter after collapse and is non-oscillatory.

2.2. Metal nanoshells

2.2.1. Nanoshell fabrication

Metal nanoshells are composite nanoparticles consisting of dielectric (mostly silica glass) core and a thin metal (mostly gold, sometimes silver) shell [42]. The preparation technique is based on the principles of molecular self-assembly and reduction chemistry of metal colloid synthesis. First silica nanoparticles dispersed in solution are grown. Then very small (1–2 nm in diameter) metal colloid particles are attached to the

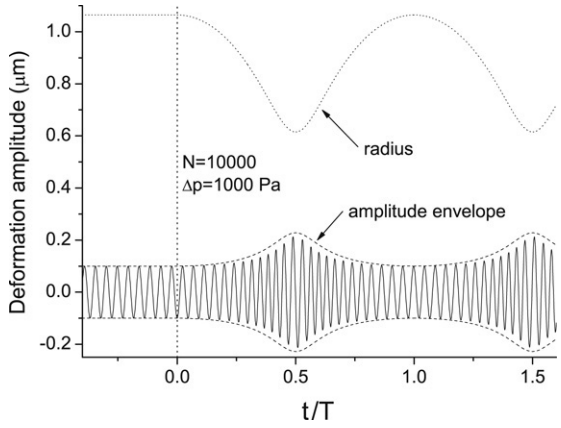

Fig. 13. The response of an MEB which initially has a ripplon mode amplitude. The bubble radius collapses and there is a high frequency oscillation of with an envelope that oscillates with the same period as the radius (dashed curve).

surface of the nanoparticles via molecular linkages, resulting in a discontinuous metal colloid layer. Additional metal is grown onto the metal colloid adsorbates via chemical reduction in solution. The different steps in the growth can be seen in the Fig. 14. Sometimes, mainly for *in vivo* applications, the surface is coated by a poly(ethylene glycol) layer to enhance biocompatibility [43,44]. The thinnest shell that is possible to prepare nowadays with the above mentioned technique is ∼5 nm. The typical shell thickness varies 5–20 nm, whereas the inner radius typically varies between 60–210 nm.

The interest in nanoshells follows in part from their optical properties [45,46] and their biocompatibility. The optical properties are governed by strong surface plasmon resonance. Surface plasmons can be excited on both (inner and outer) surfaces of the metal shell and because of the small distance between them, they couple strongly [47]. The resulting resonance frequency depends strongly on the ratio of the inner and the outer radius of the shell, and can be used for surface enhanced Raman scattering [48]. Thanks to the wide tunability of their absorption and scattering resonance in the infrared and visual spectral region, metal nanoshells are very promising in cancer research and treatment. Human tissue is most transparent in the region 650–900 nm, slightly dependent on the kind of tissue. Metal nanoshells conjugated with antibodies or proteins specifically sensitive to the substances on the surface of cancer cells can by transported by blood circulation to the tumor location, where they bind to the cells. The metal nanoshells can serve both for the imaging and the thermal ablation of the cancer cells [49] as they both scatter and strongly absorb the light.

2.2.2. *Quasi-2D shell as a multilayer system*

With respect to the Wigner–Seitz radius of the multielectron bubbles described earlier, the Wigner–Seitz radius of the nanoshell system is much smaller. Whereas in MEBs a single radial mode is occupied, in nanoshells more than one band can be occupied. If we consider the radial confinement as a square well potential with thickness d, the bottom of the bands are given by

$$E_n = \frac{\hbar^2 \pi^2}{2m_e d^2} n^2.$$

Within one band, we have the usual angular momentum spectrum, so that

$$E_{n,\ell,m} = \frac{\hbar^2 \pi^2}{2m_e d^2} n^2 + \frac{\hbar^2}{2m_e R^2} \ell(\ell+1). \tag{18}$$

How many of the bands with different n will be occupied for total number of electrons N? For every level n we fill the (ℓ, m) levels up to Fermi energy E_F, corresponding to the orbital angular momentum $L_F^{(n)}$. The number of electrons sitting in this nth band is (the approximation might not be valid in some

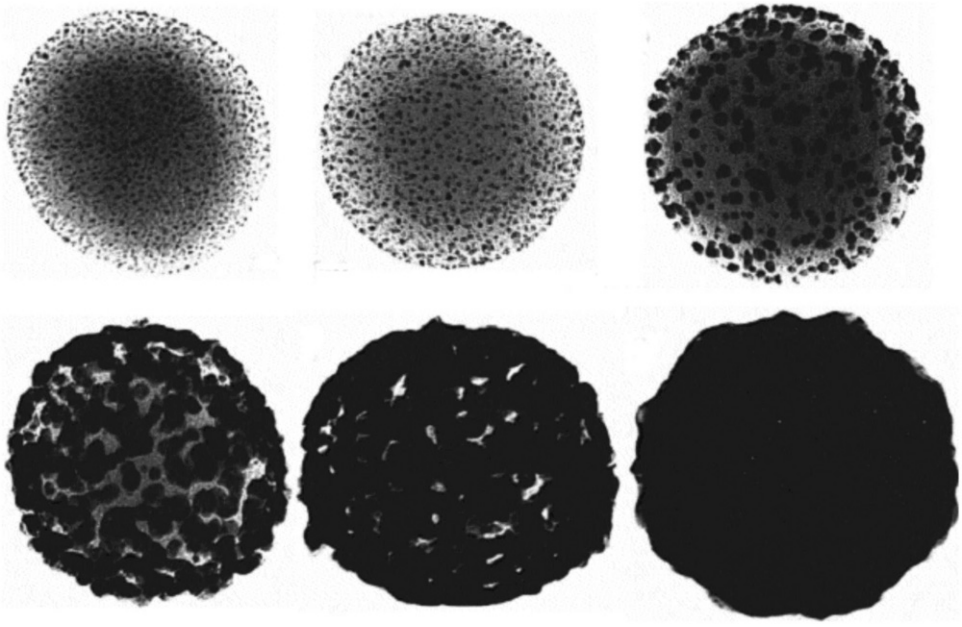

Fig. 14. Transmission electron microscope images of nanoshells in various states of formation, from Ref. [43].

bands, if $L_F^{(n)}$ is not large enough).

$$N^{(n)} = 2(L_F^{(n)} + 1)^2 \approx 2(L_F^{(n)})^2.$$

$L_F^{(n)}$ should be such that E_F is the same over all n bands. Thus:

$$E_F = \frac{\hbar^2\pi^2}{2m_e d^2}n^2 + \frac{\hbar^2 L_F^{(n)}(L_F^{(n)}+1)}{2m_e R^2}$$
$$\Rightarrow L_F^{(n)} \approx \sqrt{\frac{2m_e R^2}{\hbar^2}E_F - \frac{\pi^2 R^2}{d^2}n^2}.$$

The total number of electrons in the nanoshell will be:

$$N = \sum_{n=0}^{n_F} N^{(n)} = 2\sum_{n=0}^{n_F}\left(\frac{2mR^2}{\hbar^2}E_F - \frac{\pi^2R^2}{d^2}n^2\right)$$
$$= n_F\frac{2mR^2}{\hbar^2}E_F - \frac{2\pi^2R^2}{d^2}\frac{1}{6}\left(2n_F^3 + 3n_F^2 + n_F\right)$$

here n_F is the highest occupied band at zero temperature, so it corresponds to the number of occupied bands. The relationship between E_F and n_F is

$$E_F = \frac{\hbar^2\pi^2}{2m}\left(\frac{n_F^2}{d^2} + \frac{L_F^{(n_F)}(L_F^{(n_F)}+1)}{\pi^2R^2}\right) \approx \frac{\hbar^2\pi^2}{2md^2}n_F^2.$$

If we neglect the second term in parentheses, we can make an error in n_F of at most 1. For large n_F we also neglect the quadratic and linear term in expression for N,

$$N \approx n_F\frac{2mR^2}{\hbar^2}\frac{\hbar^2\pi^2}{2md^2}n_F^2 - \frac{2\pi^2R^2}{d^2}\frac{1}{6}2n_F^3$$
$$\Rightarrow n_F \approx \sqrt[3]{\frac{3d^2N}{\pi^2R^2}}. \tag{19}$$

The amount of free electrons in a shell of thickness d and radius R is

$$N = n_u 4\pi^2\frac{R^2 d}{a^3}$$

where n_u is the number of atoms per unit cell and a is the size of the unit cell. Then we simplify the expression:

$$n_F \approx \sqrt[3]{\frac{3d^2 n_u\cdot 4d}{a^3}} = \sqrt[3]{12n_u}\frac{d}{a}.$$

Both gold and silver have 1s electron in the valence band and crystallize in the fcc crystal structure, with $n_u = 2$ atoms per unit cell. The values of unit cell vectors are $a_{Au} = 0.40782$ nm and $a_{Ag} = 0.40853$ nm. In a gold shell with $R = 60$ nm and $d = 5$ nm there are 2.2 10^7 electrons. In this case $n_F = 36$ different radial states will be occupied. For $d = 0.5$ nm $n_F = 4$ radial states are occupied and for $d = 20$ nm 145 states with different n will be used.

A first approximation to metal nanoshells, by Prodan and Nordlander [50], takes into account only the (coupled) surface plasmon branches of the inner and outer surface of the nanoshell. The optical response of the nanoshell is shown by Prodan et al. [47] to be determined by the interaction of the plasmons on these surfaces, leading to mixing, splitting and shifts of the plasmon energies for single spherical surfaces.

In the next section we review the dielectric response (including plasmons) for a single spherical, two-dimensional electron gas and the magnetic field effects on these. Multilayer surfaces, such as a four-layer concentric nanoshell can be described by the interaction of independent layers.

3. Electric properties of the spherical two-dimensional electron system

3.1. Basic properties and phases

Nano-objects of a spherical shape are the subject of intense experimental and theoretical work. In particular, metallic shell structures and multielectron bubbles are of considerable theoretical and experimental interest because of their interesting electronic and optical properties. In recent years, it has been possible to manufacture spherical shaped nanostructures ranging from fullerene size to nanosized objects such as SiO_2 balls in opals [51], nanoshells [42] and multielectron bubbles [5,12]. For multielectron bubbles, the electrons move freely in the direction tangential to the spherical helium surface. The electrons therefore effectively form a spherical two-dimensional electron gas (S2DEG). Also, a S2DEG can be realized in charged droplets [52] and in doped semiconductor particles if carriers accumulate in a surface layer [53].

Density functional calculations for the multielectron bubbles [14,15] indicate that the electrons inside the bubble are not spread out homogeneously, but instead form a thin spherical layer with thickness $\delta \ll R$ and radius about $R - \delta$, anchored to the surface of the helium, with a binding energy of the order of several kelvins [14,54]. The electrons are free to move in the directions tangential to the spherical helium surface, so that in effect they form a spherical two-dimensional electron gas (S2DEG).

Our present analysis of the spherical two-dimensional electron gas, albeit motivated by the study of multielectron bubbles, is equally relevant from a fundamental point of view: it is the logical next step to take after analysis of the flat two-dimensional electron gas, a topic that keeps drawing renewed attention.

To describe the electrons on a sphere, it is natural to use spherical coordinates $\mathbf{r} = \{r, \theta, \phi\}$. We will assume that the electrons are strongly confined along the radial direction, but free to move along the directions tangential to the surface. This corresponds to the assumption that the single-particle wave function describing a free electron can be factorized in a radial wave function and an angular part. The radial wave function is strongly localized in a shell of thickness d around $r = R$ where R is the radius of the two-dimensional shell. As long as $d \ll R$, the assumption that the radial part of the wave function can be factored out of the total wave function is good. For multielectron bubbles, typically $R \sim 1$ μm while $d \sim 1$ nm.

All the electrons on the shell have the same radial wave function, and will differ only in the angular part. If we neglect

interaction (to be included in the next section), the angular wave functions have to be eigenfunctions of

$$\Delta_\Omega = \frac{1}{\sin\theta}\frac{\partial}{\partial\theta}\left(\sin\theta\frac{\partial}{\partial\theta}\right) + \frac{1}{\sin^2\theta}\frac{\partial^2}{\partial\phi^2} \tag{20}$$

the angular part of the Laplacian in spherical coordinates. These eigenfunctions are the spherical harmonics, and we get for the single-particle wave functions

$$-\frac{\hbar^2}{2m_e R^2}\Delta_\Omega Y_{\ell m}(\Omega) = E_{\ell m} Y_{\ell m}(\Omega) \tag{21}$$

with

$$E_{\ell m} = \frac{\hbar^2\,\ell(\ell+1)}{2m_e R^2}. \tag{22}$$

The single-particle basis is characterized by the angular momentum quantum numbers $\{\ell, m\}$. Note that for a flat two-dimensional electron gas, the single-particle electron wave functions would be plane waves $\varphi_{\mathbf{k}}(\Omega) = e^{i\mathbf{k}\cdot\mathbf{r}}/\sqrt{L}$ characterized by the quantum numbers $\mathbf{k} = \{k_x, k_y\}$ with $k_x, k_y = n\pi/L$ where L is the length of the system and n is an integer. For the sphere, the (non-interacting) single-particle wave functions $\varphi_{\ell,m}(\Omega) = Y_{\ell,m}(\Omega)$ are labeled by the quantum numbers $\{\ell, m\}$ where ℓ is a non-negative integer and m is an integer in the range $\{-\ell, \ldots, \ell\}$. These single-particle energy levels are degenerate for $\ell > 0$, and have a degeneracy of $2\ell+1$. For a very large bubble, large ℓ modes can be easily populated. Spherical harmonics with large ℓ are locally isomorphic with plane waves with $k = \ell/R$, so that in the limit $R \to \infty$ we retrieve the flat 2DEG result for the energy of the single-particle levels, $(\hbar k)^2/(2m_e)$.

An ideal (non-interacting) electron gas on a sphere can be described by a Fermi sea where the eigenfunctions are spherical harmonics $Y_{\ell m}$. The N electrons fill up the single-particle levels up to a Fermi level L_F that satisfies

$$N = 2\sum_{\ell=1}^{L_F}(2\ell+1) = 2(L_F+1)^2 \tag{23}$$

$$\to L_F = \left\lceil \sqrt{N/2} - 1 \right\rceil. \tag{24}$$

where $\lceil x \rceil$ means the smallest integer larger than or equal to x. The factor 2 comes from the spin up/spin down degeneracy for the electrons. For electron bubbles with 10^6–10^8 electrons, this means $L_F \approx 10^3$–10^4. An interesting property of the S2DEG is its Fermi energy E_F as a function of the number of particles. As the number of particles increases, more single-particle energy levels have to be filled up (increasing E_F), but at the same time the bubble radius will also increase (decreasing E_F). The Fermi energy is (for $\sqrt{N/2} \gg 1$),

$$E_F = \frac{\hbar^2\,L_F(L_F+1)}{2m_e R^2} \tag{25}$$

$$= \frac{\hbar^2 N}{4m_e}\left(\frac{1}{4}\sqrt[3]{\frac{N^2e^2}{\pi^2\varepsilon_v\varepsilon\sigma}}\right)^{-2}$$

$$= N^{-1/3}\frac{4\hbar^2}{m_e}\left(\frac{\pi^2\varepsilon_v\varepsilon\sigma}{e^2}\right)^{2/3}. \tag{26}$$

This rather surprising result shows that the increase of bubble radius with increasing N wins over the level filling, so that the Fermi energy in this system actually decreases with increasing N. Putting in the parameters, we arrive at

$$E_F = N^{-1/3} \times 2.29 \times 10^{-20}\text{J} = N^{-1/3} \times 143\ \text{meV}. \tag{27}$$

For $N = 10^6$ the Fermi energy is 16 K, for $N = 10^8$ we find $E_F = 3.57$ K. This means that smaller bubbles (10^6–10^7 electrons) will be in the degenerate Fermi gas regime. Intermediate bubbles (10^8 electrons) will be around the quantum degeneracy point, and for large bubbles (10^9 electrons) the quantum degeneracy will have been partially lifted. This is in contrast with metals at room temperature, which are deep in the quantum degenerate regime.

Different phases of the electronic system are possible due to

- the Coulomb interaction and to
- the interaction of the electrons with modes of oscillation such as ripplons in multielectron bubbles or (interface) phonons in nanoshells.

On a flat helium surface, the Coulomb interaction can lead to the formation of a Wigner lattice of electrons rather than a 2D electron gas [8]. This phase can also appear for a spherical system, but the topology introduces defects in the lattice. Whereas on a flat surface, a defect free triangular lattice can be formed where every electron has six neighbors, on a spherical surface there need to be exactly twelve sites where electrons have only five neighbors. More defects can be formed, but for every additional electron with only five neighbors, another electron will have seven neighbors. The fivefold and sevenfold site defects can either be bound together, or hop around freely — this additional order parameter introduces nematic phases that can be distinguished in the Wigner lattice on a spherical surface [25,55].

The electron–ripplon interaction (or electron phonon interaction) leads to polaron formation when the electron and the local deformation of the helium surface (or the crystal lattice) together form a quasiparticle [56,57]. The electron–ripplon coupling on a curved surface can be much stronger than on a flat helium surface, and this can strongly localize the electron wave function in a self-induced trapping potential, leading to the formation of a Wigner lattice of ripplonic polarons [58]. Finally, the exchange of ripplons (similar to the exchange of phonons) between electrons leads to an attractive effective interaction that may result in strong pairing correlations and superconductivity [59].

In the remainder of this review, we will investigate these different phases and how they differ from the analogous phases on the flat surface. Of course, the electron liquid is still a possible phase, too. It competes with the Wigner crystallized phase, and can be described in second quantization based on the spherical harmonics, which are introduced in the next subsection (cf. Ref. [60]).

3.2. Green's function formalism for a sphere

The many-body theory, and especially the second quantization formalism, commonly treats flat spaces of one, two or three dimensions, using decompositions in plane waves. For a spherical surface the spherical harmonics are better suited. First, some notation conventions are listed. Each time, also the familiar plane wave counterpart is listed.

- The position operators $\mathbf{r}_j = \{x_j, y_j\}$ $(j = 1, \ldots, N)$ are replaced by the spherical angle operator $\Omega_j = \{\theta_j, \phi_j\}$ giving the position on the spherical surface.
- The unitary operator in flat space can be decomposed as $\mathbf{1} = \int \mathrm{d}\mathbf{r}\, |\mathbf{r}\rangle \langle \mathbf{r}|$ where $\langle \mathbf{r}|\varphi\rangle = \varphi(\mathbf{r})$; whereas on the spherical surface the unitary operator can be decomposed as

$$\mathbf{1} = \int \mathrm{d}\Omega\, |\Omega\rangle \langle \Omega| = \int_0^{\pi} \mathrm{d}\theta \int_0^{2\pi} \mathrm{d}\phi \sin\theta\, |\Omega\rangle \langle \Omega|\,, \quad (28)$$

  where $\langle \Omega|\varphi\rangle = Y_{\ell m}(\Omega)$.
- The second-quantized operators $\widehat{c}^{+}_{\ell,m}$ and $\widehat{c}_{\ell,m}$ are introduced; they respectively create and annihilate an electron in the single-particle state with wave function $Y_{\ell m}$. These operators satisfy Fermionic anticommutation relations $\left[\widehat{c}_{\ell,m}, \widehat{c}^{+}_{\ell',m'}\right]_+ = \delta_{\ell,\ell'}\delta_{m,m'}$ and are the spherical counterparts of the plane wave operators $\widehat{c}^{+}_{\mathbf{k}}$ and $\widehat{c}_{\mathbf{k}}$ which respectively create and annihilate an electron in the single-particle state $\varphi_{\mathbf{k}}$.

3.2.1. Kinetic energy

A one-particle operator on the many-body system is an operator can be written as:

$$\widehat{A} = \sum_{j=1}^{N} \widehat{A}(\Omega_j). \quad (29)$$

In second quantization based on a set of single-particle wave functions $\varphi_{\ell m}(\Omega)$, this operator can be written as

$$\widehat{A} = \sum_{\ell=0}^{\infty} \sum_{m=-\ell}^{\ell} \sum_{\ell'=0}^{\infty} \sum_{m'=-\ell}^{\ell} \left\langle \ell m \left| \widehat{A} \right| \ell' m' \right\rangle \widehat{c}^{+}_{\ell m} \widehat{c}_{\ell' m'}. \quad (30)$$

This can be applied to the kinetic energy operator $\widehat{T}$

$$\widehat{T} = \sum_{j=1}^{N} \frac{-\hbar^2}{2m_{\mathrm{e}}R^2} \Delta_{\Omega_j}. \quad (31)$$

Its expectation value with respect to spherical harmonics is

$$\left\langle \ell m \left| \widehat{T} \right| \ell' m' \right\rangle = \int \mathrm{d}\Omega Y^*_{\ell m}(\Omega) \frac{-\hbar^2}{2m_{\mathrm{e}}R^2} \Delta_{\Omega} Y_{\ell' m'}(\Omega) \quad (32)$$

$$= \frac{\hbar^2\, \ell(\ell+1)}{2m_{\mathrm{e}}R^2} \int \mathrm{d}\Omega Y_{\ell m}(\Omega) Y_{\ell' m'}(\Omega) \quad (33)$$

$$= \frac{\hbar^2\, \ell(\ell+1)}{2m_{\mathrm{e}}R^2} \delta_{\ell,\ell'}\delta_{m,m'}. \quad (34)$$

So that its second-quantized form is

$$\widehat{T} = \sum_{\ell=0}^{\infty} \sum_{m=-\ell}^{\ell} \frac{\hbar^2\, \ell(\ell+1)}{2m_{\mathrm{e}}R^2} \widehat{c}^{+}_{\ell m} \widehat{c}_{\ell m}. \quad (35)$$

3.2.2. Coulomb interaction

In first quantization, the Coulomb interaction can be written as

$$\widehat{\mathcal{H}}_{\mathrm{coul}} = \frac{1}{2} \sum_{j=1}^{N} \sum_{j' \neq j=1}^{N} \frac{\mathrm{e}^2}{4\pi\varepsilon} \frac{1}{|\widehat{\mathbf{r}}_j - \widehat{\mathbf{r}}_{j'}|}, \quad (36)$$

where $\mathbf{r}_j$ and $\mathbf{r}_{j'}$ are the position operators of electrons j and j' — the electrons are restricted to a spherical shell of radius R and negligible width. The Coulomb interaction is ideally suited to rewrite in spherical harmonics:

$$\widehat{\mathcal{H}}_{\mathrm{coul}} = \frac{1}{2} \sum_{j=1}^{N} \sum_{j' \neq j=1}^{N} \frac{\mathrm{e}^2}{4\pi\varepsilon} \frac{1}{R} \sum_{\ell=0}^{\infty} \sum_{m=-\ell}^{\ell} \frac{4\pi}{2\ell+1} \times Y_{\ell,m}(\widehat{\Omega}_j) Y^*_{\ell,m}(\widehat{\Omega}_{j'}). \quad (37)$$

The advantage of the Coulomb interaction in the spherical representation is that the $\widehat{\Omega}_j$ and $\widehat{\Omega}_{j'}$ are factorized. The standard second-quantized form of this operator is

$$\widehat{\mathcal{H}}_{\mathrm{coul}} = \sum_{\ell_1,m_1} \sum_{\ell_2,m_2} \sum_{\ell_3,m_3} \sum_{\ell_4,m_4} \langle V_2 \rangle\, \widehat{c}^{+}_{\ell_4,m_4} \widehat{c}^{+}_{\ell_3,m_3} \widehat{c}_{\ell_2,m_2} \widehat{c}_{\ell_1,m_1} \quad (38)$$

with $\langle V_2 \rangle$

$$= \frac{\mathrm{e}^2}{2\varepsilon} \frac{1}{R} \sum_{\ell=0}^{\infty} \sum_{m=-\ell}^{\ell} \int \mathrm{d}\Omega \int \mathrm{d}\Omega' Y^*_{\ell_4,m_4}(\Omega) Y^*_{\ell_3,m_3}(\Omega') \times \frac{Y_{\ell,m}(\Omega) Y^*_{\ell,m}(\Omega')}{2\ell+1} Y_{\ell_2,m_2}(\Omega') Y_{\ell_1,m_1}(\Omega). \quad (39)$$

The double integration can be factorized:

$$\langle V_2 \rangle = \frac{\mathrm{e}^2}{2\varepsilon} \frac{1}{R} \sum_{\ell=0}^{\infty} \sum_{m=-\ell}^{\ell} \frac{1}{2\ell+1} \times \left[\int \mathrm{d}\Omega Y^*_{\ell_4,m_4}(\Omega) Y_{\ell,m}(\Omega) Y_{\ell_1,m_1}(\Omega) \right] \times \left[\int \mathrm{d}\Omega' Y^*_{\ell_3,m_3}(\Omega') Y^*_{\ell,m}(\Omega') Y_{\ell_2,m_2}(\Omega') \right], \quad (40)$$

so that the Coulomb part of the Hamiltonian can be written as

$$\widehat{\mathcal{H}}_{\mathrm{coul}} = \frac{\mathrm{e}^2}{2\varepsilon R} \sum_{\ell_1,m_1} \sum_{\ell_2,m_2} \sum_{\ell=0}^{\infty} \sum_{m=-\ell}^{\ell} \frac{1}{2\ell+1} \times \sum_{\ell_4,m_4} \int \mathrm{d}\Omega Y^*_{\ell_4,m_4}(\Omega) Y_{\ell,m}(\Omega) Y_{\ell_1,m_1}(\Omega) \widehat{c}^{+}_{\ell_4,m_4} \times \sum_{\ell_3,m_3} \int \mathrm{d}\Omega' Y^*_{\ell_3,m_3}(\Omega') Y^*_{\ell,m}(\Omega') Y_{\ell_2,m_2}(\Omega') \widehat{c}^{+}_{\ell_3,m_3} \times \widehat{c}_{\ell_2,m_2} \widehat{c}_{\ell_1,m_1}. \quad (41)$$

Integrals over triple products of spherical harmonics appear in this expression. A double product would be easy to integrate with the orthonormality relation

$$\int \mathrm{d}\Omega Y_{j,m}(\Omega) Y^*_{j',m'}(\Omega) = \delta_{j,j'}\delta_{m,m'}. \tag{42}$$

Reducing the triple product to a double product relies on the addition of angular momenta. Two spherical harmonics can be combined into a sum of spherical harmonics through:

$$\begin{aligned} &Y_{j_1,m_1}(\Omega) Y_{j_2,m_2}(\Omega) \\ &= \sum_{j=|j_1-j_2|}^{j_1+j_2} \sum_{m=-j}^{j} \sqrt{\frac{(2j_1+1)(2j_2+1)}{4\pi(2j+1)}} \langle j_1, 0; j_2, 0 | j, 0\rangle \\ &\quad \times \langle j_1, m_1; j_2, m_2 | j, m\rangle Y_{j,m}(\Omega). \end{aligned} \tag{43}$$

From this, it also follows that $Y^*_{j_1,m_1}(\Omega) Y_{j_2,m_2}(\Omega) = (-1)^{m_1} Y_{j_1,-m_1}(\Omega) Y_{j_2,m_2}(\Omega)$. In expression (43), $\langle j_1, m_1; j_2, m_2 | j, m\rangle$ is the Clebsch–Gordan coefficient for combining the angular momentum states $|j_1, m_1\rangle$ and $|j_2, m_2\rangle$ into the angular momentum state $|j, m\rangle$, sometimes denoted as $C(j_1, m_1; j_2, m_2 | j, m)$. The complex conjugate expression can be found by replacing all Y's by Y^* since the Clebsch–Gordan coefficients are real. The addition rule of spherical harmonics is more restrictive than the addition rule of angular momenta: it contains the extra coefficient $\langle j_1, 0; j_2, 0 | j, 0\rangle$ which is different from zero only if $j_1 + j_2 - j$ is even. The combination of angular momenta of magnitude j_1 and j_2 can lead to all values of angular momentum between $|j_1 - j_2|$ and $j_1 + j_2$, but the product of spherical harmonics of order j_1 and j_2 lead to spherical harmonics of order $j_1 + j_2$, $j_1 + j_2 - 2$, $j_1 + j_2 - 4$, …, $|j_1 - j_2|$. This insures that the parity of all terms on the right hand side $(-1)^j$ equals the parity of all terms on the left hand side $(-1)^{j_1+j_2}$. The addition rule (43) allows to perform the integral of the triple product of Y's, combining the ℓ and ℓ_1 spherical harmonics.

$$\begin{aligned} &\int \mathrm{d}\Omega Y_{\ell,m}(\Omega) Y^*_{\ell_2,m_2}(\Omega) Y_{\ell_1,m_1}(\Omega) \\ &= \sum_{\ell'=|\ell-\ell_1|}^{\ell+\ell_1} \sum_{m'=-\ell'}^{\ell'} \sqrt{\frac{(2\ell+1)(2\ell_1+1)}{4\pi(2\ell'+1)}} \\ &\quad \times \left\langle \ell, 0; \ell_1, 0 | \ell', 0\right\rangle \left\langle \ell, m; \ell_1, m_1 | \ell', m'\right\rangle \\ &\quad \times \int \mathrm{d}\Omega Y_{\ell',m'}(\Omega) Y^*_{\ell_2,m_2}(\Omega). \end{aligned} \tag{44}$$

The remaining integral over the spherical angle Ω gives $\delta_{\ell',\ell_2}\delta_{m',m_2}$.

To draw the analogy with the plane wave density operator, we introduce the following notation:

$$\begin{aligned} \widehat{c}^+_{(\ell_1,m_1)\otimes(\ell,m)} = &\sum_{\ell'=|\ell-\ell_1|}^{\ell+\ell_1} \sum_{m'=-\ell'}^{\ell'} \sqrt{\frac{(2\ell+1)(2\ell_1+1)}{4\pi(2\ell'+1)}} \\ &\times \left\langle \ell, 0; \ell_1, 0 | \ell', 0\right\rangle \\ &\times \left\langle \ell, m; \ell_1, m_1 | \ell', m'\right\rangle \widehat{c}^+_{\ell' m'}. \end{aligned} \tag{45}$$

The operator $\widehat{c}^+_{(\ell_1,m_1)\otimes(\ell,m)}$ creates an electron in a state which results from the combination of a spherical (ℓ_1, m_1) state and a spherical (ℓ, m) state, as governed by the spherical harmonics addition formula (43).

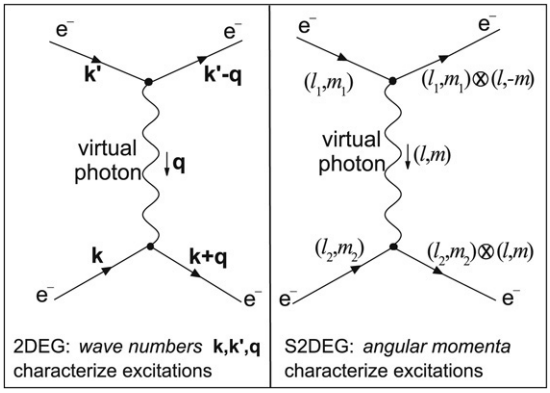

Fig. 15. The physical process described by $\widehat{\mathcal{H}}_{\mathrm{coul}}$ (from Ref. [60]).

Now we return to (41). We combine (44) and (45) to find

$$\begin{aligned} &\sum_{\ell_4,m_4} \int \mathrm{d}\Omega Y^*_{\ell_4,m_4}(\Omega) Y_{\ell,m}(\Omega) Y_{\ell_1,m_1}(\Omega) \widehat{c}^+_{\ell_4,m_4} \\ &\quad = \widehat{c}^+_{(\ell,m)\otimes(\ell_1,m_1)}. \end{aligned} \tag{46}$$

and

$$\begin{aligned} &\sum_{\ell_3,m_3} \int \mathrm{d}\Omega' Y^*_{\ell_3,m_3}(\Omega') Y^*_{\ell,m}(\Omega') Y_{\ell_2,m_2}(\Omega') \widehat{c}^+_{\ell_3,m_3} \\ &\quad = (-1)^m \widehat{c}^+_{(\ell,-m)\otimes(\ell_2,m_2)}. \end{aligned} \tag{47}$$

The notation for the creation operator of a combination of spherical states is simplifying the expression. We find for the Coulomb part of the Hamiltonian

$$\begin{aligned} \widehat{\mathcal{H}}_{\mathrm{coul}} = &\frac{\mathrm{e}^2}{2\varepsilon R} \sum_{\ell_1,m_1} \sum_{\ell_2,m_2} \sum_{\ell,m} \frac{(-1)^m}{2\ell+1} \\ &\times \widehat{c}^+_{(\ell_1,m_1)\otimes(\ell,m)} \widehat{c}^+_{(\ell_2,m_2)\otimes(\ell,-m)} \widehat{c}_{\ell_2,m_2} \widehat{c}_{\ell_1,m_1}. \end{aligned} \tag{48}$$

There is a nice analogy with the plane wave expansion

$$\widehat{\mathcal{H}}^{\text{plane wave}}_{\mathrm{coul}} = \sum_{\mathbf{k}_1} \sum_{\mathbf{k}_2} \sum_{\mathbf{q}} v(\mathbf{q}) \widehat{c}^+_{\mathbf{k}_1+\mathbf{q}} \widehat{c}^+_{\mathbf{k}_2-\mathbf{q}} \widehat{c}_{\mathbf{k}_2} \widehat{c}_{\mathbf{k}_1}, \tag{49}$$

where $v(\mathbf{q})$ is the (ill-behaved) Fourier transform of the Coulomb interaction. The analogy is illustrated in Fig. 15. The electrons interact through the exchange of a virtual photon, which for a flat surface transfers momentum $\mathbf{q}$ and on a sphere transfers angular momentum j.

3.2.3. Electron Green's function

The one-fermion propagator; or Green's function is defined at $T = 0$ through

$$G\left(\ell', m'; t | \ell, m, 0\right) = -\mathrm{i}\left\langle \Psi_0 \left| \mathcal{T}\left[\left\{c_{\ell' m'}(t) c^+_{\ell m}(0)\right\}\right] \right| \Psi_0\right\rangle. \tag{50}$$

For $t > 0$ this is the amplitude (with respect to the ground state) to create a single-particle excitation in state ℓm at time 0, and detect it in state $\ell' m'$ at time t. In this expression $\mathcal{T}$ is the time ordering operator which puts the operator acting at the later times to the left. The ground state of the system is represented by the many-body wave function $|\Psi_0\rangle$.

The calculation is straightforward and gives

$$\mathrm{i}G_0\left(\ell',m';t|\ell,m,0\right)=\delta_{\ell,\ell'}\delta_{m,m'}\exp(-\mathrm{i}E_{\ell m}t/\hbar)\times\begin{bmatrix}\theta(\ell>L_F)\theta(t>0)\\-\theta(\ell\leqslant L_F)\theta(t<0)\end{bmatrix}. \quad (51)$$

The frequency dependent Green's function is found after Fourier transformation:

$$G_0\left(\ell',m';\ell,m|\omega\right)=\int_{-\infty}^{\infty}\mathrm{e}^{\mathrm{i}\omega t}G\left(\ell',m';t|\ell,m,0\right)\mathrm{d}t \quad (52)$$

$$=\delta_{\ell,\ell'}\delta_{m,m'}\left\{\frac{1-n(\ell m)}{\omega-E_{\ell m}+\mathrm{i}\eta}+\frac{n(\ell m)}{\omega-E_{\ell m}-\mathrm{i}\eta}\right\}. \quad (53)$$

Here η is an infinitesimal positive quantity and

$$n(\ell,m)=\frac{1}{1+\exp[(E_{\ell m}-\mu)/(k_{\mathrm{B}}T)]}, \quad (54)$$

is the Fermi–Dirac distribution where μ is the chemical potential, fixed by the condition $\sum_{\ell,m}n(\ell,m)=N$ where N is the number of electrons in the bubble. As discussed earlier, it might be necessary to consider temperatures comparable or larger than the Fermi temperature, a regime that is usually not accessible in bulk metals.

3.3. Hartree–Fock treatment

We described the spherical 2D electron gas (S2DEG) using a second quantization operator formalism where the operators $\hat{c}^{+}_{\ell m}$ and $\hat{c}_{\ell m}$ create and annihilate an electron in the single-particle state given by the spherical harmonic $Y_{\ell m}(\Omega)$.

For the spin mixture, we use operators $\hat{c}^{+}_{\ell m,\sigma}$ and $\hat{c}_{\ell m,\sigma}$ that create and annihilate an electron in the single-particle state given by $Y_{\ell m}(\Omega)\eta(\sigma)$ where η is the spinor for spin up $\sigma=\uparrow$ or spin down $\sigma=\downarrow$. The Hamiltonian of the electron gas is in that case given by

$$\hat{H}=\sum_{\ell=0}^{\infty}\sum_{m=-\ell}^{\ell}\sum_{\sigma}\frac{\hbar^2\,\ell(\ell+1)}{2m_{\mathrm{e}}R^2}\hat{c}^{+}_{\ell m,\sigma}\hat{c}_{\ell m,\sigma}+\frac{\mathrm{e}^2}{2\varepsilon_v R}\sum_{\ell,m}\frac{(-1)^m}{2\ell+1}\times\sum_{\ell_1,m_1,\sigma}\sum_{\ell_2,m_2,\sigma}\hat{c}^{+}_{(\ell_1,m_1)\otimes(\ell,m),\sigma}\hat{c}^{+}_{(\ell_2,m_2)\otimes(\ell,-m),\sigma'}\times\hat{c}_{(\ell_2,m_2),\sigma'}\hat{c}_{(\ell_1,m_1),\sigma}, \quad (55)$$

where

$$\widehat{c}^{+}_{(\ell_1,m_1)\otimes(\ell,m),\sigma}=\sum_{\ell'=0}^{\infty}\sum_{m'=-\ell'}^{\ell'}\left[\int\mathrm{d}\Omega Y_{\ell,m}(\Omega)Y^{*}_{\ell',m'}(\Omega)Y_{\ell_1,m_1}(\Omega)\right]\widehat{c}^{+}_{(\ell'm'),\sigma} \quad (56)$$

$$=\sum_{\ell'=|\ell-\ell_1|}^{\ell+\ell_1}\sum_{m'=-\ell'}^{\ell'}\sqrt{\frac{(2\ell+1)(2\ell_1+1)}{4\pi(2\ell'+1)}}\left\langle\ell,0;\ell_1,0|\ell',0\right\rangle\times\left\langle\ell,m;\ell_1,m_1|\ell',m'\right\rangle\widehat{c}^{+}_{(\ell',m'),\sigma} \quad (57)$$

creates an electron in the single-particle state resulting from the multiplication of the angular momentum states (ℓ_1,m_1) and (ℓ,m).

3.3.1. Kinetic energy

We now assume that the ground state $\left|N_\uparrow N_\downarrow\right\rangle$ consists of a Fermi triangle filled up to the Fermi levels $L_\uparrow$ for the spin ups and $L_\downarrow$ for the spin downs. The number of spin up and spin down electrons fix these levels: $N_{\uparrow,\downarrow}=\left(L_{\uparrow,\downarrow}+1\right)^2$. Then we evaluate the energy of this system by treating the Coulomb interaction as a perturbation. The zeroth-order contribution is

$$E_0=E_{\mathrm{kin}}=\frac{\hbar^2}{2m_{\mathrm{e}}R^2}\left\{\sum_{\ell=0}^{L_{F,\uparrow}}\sum_{m=-\ell}^{\ell}\ell(\ell+1)+\sum_{\ell=0}^{L_{F,\downarrow}}\sum_{m=-\ell}^{\ell}\ell(\ell+1)\right\}=\frac{\hbar}{2m_{\mathrm{e}}R^2}\times\left\{\frac{L_\uparrow\left(L_\uparrow+2\right)\left(L_\uparrow+1\right)^2}{2}+\frac{L_\downarrow\left(L_\downarrow+2\right)\left(L_\downarrow+1\right)^2}{2}\right\}. \quad (58)$$

For $N\gg1$ we have

$$E_0\approx\frac{\hbar^2}{4m_{\mathrm{e}}R^2}(N_\uparrow^2+N_\downarrow^2). \quad (59)$$

When the kinetic energy dominates, it is energetically advantageous to have an equal number of spin up and spin down electrons

3.3.2. Direct Coulomb energy

The first-order correction due to the Coulomb interaction is

$$E_1=\frac{\mathrm{e}^2}{2\varepsilon_v R}\sum_{\ell,m}\frac{(-1)^m}{2\ell+1}\sum_{\ell_1,m_1,\sigma}\sum_{\ell_2,m_2,\sigma'}\times\left\langle N_\uparrow N_\downarrow\right|\hat{c}^{+}_{(\ell_1,m_1)\otimes(\ell,m),\sigma}\hat{c}^{+}_{(\ell_2,m_2)\otimes(\ell,-m),\sigma'}\times\hat{c}_{(\ell_2,m_2),\sigma'}\hat{c}_{(\ell_1,m_1),\sigma}\left|N_\uparrow N_\downarrow\right\rangle. \quad (60)$$

The expectation value will differ from zero only when the creation/annihilation operators are paired up. There are two ways of pairing up the operators, giving two terms, $E_1=E_D+E_X$. We obtain the direct Coulomb contribution (the Hartree term) by pairing up as follows:

$$E_D=\frac{\mathrm{e}^2}{2\varepsilon_v R}\sum_{\ell,m}\frac{1}{2\ell+1}\sum_{\ell_1,m_1,\sigma}\sum_{\ell_2,m_2,\sigma'}\times\left\langle N_\uparrow N_\downarrow\left|\hat{c}^{+}_{(\ell_1,m_1)\otimes(\ell,m),\sigma}\hat{c}_{(\ell_1,m_1),\sigma}\right|N_\uparrow N_\downarrow\right\rangle \quad (61)$$

$$\times\left\langle N_\uparrow N_\downarrow\left|(-1)^m\hat{c}^{+}_{(\ell_2,m_2)\otimes(\ell,-m),\sigma'}\hat{c}_{(\ell_2,m_2),\sigma'}\right|N_\uparrow N_\downarrow\right\rangle. \quad (62)$$

Filling in expression for the creation operator, we find for the first factor

$$\left\langle N_\uparrow N_\downarrow \left| \hat{c}^+_{(\ell_1,m_1)\otimes(\ell,m),\sigma} \hat{c}_{(\ell_1,m_1),\sigma} \right| N_\uparrow N_\downarrow \right\rangle$$
$$= \sum_{\ell'=0}^{\infty} \sum_{m'=-\ell'}^{\ell'} \left[\int \mathrm{d}\Omega Y_{\ell,m}(\Omega) Y^*_{\ell',m'}(\Omega) Y_{\ell_1,m_1}(\Omega) \right]$$
$$\times \left\langle N_\uparrow N_\downarrow \left| \widehat{c}^+_{(\ell'm'),\sigma} \hat{c}_{(\ell_1,m_1),\sigma} \right| N_\uparrow N_\downarrow \right\rangle, \quad (63)$$

which will differ from zero only if $(\ell', m') = (\ell_1, m_1)$ and $\ell_1 \leqslant L_\sigma$. Hence we have

$$\left\langle N_\uparrow N_\downarrow \left| \hat{c}^+_{(\ell_1,m_1)\otimes(\ell,m),\sigma} \hat{c}_{(\ell_1,m_1),\sigma} \right| N_\uparrow N_\downarrow \right\rangle$$
$$= \Theta(\ell_1 \leqslant L_\sigma) \times \int \mathrm{d}\Omega Y_{\ell,m}(\Omega) Y^*_{\ell_1,m_1}(\Omega) Y_{\ell_1,m_1}(\Omega),$$

and analogously for the second factor

$$\left\langle N_\uparrow N_\downarrow \left| (-1)^m \hat{c}^+_{(\ell_2,m_2)\otimes(\ell,-m),\sigma'} \hat{c}_{(\ell_2,m_2),\sigma'} \right| N_\uparrow N_\downarrow \right\rangle$$
$$= \Theta(\ell_2 \leqslant L_{\sigma'}) \times \int \mathrm{d}\Omega\, Y^*_{\ell,m}(\Omega) Y^*_{\ell_2,m_2}(\Omega) Y_{\ell_2,m_2}(\Omega). \quad (64)$$

so that

$$E_D = \frac{\mathrm{e}^2}{2\varepsilon_v R} \sum_{\ell,m} \frac{1}{2\ell+1} \sum_{\sigma,\sigma'} \sum_{\ell_1 \leqslant L_\sigma, m_1} \sum_{\ell_2 \leqslant L_{\sigma'}, m_2}$$
$$\times \int \mathrm{d}\Omega Y_{\ell,m}(\Omega) Y^*_{\ell_1,m_1}(\Omega) Y_{\ell_1,m_1}(\Omega)$$
$$\times \int \mathrm{d}\Omega' Y^*_{\ell,m}(\Omega') Y^*_{\ell_2,m_2}(\Omega') Y_{\ell_2,m_2}(\Omega'). \quad (65)$$

The first integral is

$$\int \mathrm{d}\Omega Y_{\ell,m}(\Omega) Y_{\ell_1,m_1}(\Omega) Y^*_{\ell_1,m_1}(\Omega)$$
$$= \sqrt{\frac{2\ell+1}{4\pi}} \langle \ell, 0; \ell_1, 0 | \ell_1, 0 \rangle \langle \ell, m; \ell_1, m_1 | \ell_1, m_1 \rangle . \quad (66)$$

The Clebsch–Gordan coefficients can only be satisfied for $m = 0$. We then obtain for the direct contribution:

$$E_D = \frac{\mathrm{e}^2}{8\pi\varepsilon_v R} \sum_{\sigma,\sigma'} \times \sum_{\ell_1 \leqslant L_\sigma, m_1} \sum_{\ell_2 \leqslant L_{\sigma'}, m_2}$$
$$\times \sum_{\ell > 0} \{ \langle \ell, 0; \ell_1, 0 | \ell_1, 0 \rangle \langle \ell, 0; \ell_1, m_1 | \ell_1, m_1 \rangle$$
$$\times \langle \ell, 0; \ell_2, 0 | \ell_2, 0 \rangle \langle \ell, 0; \ell_2, m_2 | \ell_2, m_2 \rangle \} . \quad (67)$$

The sum over ℓ is restricted to $\ell < \max[2\ell_1, 2\ell_2]$ and $\ell > 0$.

Some discussion is in order. In the flat electron gas, the direct Coulomb contribution is characterized by a transferred momentum that changes wave vector $\mathbf{k}$ into itself. The only value of the transferred momentum with which this can be achieved is obviously $\mathbf{q} = 0$, since only with this choice we can satisfy $\mathbf{k} + \mathbf{q} = \mathbf{k}$. However, the $\mathbf{q} = 0$ contribution is completely compensated by the positive background in the jellium model, and one is left with only exchange.

In the S2DEG, the direct Coulomb contribution is characterized by a transferred *angular* momentum that changes *angular* momentum state $|\ell, m\rangle$ into itself. So, we look for the angular momentum states $\left|\ell', m'\right\rangle$ that can satisfy $\langle (\ell, m) \otimes (\ell', m') | \ell, m \rangle \neq 0$. Any angular momentum state $\left|\ell', 0\right\rangle$ (with $m' = 0$ and $\ell' \leqslant 2\ell$) can satisfy this relation, not only the $|0, 0\rangle$ state! Indeed, after adding together an angular momentum state $|\ell, m\rangle$ with $\left|\ell', 0\right\rangle$ the resulting state will for any value ℓ' have a non-zero amplitude in the original state $|\ell, m\rangle$.

What takes on the role of the jellium in the S2DEG? There is no positive background any more, but nevertheless, the contribution of the transfer of angular momentum $|0, 0\rangle$ *will not appear in the sum. This particular mode is the s-wave contribution to the direct Coulomb interaction (the part of the Coulomb interaction energy that only depends on R) and that is precisely counteracted by the surface tension term in order to achieve an equilibrium radius for the MEB.*

We note that for the S2DEG, there are still terms left in the direct Coulomb interaction after the removal of the $\ell' = 0$ mode by the background (the surface tension term): namely the term involving a transfer of momentum $\left|\ell', 0\right\rangle$ with $0 < \ell' < 2\ell$. But, we can use that

$$\forall \ell' \neq 0 : \sum_{m=-\ell}^{\ell} \left\langle \ell', 0; \ell, m | \ell, m \right\rangle = 0 \quad (68)$$

to prove that nevertheless the direct Coulomb term vanishes. Indeed, the remaining terms have Clebsch–Gordan coefficients that cancel each other out. Just as was the case for the flat 2DEG, we find that in the S2DEG there is no direct Coulomb contribution.

3.3.3. Exchange energy

The exchange contribution (the Fock term) arises from the second way of pairing up the electrons, namely as

$$E_X = -\frac{\mathrm{e}^2}{2\varepsilon_v R} \sum_{\ell,m} \frac{1}{2\ell+1}$$
$$\times \sum_{\ell_1,m_1,\sigma} \sum_{\ell_2,m_2,\sigma'} \left\langle N_\uparrow N_\downarrow \left| \hat{c}^+_{(\ell_1,m_1)\otimes(\ell,m),\sigma} \hat{c}_{(\ell_2,m_2),\sigma'} \right| N_\uparrow N_\downarrow \right\rangle$$
$$\times \left\langle N_\uparrow N_\downarrow \left| (-1)^m \hat{c}^+_{(\ell_2,m_2)\otimes(\ell,-m),\sigma'} \hat{c}_{(\ell_1,m_1),\sigma} \right| N_\uparrow N_\downarrow \right\rangle . \quad (69)$$

The minus sign appears because of the reordering of the fermionic operators. The first factor is

$$\left\langle N_\uparrow N_\downarrow \left| \hat{c}^+_{(\ell_1,m_1)\otimes(\ell,m),\sigma} \hat{c}_{(\ell_2,m_2),\sigma'} \right| N_\uparrow N_\downarrow \right\rangle$$
$$= \sum_{\ell'=0}^{\infty} \sum_{m'=-\ell'}^{\ell'} \left[\int \mathrm{d}\Omega Y_{\ell,m}(\Omega) Y^*_{\ell',m'}(\Omega) Y_{\ell_1,m_1}(\Omega) \right]$$
$$\times \left\langle N_\uparrow N_\downarrow \left| \widehat{c}^+_{(\ell'm'),\sigma} \hat{c}_{(\ell_2,m_2),\sigma'} \right| N_\uparrow N_\downarrow \right\rangle \delta_{\sigma\sigma'}. \quad (70)$$

The expectation value in the right hand side of the above expression is zero unless $\ell' = \ell_2 \leqslant L_\sigma$ and $m' = m_2$. So we find

$$\left\langle N_\uparrow N_\downarrow \left| \hat{c}^+_{(\ell_1,m_1)\otimes(\ell,m),\sigma} \hat{c}_{(\ell_2,m_2),\sigma'} \right| N_\uparrow N_\downarrow \right\rangle$$
$$= \delta_{\sigma\sigma'} \int \mathrm{d}\Omega Y_{\ell,m}(\Omega) Y^*_{\ell_2,m_2}(\Omega) Y_{\ell_1,m_1}(\Omega) \Theta(\ell_2 \leqslant L_\sigma). \quad (71)$$

Similarly, for the second factor we have

$$\left\langle N_\uparrow N_\downarrow \left| (-1)^m \hat{c}^+_{(\ell_2,m_2)\otimes(\ell,-m),\sigma'} \hat{c}_{(\ell_1,m_1),\sigma} \right| N_\uparrow N_\downarrow \right\rangle$$
$$= \sum_{\ell'=0}^{\infty} \sum_{m'=-\ell'}^{\ell'} \left[\int \mathrm{d}\Omega' Y^*_{\ell',m'}(\Omega') Y^*_{\ell,m}(\Omega') Y_{\ell_2,m_2}(\Omega') \right]$$
$$\times \left\langle N_\uparrow N_\downarrow \left| \widehat{c}^+_{\ell',m'} \hat{c}_{(\ell_1,m_1),\sigma} \right| N_\uparrow N_\downarrow \right\rangle \delta_{\sigma\sigma'} \quad (72)$$
$$= \delta_{\sigma\sigma'} \int \mathrm{d}\Omega' Y^*_{\ell_1,m_1}(\Omega') Y^*_{\ell,m}(\Omega')$$
$$\times Y_{\ell_2,m_2}(\Omega') \Theta(\ell_1 \leqslant L_\sigma). \quad (73)$$

Thus,

$$E_X = -\frac{\mathrm{e}^2}{2\varepsilon_v R} \sum_\ell \frac{1}{2\ell+1} \sum_\sigma \sum_{\ell_1,m_1} \sum_{\ell_2,m_2} \left| \int \mathrm{d}\Omega Y_{\ell,m_2-m_1}(\Omega) \right.$$
$$\left. \times\ Y^*_{\ell_2,m_2}(\Omega) Y_{\ell_1,m_1}(\Omega) \right|^2. \quad (74)$$

The integrations yield Clebsch–Gordan coefficients:

$$E_X = -\frac{\mathrm{e}^2}{8\pi\varepsilon_v R}$$
$$\times \sum_{\ell>0} \sum_\sigma \sum_{\ell_1 \leqslant L_\sigma, m_1} \sum_{\ell_2 \leqslant L_\sigma, m_2} \frac{2\ell_1+1}{2\ell_2+1} |\langle \ell, 0; \ell_1, 0 | \ell_2, 0\rangle$$
$$\times \langle \ell, m_2-m_1; \ell_1, m_1 | \ell_2, m_2\rangle|^2. \quad (75)$$

Hence, we have for the total energy the expression

$$E = \frac{\hbar^2}{2m_\mathrm{e}R^2} \sum_\sigma \frac{L_\sigma\,(L_\sigma+2)\,(L_\sigma+1)^2}{2}$$
$$- \frac{\mathrm{e}^2}{8\pi\varepsilon_v R} \sum_\sigma \sum_{\ell>0} \sum_{\ell_1,m_1}^{\ell_1\leqslant L_\sigma} \sum_{\ell_2,m_2}^{\ell_2\leqslant L_\sigma} \frac{2\ell_1+1}{2\ell_2+1} |\langle \ell, 0; \ell_1, 0 | \ell_2, 0\rangle$$
$$\times \langle \ell, m_2-m_1; \ell_1, m_1 | \ell_2, m_2\rangle|^2. \quad (76)$$

3.3.4. Total energy

Define

$$\Gamma_X(L_F) = \sum_{\ell_1,m_1}^{\ell_1\leqslant L_F} \sum_{\ell_2,m_2}^{\ell_2\leqslant L_F} \sum_{\ell>0} \frac{2\ell_1+1}{2\ell_2+1}$$
$$\times |\langle \ell, 0; \ell_1, 0 | \ell_2, 0\rangle$$
$$\times \langle \ell, m_2-m_1; \ell_1, m_1 | \ell_2, m_2\rangle|^2 \quad (77)$$

and

$$\Gamma_\mathrm{K}(L_F) = \frac{L_F\,(L_F+2)\,(L_F+1)^2}{2}. \quad (78)$$

Using these 'geometrical' functions, which depend only on the Fermi levels of spin up and spin down electrons and are given by a sum over a bunch of Clebsch–Gordan coefficients, we can write the energy as

$$E = \frac{\hbar^2}{2m_\mathrm{e}R^2} \left[\Gamma_\mathrm{K}(L_\uparrow) + \Gamma_\mathrm{K}(L_\downarrow) \right]$$
$$- \frac{\mathrm{e}^2}{8\pi\varepsilon_v R} \left[\Gamma_X(L_\uparrow) + \Gamma_X(L_\downarrow) \right]. \quad (79)$$

We can now proceed to express the energy as a function only of the Fermi levels and one dimensionless parameter which expresses the bubble radius in units of the Bohr radius. We find

$$E(r, L_\uparrow, L_\downarrow) = \frac{\hbar^2}{2m_\mathrm{e}R^2}$$
$$\times \left\{ \Gamma_\mathrm{K}(L_\uparrow) + \Gamma_\mathrm{K}(L_\downarrow) - \frac{R}{a_\mathrm{B}} \left[\Gamma_X(L_\uparrow) + \Gamma_X(L_\downarrow) \right] \right\}. \quad (80)$$

Thus, in expression (80) the energy is given in units $\hbar^2/(2m_\mathrm{e}R^2)$, and is fully determined by R and the Fermi levels. Both Γ_K and Γ_X increase monotonically and concavely as a function of their argument L_σ. The geometric factor for the kinetic energy is larger than that for the exchange contribution, but after multiplication with R, the exchange contribution factor can become stronger. Indeed, the kinetic energy rises as $L_\sigma^4/2$ whereas the exchange contribution rises as λL_σ^3. This is consistent with the limit of a flat two-dimensional electron gas, where the kinetic energy rises as k_F^4 and the exchange energy rises as k_F^3. It is also clear that $\Gamma_\mathrm{K}/\Gamma_X$ increases with increasing L_σ.

When the exchange contribution dominates and spin flip transitions are possible, the electron system on the sphere will tend to polarize. Since the electrons carry a magnetic moment through their spin, this will magnetize the electron system — it is the analogue of the Bloch instability in three dimensions. This instability may be removed or shifted when the magnetic field is taken into account properly, which we will do in Section 3.5.

3.4. Dielectric response

We want to find the response of the electron gas on a probe that couples to the density. For this purpose, we introduce the density operator in its spherical decomposition:

$$\widehat{\rho}_\mathrm{e}(\ell, m) = \int \mathrm{d}\Omega Y_{\ell,m}(\Omega) \widehat{n}_\mathrm{e}(\Omega) \quad (81)$$

with

$$\widehat{n}_\mathrm{e}(\Omega) = \sum_{j=1}^{N} \delta(\Omega - \widehat{\Omega}_j),$$

where $\widehat{\Omega}_j$ is the position operator of electron j. In second quantization, this becomes

$$\widehat{n}_\mathrm{e}(\Omega) = \sum_{\ell,m} \sum_{\ell',m'} Y^*_{\ell',m'}(\Omega) Y_{\ell,m}(\Omega) \widehat{c}^+_{\ell'm'} \widehat{c}_{\ell m}. \quad (82)$$

so that

$$\widehat{\rho}_\mathrm{e}(\ell, m) = \sum_{\ell_1,m_1} \sum_{\ell_2,m_2} \left[\int \mathrm{d}\Omega Y_{\ell,m}(\Omega) \right.$$
$$\left. \times\ Y^*_{\ell_2,m_2}(\Omega) Y_{\ell_1,m_1}(\Omega) \right] \widehat{c}^+_{\ell_2 m_2} \widehat{c}_{\ell_1 m_1}. \quad (83)$$

Again we encounter the triple product of operators (44), so that with (45):

$$\widehat{\rho}_{\mathrm{e}}(\ell,m)=\sum_{\ell'=0}^{\infty}\sum_{m'=-\ell'}^{\ell'}\widehat{c}^{+}_{(\ell',m')\otimes(\ell,m)}\widehat{c}_{\ell',m'}. \tag{84}$$

This allows to rewrite the Hamiltonian of the electron gas as

$$\begin{aligned}\widehat{\mathcal{H}}=&\sum_{\ell=0}^{\infty}\sum_{m=-\ell}^{\ell}\frac{\hbar^2\,\ell(\ell+1)}{2m_{\mathrm{e}}R^2}\widehat{c}^{+}_{\ell m}\widehat{c}_{\ell m}\\&+\frac{\mathrm{e}^2}{2\varepsilon R}\sum_{\ell=0}^{\infty}\sum_{m=-\ell}^{\ell}\frac{1}{2\ell+1}\\&\times\left[\widehat{\rho}_{\mathrm{e}}(\ell,m)\widehat{\rho}^{+}_{\mathrm{e}}(\ell,m)-\mathcal{A}\delta(\ell=0)\right]\end{aligned} \tag{85}$$

with

$$\begin{aligned}\mathcal{A}=&\sum_{\ell_1=0}^{L_F}\sum_{m_1=-\ell_1}^{\ell_1}\sum_{\ell=0}^{2\ell_1}[\langle\ell,0;\ell_1,0|\ell_1,0\rangle\\&\times\langle\ell,0;\ell_1,m_1|\ell_1,m_1\rangle]^2.\end{aligned} \tag{86}$$

The Coulomb part, rewritten with the density operator, is again analogous to the result for a flat two-dimensional electron gas:

$$\widehat{\mathcal{H}}^{\text{plane wave}}_{\text{coul}}=\sum_{\mathbf{k}_1}\sum_{\mathbf{k}_2}\sum_{\mathbf{q}}v(\mathbf{q})\left[\widehat{\rho}_{\mathbf{q}}\widehat{\rho}^{+}_{\mathbf{q}}-N\delta(\mathbf{q}=0)\right]. \tag{87}$$

To investigate the response of this system, we introduce an external charge density (e.g. from an ion) in the S2DEG. On the spherical surface, this external charge can be decomposed as

$$\rho_{\mathrm{ext}}(\Omega,t)=\int_{-\infty}^{\infty}\mathrm{d}\omega\sum_{\ell,m}\rho_{\mathrm{ext}}(\ell,m;\omega)Y^{*}_{\ell m}(\Omega)\mathrm{e}^{-\mathrm{i}\omega t}. \tag{88}$$

The Coulomb interaction between the external charge and the S2DEG can be calculated analogously to our previous analysis:

$$\widehat{\mathcal{H}}_{\mathrm{perturb}}(t)=\sum_{\ell=0}^{\infty}\sum_{m=-\ell}^{\ell}V_{\ell}\widehat{\rho}_{\mathrm{e}}(\ell,m;t)\rho^{*}_{\mathrm{ext}}(\ell,m;t)+c.c. \tag{89}$$

$$\text{with } V_{\ell}=\frac{\mathrm{e}^2}{2\varepsilon R}\frac{1}{2\ell+1}. \tag{90}$$

The perturbation Hamiltonian is Hermitian by virtue of the complex conjugate term. In linear response theory (valid for a weak perturbation), each spherical component of this problem can be treated separately. To get the general result we can suffice by studying the effect of

$$\widehat{\mathcal{H}}^{\ell m,\omega}_{\mathrm{perturb}}(t)=V_{\ell}\rho^{*}_{\mathrm{ext}}(\ell,m;\omega)\mathrm{e}^{\mathrm{i}\omega t}\mathrm{e}^{\delta t}\times\widehat{\rho}_{\mathrm{e}}(\ell,m;t)+c.c. \tag{91}$$

The factor $\mathrm{e}^{\delta|t|}$ has been added to switch on the perturbation adiabatically. Note that this form of the perturbation Hamiltonian is generic for perturbations which couple to the density of the electrons in the S2DEG.

In equilibrium, the expectation value for the density operator is supposed to be homogeneous; i.e. $\langle\widehat{\rho}_{\mathrm{e}}(\ell,m;t)\rangle=0$ for $\ell,m\neq0$. When a perturbation coupling to the density is present, it will induce a redistribution of the electron density, and lead to a non-zero expectation value for $\widehat{\rho}_{\mathrm{e}}$, the induced density

$$\rho_{\mathrm{ind}}(\ell,m;t)=\langle\widehat{\rho}_{\mathrm{e}}(\ell,m;t)\rangle-\langle\widehat{\rho}_{\mathrm{e}}(\ell,m;-\infty)\rangle. \tag{92}$$

Here $\langle\widehat{\rho}_{\mathrm{e}}(\ell,m;-\infty)\rangle$ is the equilibrium density since we switched on the perturbation adiabatically. The familiar definition of the dielectric function is then

$$\varepsilon(\ell,m;\omega)=\frac{\rho_{\mathrm{ext}}(\ell,m;\omega)}{\rho_{\mathrm{ext}}(\ell,m;\omega)-\rho_{\mathrm{ind}}(\ell,m;\omega)}. \tag{93}$$

or

$$\frac{1}{\varepsilon(\ell,m;\omega)}=1-\frac{\rho_{\mathrm{ind}}(\ell,m;\omega)}{\rho_{\mathrm{ext}}(\ell,m;\omega)}. \tag{94}$$

In the next subsection, linear response theory is used to express ρ_{ind} as a function of the microscopic density–density Green's function of the system. Then, the density–density Green's function is calculated diagrammatically to lowest order, and finally a Dyson resummation is used to provide the RPA result for the dielectric function.

3.4.1. Linear response

The main question of response theory is: how will the electron density $\widehat{\rho}_{\mathrm{e}}$ evolve in time due to a perturbation? To find the answer, Kubo's formalism can be used. However, in the spherical case, this poses a problem since the commutator relations for the density operator are complicated (because addition of two angular momenta leads to a set of possible angular momenta, whereas addition of two momenta leads to one total momentum). To avoid this complication, let's try resorting to standard time dependent perturbation theory.

The many-body wave function of the S2DEG can be written as a linear superposition of many-body eigenkets $|\Psi_n\rangle$ of the unperturbed Hamiltonian $\widehat{\mathcal{H}}$, Eq. (85):

$$\Psi(t)=\sum_{n}|\Psi_n\rangle\,\mathrm{e}^{-\mathrm{i}E_nt/\hbar}a_n(t). \tag{95}$$

In this expression, E_n denotes the energy of the many-body eigenket $|\Psi_n\rangle$. The corresponding eigenfunction is $\langle\mathbf{r}_1,\mathbf{r}_2,\mathbf{r}_3,\ldots,\mathbf{r}_N|\Psi_n\rangle=\Psi_n(\mathbf{r}_1,\mathbf{r}_2,\mathbf{r}_3,\ldots,\mathbf{r}_N)$. Let $|\Psi_0\rangle$ correspond to the ground state, and E_0 to the ground state energy. The initial condition on the coefficients a_n is that $a_n(t\to-\infty)=1$ for $n=0$ and $a_n(t\to-\infty)=0$ for $n>0$. This affirms that without the perturbation of the external charge, the S2DEG is in its ground state. To first order in the perturbation, the coefficients $a_n(t)$ are given by

$$a_0(t)=1-\frac{\mathrm{i}}{\hbar}\int_{-\infty}^{t}\left\langle\Psi_0\left|\widehat{\mathcal{H}}^{\ell m,\omega}_{\mathrm{perturb}}(t')\right|\Psi_0\right\rangle\mathrm{d}t' \tag{96}$$

$$a_{n\neq0}(t)=-\frac{\mathrm{i}}{\hbar}\int_{-\infty}^{t}\left\langle\Psi_n\left|\widehat{\mathcal{H}}^{\ell m,\omega}_{\mathrm{perturb}}(t')\right|\Psi_0\right\rangle\mathrm{d}t'. \tag{97}$$

The time dependence of the expectation value of the spherical components of the density is given by

$$\rho_{\mathrm{e}}(\ell,m;t)=\langle\Psi(t)|\widehat{\rho}_{\mathrm{e}}(\ell,m)|\Psi(t)\rangle \tag{98}$$

$$=\sum_{n,m}\langle\Psi_n|\widehat{\rho}_{\mathrm{e}}(\ell,m)|\Psi_m\rangle\,\mathrm{e}^{-\mathrm{i}(E_m-E_n)t/\hbar}a_m(t)a^{*}_n(t). \tag{99}$$

Substituting (96) and (97) in (99) to first order in the perturbation, we find

$$\rho_e(\ell,m;t) \approx \rho_e(\ell,m;-\infty) + \sum_{n\neq 0} \langle \Psi_n | \widehat{\rho}_e(\ell,m) | \Psi_0 \rangle \, e^{-i(E_0-E_n)t/\hbar} a_n^*(t) + \sum_{n\neq 0} \langle \Psi_0 | \widehat{\rho}_e(\ell,m) | \Psi_n \rangle \, e^{i(E_0-E_n)t/\hbar} a_n(t). \tag{100}$$

The shorthand notation $(E_n - E_0)/\hbar = \omega_{n0}$ will be used. To proceed further, the coefficients $a_{n\neq 0}(t)$ must be evaluated:

$$a_{n\neq 0}(t) = -\frac{V_\ell}{\hbar}\left[\frac{\rho^*_{ext}(\ell,m;\omega)\,\langle \Psi_n | \widehat{\rho}_e(\ell,m) | \Psi_0\rangle \, e^{i(\omega_{n0}+\omega-i\delta)t}}{\omega_{n0}+\omega-i\delta} + \frac{\rho_{ext}(\ell,m;\omega)\,\langle \Psi_n | \widehat{\rho}^+_e(\ell,m) | \Psi_0\rangle e^{i(\omega_{n0}-\omega-i\delta)t}}{\omega_{n0}-\omega-i\delta}\right], \tag{101}$$

where $V_\ell = V_\ell^*$ was used (expression (90)). The (101) for the coefficients $a_{n\neq 0}$ is substituted in (100), resulting in

$$\rho_e(\ell,m;t) = \rho_e(\ell,m;-\infty) - \frac{V_\ell \rho_{ext}(\ell,m;\omega)}{\hbar} e^{-i\omega t+\delta t} \times \sum_n \left[\frac{|\langle \Psi_n | \widehat{\rho}_e(\ell,m) | \Psi_0\rangle|^2}{\omega_{n0}-\omega-i\delta} + \frac{|\langle \Psi_0 | \widehat{\rho}^+_e(\ell,m) | \Psi_n\rangle|^2}{\omega_{n0}+\omega+i\delta}\right]. \tag{102}$$

The term $\rho_e(\ell,m;-\infty)$ is the unperturbed charge density. The remaining terms represent the charge density induced by the presence of the external charge. This induced charge density screens the external field. Let's denote this induced charge density $\rho_{ind}(\ell,m;t) = \rho_e(\ell,m;t) - \rho_e(\ell,m;-\infty)$. It is given by

$$\rho_{ind}(\ell,m;t) = \frac{V_\ell}{\hbar}\rho_{ext}(\ell,m;\omega) e^{-i\omega t+\delta t} \mathcal{D}_R(\ell,m;\omega), \tag{103}$$

with

$$\mathcal{D}_R(\ell,m;\omega) = \sum_n \left[\frac{|\langle \Psi_n | \widehat{\rho}_{ind}(\ell,m) | \Psi_0\rangle|^2}{\omega-\omega_{n0}+i\delta} - \frac{|\langle \Psi_0 | \widehat{\rho}_{ind}(\ell,m) | \Psi_n\rangle|^2}{\omega_{n0}+\omega+i\delta}\right]. \tag{104}$$

The reason for introducing the notation $\mathcal{D}_R$ is that we relate the dielectric response to the density–density Green's function $\mathcal{D}$.

$$\mathcal{D}(\ell,m;t) = -i\langle \Psi_0 | \mathcal{T}\left\{\widehat{\rho}_{ind}(\ell,m;t)\widehat{\rho}^+_{ind}(\ell,m;0)\right\} | \Psi_0\rangle. \tag{105}$$

This is the amplitude that a density fluctuation, created at time $t = 0$, will be present at a later time t. Then the retarded density–density Green's function is

$$\mathcal{D}_R(\ell,m;t) = \begin{cases} -i\langle \Psi_0 | \left[\widehat{\rho}_{ind}(\ell,m;t), \widehat{\rho}^+_{ind}(\ell,m;0)\right] | \Psi_0\rangle & t>0 \\ 0 & t<0. \end{cases} \tag{106}$$

Its time Fourier transform is exactly expression (104) obtained in our study of the response of the density to an external probe charge. The density–density Green's function also allows to define the structure factor of the S2DEG as

$$S(\ell,m;\omega) = \sum_n |\langle \Psi_0 | \widehat{\rho}_{ind}(\ell,m;0) | \Psi_n\rangle|^2 \, \delta(\omega-\omega_{n0}), \tag{107}$$

so that

$$\mathcal{D}_R(\ell,m;\omega) = \int d\omega' S(\ell,m;\omega') \times \left(\frac{1}{\omega-\omega'+i\delta} - \frac{1}{\omega+\omega'+i\delta}\right). \tag{108}$$

Substituting this (108) into the expression (103) for the induced charge density yields

$$\rho_{ind}(\ell,m;t) = \frac{V_\ell}{\hbar}\rho_{ext}(\ell,m;\omega)e^{-i\omega t}\int d\omega' \times \left(\frac{S(\ell,m;\omega')}{\omega-\omega'+i\delta} - \frac{S(\ell,m;\omega')}{\omega+\omega'+i\delta}\right). \tag{109}$$

Using Plemelj's identity $1/(x \pm i\varepsilon) = \mathcal{P}(1/x) \mp i\pi\delta(x)$ we find the spherical electron gas version of the important relation between the dielectric function and the structure factor:

$$\mathrm{Im}\left[\frac{\rho_{ind}(\ell,m;t)}{\rho_{ext}(\ell,m;\omega)e^{-i\omega t}}\right] = -\frac{V_\ell}{\hbar}\pi S(\ell,m;\omega) \tag{110}$$

$$\Rightarrow \mathrm{Im}\left[\frac{1}{\varepsilon(\mathbf{k},\omega)}\right] = -\frac{\pi e^2}{2\varepsilon_{vac}\hbar R}\frac{S(\ell,m;\omega)}{2\ell+1}. \tag{111}$$

An expression for the dielectric function can be derived from (103) and (94):

$$\frac{1}{\varepsilon(\ell,m;\omega)} = 1 + \frac{V_\ell}{\hbar}\mathcal{D}_R(\ell,m;\omega), \tag{112}$$

so that

$$\frac{1}{\varepsilon(\ell,m;\omega)} = 1 + \frac{e^2}{2\varepsilon_{vac}\hbar R}\frac{1}{2\ell+1}\mathcal{D}_R(\ell,m;\omega), \tag{113}$$

with ε_{vac} the permittivity of vacuum, and $\mathcal{D}_R$ given by expression (104).

3.4.2. Random phase approximation

The response properties are governed by the density–density fluctuations, through the Green's function

$$\mathcal{D}(\ell,m;t) = -i\langle \Psi_0 | \mathcal{T}\left\{\widehat{\rho}_{ind}(\ell,m;t)\widehat{\rho}^+_{ind}(\ell,m;0)\right\} | \Psi_0\rangle. \tag{114}$$

This expectation value (114) in the interacting system can be written as a sum of Feynman diagrams, resulting from the expansion of the exponentials in the time dependent operator

$$\widehat{\rho}_{ind}(\ell,m;t) = e^{i\widehat{\mathcal{H}}t/\hbar}\widehat{\rho}_{ind}(\ell,m;0)e^{-i\widehat{\mathcal{H}}t/\hbar}. \tag{115}$$

Let's start with the lowest order diagram, resulting in $\mathcal{D}_0$. Expanding the densities again, we find

$$\widehat{\rho}_{ind}(\ell,m;t)\widehat{\rho}^+_{ind}(\ell,m;0)$$

$$= \sum_{\ell_1,m_1} \widehat{c}^{+}_{(\ell_1,m_1)\otimes(\ell,m)}(t)\widehat{c}_{\ell_1,m_1}(t) \times \sum_{\ell_2,m_2} (-1)^m \widehat{c}^{+}_{(\ell_2,m_2)\otimes(\ell,-m)}(0)\widehat{c}_{\ell_2,m_2}(0). \quad (116)$$

Writing out the creation operators:

$$\begin{aligned}\left\langle \Psi_0 \left| \mathcal{T}\left\{\widehat{\rho}_{\rm ind}(\ell,m;t)\widehat{\rho}^{+}_{\rm ind}(\ell,m;0)\right\}\right| \Psi_0\right\rangle &= \sum_{\ell_1,m_1}\sum_{\ell_2,m_2}\sum_{\ell_3,m_3}\sum_{\ell_4,m_4}\int \mathrm{d}\Omega \int \mathrm{d}\Omega' \\ &\times (-1)^m [Y_{\ell,m}(\Omega')Y^*_{\ell_3,m_3}(\Omega')Y_{\ell_1,m_1}(\Omega')] \\ &\times [Y_{\ell,-m}(\Omega)Y^*_{\ell_4,m_4}(\Omega)Y_{\ell_2,m_2}(\Omega)] \\ &\times \langle \Psi_0|\mathcal{T}\{\widehat{c}^{+}_{\ell_3m_3}(t)\widehat{c}_{\ell_1,m_1}(t)\widehat{c}^{+}_{\ell_4m_4}(0)\widehat{c}_{\ell_2,m_2}(0)\}|\Psi_0\rangle. \quad (117)\end{aligned}$$

The expectation value of the time ordered product of four operators can be decomposed in product of single-particle Green's functions using Wick's theorem:

$$\begin{aligned}(\text{Wick}:) \left\langle \Psi_0 \left| \mathcal{T}\left\{\widehat{c}^{+}_{\ell_3m_3}(t)\widehat{c}_{\ell_1,m_1}(t)\widehat{c}^{+}_{\ell_4m_4}(0)\widehat{c}_{\ell_2,m_2}(0)\right\}\right| \Psi_0\right\rangle &= \left\langle \Psi_0 \left| \mathcal{T}\left\{\widehat{c}_{\ell_1,m_1}(t)\widehat{c}^{+}_{\ell_3m_3}(t)\right\}\right| \Psi_0\right\rangle \\ &\times \left\langle \Psi_0 \left| \mathcal{T}\left\{\widehat{c}_{\ell_2,m_2}(0)\widehat{c}^{+}_{\ell_4m_4}(0)\right\}\right| \Psi_0\right\rangle \\ &- \left\langle \Psi_0 \left| \mathcal{T}\left\{\widehat{c}_{\ell_2,m_2}(0)\widehat{c}^{+}_{\ell_3m_3}(t)\right\}\right| \Psi_0\right\rangle \\ &\times \left\langle \Psi_0 \left| \mathcal{T}\left\{\widehat{c}_{\ell_1,m_1}(t)\widehat{c}^{+}_{\ell_4m_4}(0)\right\}\right| \Psi_0\right\rangle.\end{aligned}$$

The factors can be identified as single-particle Green's functions, so that

$$\begin{aligned}\left\langle \Psi_0 \left| \mathcal{T}\left\{\widehat{c}^{+}_{\ell_3m_3}(t)\widehat{c}_{\ell_1,m_1}(t)\widehat{c}^{+}_{\ell_4m_4}(0)\widehat{c}_{\ell_2,m_2}(0)\right\}\right| \Psi_0\right\rangle &= -G_0(\ell_3,m_3;0|\ell_1,m_1,0)\,G_0(\ell_4,m_4;0|\ell_2,m_2,0) \\ &+ G_0(\ell_3,m_3;t|\ell_2,m_2,0)\,G_0(\ell_4,m_4;-t|\ell_1,m_1,0). \quad (118)\end{aligned}$$

The first line is time independent, and will only contribute a $\omega = 0$ term to the frequency dependence of the response. We will omit it from further considerations, keeping in mind that the $\omega = 0$ response is a special case. We find:

$$\begin{aligned}\mathcal{D}_0(\ell,m;t) = -\mathrm{i}\sum_{\ell_1,m_1}\sum_{\ell_2,m_2}\sum_{\ell_3,m_3}\sum_{\ell_4,m_4}\int \mathrm{d}\Omega \int \mathrm{d}\Omega'(-1)^m &\times [Y_{\ell,m}(\Omega')Y^*_{\ell_3,m_3}(\Omega')Y_{\ell_1,m_1}(\Omega')] \\ &\times \left[Y_{\ell,-m}(\Omega)Y^*_{\ell_4,m_4}(\Omega)Y_{\ell_2,m_2}(\Omega)\right] \\ &\times \mathrm{i}G_0(\ell_3,m_3;t|\ell_2,m_2,0) \\ &\times \mathrm{i}G_0(\ell_4,m_4;-t|\ell_1,m_1,0). \quad (119)\end{aligned}$$

The frequency dependent case is

$$\begin{aligned}\mathcal{D}_0(\ell,m;\omega) = \mathrm{i}\sum_{\ell_1,m_1}\sum_{\ell_2,m_2}\sum_{\ell_3,m_3}\sum_{\ell_4,m_4}\int \mathrm{d}\Omega \int \mathrm{d}\Omega'(-1)^m &\times \left[Y_{\ell,m}(\Omega')Y^*_{\ell_3,m_3}(\Omega')Y_{\ell_1,m_1}(\Omega')\right] \\ &\times \left[Y_{\ell,-m}(\Omega)Y^*_{\ell_4,m_4}(\Omega)Y_{\ell_2,m_2}(\Omega)\right] \\ &\times \int \mathrm{d}t\mathrm{e}^{\mathrm{i}\omega t}G_0(\ell_3,m_3;t|\ell_2,m_2,0)\end{aligned}$$

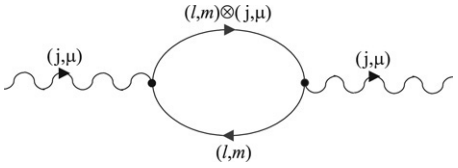

Fig. 16. The polarization diagram (also called the 'bubble' diagram) on a spherical surface.

$$\times G_0(\ell_4,m_4;-t|\ell_1,m_1,0). \quad (120)$$

The interpretation of this function is shown in Fig. 16. The two Green's functions form a polarization diagram, analogous to the polarization diagrams in the treatment of the flat electron gas. Let's focus on the integral in the last line of expression (120)

$$\begin{aligned}\mathcal{J} &= \int \mathrm{d}t\mathrm{e}^{\mathrm{i}\omega t}G_0(\ell_3,m_3;t|\ell_2,m_2,0) \\ &\times G_0(\ell_4,m_4;-t|\ell_1,m_1,0) \\ &= \int \frac{\mathrm{d}\omega'}{2\pi}G_0(\ell_3,m_3;\ell_2,m_2|\omega')G_0(\ell_4,m_4;\ell_1,m_1|\omega'-\omega).\end{aligned}$$

In this expression, we can substitute the result for the zeroth-order Green's function G_0,

$$G_0(\ell',m';\ell,m|\omega) = \delta_{\ell,\ell'}\delta_{m,m'}\left\{\frac{1-n(\ell m)}{\omega - E_{\ell m}+\mathrm{i}\varepsilon} + \frac{n(\ell m)}{\omega - E_{\ell m}-\mathrm{i}\varepsilon}\right\}, \quad (121)$$

so that, omitting the delta functions $\delta_{\ell_1,\ell_4}\delta_{m_1,m_4}\times\delta_{\ell_2,\ell_3}\delta_{m_2,m_3}$, one finds the factor:

$$\begin{aligned}\mathcal{J} = \int \frac{\mathrm{d}\omega'}{2\pi}&\left\{\frac{1-n(\ell_2m_2)}{\omega' - E_{\ell_2m_2}+\mathrm{i}\varepsilon} + \frac{n(\ell_2m_2)}{\omega' - E_{\ell_2m_2}-\mathrm{i}\varepsilon}\right\} \\ &\times \left\{\frac{1-n(\ell_1m_1)}{\omega' - \omega - E_{\ell_1m_1}+\mathrm{i}\varepsilon} + \frac{n(\ell_1m_1)}{\omega' - \omega - E_{\ell_1m_1}-\mathrm{i}\varepsilon}\right\}. \quad (122)\end{aligned}$$

We close the contour in the upper half complex plane so that only the contributions with poles in that half plane count.

$$\begin{aligned}\mathcal{J} = \int \frac{\mathrm{d}\omega'}{2\pi}&\left\{\frac{n(\ell_2m_2)}{\omega' - E_{\ell_2m_2}-\mathrm{i}\varepsilon}\frac{1-n(\ell_1m_1)}{\omega' - \omega - E_{\ell_1m_1}+\mathrm{i}\varepsilon}\right. \\ &+ \frac{1-n(\ell_2m_2)}{\omega' - E_{\ell_2m_2}+\mathrm{i}\varepsilon}\frac{n(\ell_1m_1)}{\omega' - \omega - E_{\ell_1m_1}-\mathrm{i}\varepsilon} \\ &\left.+ \frac{n(\ell_2m_2)}{\omega' - E_{\ell_2m_2}-\mathrm{i}\varepsilon}\frac{n(\ell_1m_1)}{\omega' - \omega - E_{\ell_1m_1}-\mathrm{i}\varepsilon}\right\}. \quad (123)\end{aligned}$$

The first term is

$$\int \frac{\mathrm{d}\omega'}{2\pi}\frac{n(\ell_2m_2)}{\omega' - E_{\ell_2m_2}-\mathrm{i}\varepsilon}\frac{1-n(\ell_1m_1)}{\omega' - \omega - E_{\ell_1m_1}+\mathrm{i}\varepsilon} = \frac{n(\ell_2m_2)[1-n(\ell_1m_1)]}{E_{\ell_2m_2} - \omega - E_{\ell_1m_1}+2\mathrm{i}\varepsilon}. \quad (124)$$

The second term is

$$\int \frac{\mathrm{d}\omega'}{2\pi}\frac{1-n(\ell_2m_2)}{\omega' - E_{\ell_2m_2}+\mathrm{i}\varepsilon}\frac{n(\ell_1m_1)}{\omega' - \omega - E_{\ell_1m_1}-\mathrm{i}\varepsilon} = \frac{[1-n(\ell_2m_2)]n(\ell_1m_1)}{\omega + E_{\ell_1m_1} - E_{\ell_2m_2}+2\mathrm{i}\varepsilon}. \quad (125)$$

The third term is, in the case $\omega \neq E_{\ell_2 m_2} - E_{\ell_1 m_1}$

$$\int \frac{\mathrm{d}\omega'}{2\pi} \frac{n(\ell_2 m_2)}{\omega' - E_{\ell_2 m_2} - \mathrm{i}\varepsilon} \frac{n(\ell_1 m_1)}{\omega' - \omega - E_{\ell_1 m_1} - \mathrm{i}\varepsilon} \tag{126}$$

$$= \frac{n(\ell_2 m_2) n(\ell_1 m_1)}{\omega + E_{\ell_1 m_1} - E_{\ell_2 m_2}} + \frac{n(\ell_2 m_2) n(\ell_1 m_1)}{E_{\ell_2 m_2} - \omega - E_{\ell_1 m_1}} = 0. \tag{127}$$

If $\omega = E_{\ell_2 m_2} - E_{\ell_1 m_1}$, then

$$\int \frac{\mathrm{d}\omega'}{2\pi} \frac{n(\ell_2 m_2) n(\ell_1 m_1)}{(\omega' - E_{\ell_2 m_2} - \mathrm{i}\varepsilon)^2} = 0. \tag{128}$$

This is zero since the second-order pole has a residue proportional to $\mathrm{d}[n(\ell_2 m_2) n(\ell_1 m_1)]/\mathrm{d}\omega = 0$. Another reason is that we could have chosen to close the contour along the lower half of the complex plane and then both poles of this last term would lie on the same (upper) half. We have, in total

$$\mathcal{J} = \frac{[1 - n(\ell_2 m_2)] n(\ell_1 m_1)}{\omega + E_{\ell_1 m_1} - E_{\ell_2 m_2} + \mathrm{i}\eta} - \frac{n(\ell_2 m_2)[1 - n(\ell_1 m_1)]}{\omega + E_{\ell_1 m_1} - E_{\ell_2 m_2} - \mathrm{i}\eta} \tag{129}$$

where $\eta = 2\varepsilon$ is just another infinitesimal number. Remember that for the response we will need the retarded density–density Green's function $\mathcal{D}_R$. However, since $\mathcal{D}_R = \mathrm{Re}[\mathcal{D}] + \mathrm{isgn}(\omega)\mathrm{Im}[\mathcal{D}]$ (see e.g. Ref. [61], p. 176), so that

$$\mathcal{J} = \frac{[1 - n(\ell_2 m_2)] n(\ell_1 m_1)}{\omega + E_{\ell_1 m_1} - E_{\ell_2 m_2} + \mathrm{i}\eta} - \frac{n(\ell_2 m_2)[1 - n(\ell_1 m_1)]}{\omega + E_{\ell_1 m_1} - E_{\ell_2 m_2} + \mathrm{i}\eta} \tag{130}$$

$$= -\frac{n(\ell_2 m_2) - n(\ell_1 m_1)}{\omega - (E_{\ell_2 m_2} - E_{\ell_1 m_1}) + \mathrm{i}\eta}. \tag{131}$$

We find

$$\begin{aligned} \mathcal{D}_{R,0}(\ell, m; \omega) = & \sum_{\ell_1, m_1} \sum_{\ell_2, m_2} \sum_{\ell_3, m_3} \sum_{\ell_4, m_4} \delta_{\ell_1, \ell_4} \delta_{m_1, m_4} \delta_{\ell_2, \ell_3} \delta_{m_2, m_3} \\ & \times \int \mathrm{d}\Omega \int \mathrm{d}\Omega' (-1)^m \\ & \times [Y_{\ell,m}(\Omega') Y^*_{\ell_3, m_3}(\Omega') Y_{\ell_1, m_1}(\Omega')] \\ & \times \left[Y_{\ell,-m}(\Omega) Y^*_{\ell_4, m_4}(\Omega) Y_{\ell_2, m_2}(\Omega) \right] \\ & \times \frac{n(\ell_2 m_2) - n(\ell_1 m_1)}{\omega - (E_{\ell_2 m_2} - E_{\ell_1 m_1}) + \mathrm{i}\eta}. \end{aligned} \tag{132}$$

The delta functions enable the performance of some of the summations:

$$\begin{aligned} \mathcal{D}_{R,0}(\ell, m; \omega) = & \sum_{\ell_1, m_1} \sum_{\ell_2, m_2} \int \mathrm{d}\Omega (-1)^m \\ & \times \left[Y_{\ell,-m}(\Omega) Y^*_{\ell_1, m_1}(\Omega) Y_{\ell_2, m_2}(\Omega) \right] \\ & \times \int \mathrm{d}\Omega' \left[Y_{\ell,m}(\Omega') Y^*_{\ell_2, m_2}(\Omega') Y_{\ell_1, m_1}(\Omega') \right] \\ & \times \frac{n(\ell_2, m_2) - n(\ell_1, m_1)}{\omega - (E_{\ell_2, m_2} - E_{\ell_1, m_1}) + \mathrm{i}\eta}. \end{aligned} \tag{133}$$

The Ω'-integration means that (ℓ_2, m_2) must result from the addition of the angular moment (ℓ_1, m_1) and (ℓ, m). The Ω-integration means that (ℓ_1, m_1) must result from the addition of (ℓ_2, m_2) and $(\ell, -m)$. This imposes the conditions $m_2 = m_1 + m$, $|\ell - \ell_1| \leqslant \ell_2$ and $\ell_2 \leqslant \ell + \ell_1$. The final result for the lowest order retarded density–density Green's function is

$$\begin{aligned} \mathcal{D}_{R,0}(\ell, m; \omega) = & \sum_{\ell_1, m_1} \sum_{\ell_2 = |\ell - \ell_1|}^{\ell + \ell_1} \frac{(2\ell_1 + 1)(2\ell + 1)}{4\pi(2\ell_2 + 1)} |\langle \ell, 0; \ell_1, 0 | \ell_2, 0 \rangle|^2 \\ & \times |\langle \ell, 0; \ell_1, m_1 | \ell_2, m_2 \rangle|^2 \\ & \times \frac{n(\ell_2, m_1 + m) - n(\ell_1, m_1)}{\omega - (E_{\ell_2, m_1 + m} - E_{\ell_1, m_1}) + \mathrm{i}\eta}. \end{aligned} \tag{134}$$

As usual we make the comparison with the plane wave result

$$\mathcal{D}_{R,0}(\mathbf{q}, \omega) = \sum_{\mathbf{k}} \frac{n(\mathbf{k} + \mathbf{q}) - n(\mathbf{k})}{\omega - (E_{\mathbf{k}+\mathbf{q}} - E_{\mathbf{k}}) + \mathrm{i}\eta}. \tag{135}$$

The analogy, replacing wave vector addition with angular momentum addition, is again obvious; as is the appearance of Clebsch–Gordan coefficients tackling the summation of the angular momenta.

3.4.3. RPA dielectric function

The RPA dielectric function on the sphere can then be derived from the result for the zeroth-order density–density Green's function $\mathcal{D}_{R,0}$, expression (134) and with $E_{\ell m} = \hbar^2 \ell(\ell + 1)/(2m_\mathrm{e} R^2)$. The spherical decomposition of the Coulomb interaction can be denoted by

$$U_0(\ell) = \frac{\mathrm{e}^2}{2\varepsilon_{\mathrm{vac}} \hbar R} \frac{1}{2\ell + 1}.$$

Using the zeroth-order result $\mathcal{D}_{R,0}$ in the dielectric function (113) would give

$$\varepsilon_{\text{Hartree–Fock}}(\ell, m; \omega) = \left[1 + U_0(\ell) \mathcal{D}_{R,0}(\ell, m; \omega) \right]^{-1}. \tag{136}$$

This result is known as the Hartree–Fock approximation to the dielectric function.

The *Random Phase Approximation* (RPA) is an approximation to the sum over all Feynman diagrams needed to calculate the density–density Green's function $\mathcal{D}_R$. The approximation consists in only summing a subset of those diagrams, which can be summed analytically. This subset leads to

$$\mathcal{D}_R \approx \mathcal{D}_{R,0} + \mathcal{D}_{R,0} U_0 \mathcal{D}_{R,0} + \mathcal{D}_{R,0} U_0 \mathcal{D}_{R,0} U_0 \mathcal{D}_{R,0} + \cdots \tag{137}$$

$$= \mathcal{D}_{R,0}[1 + U_0 \mathcal{D}_{R,0} + (U_0 \mathcal{D}_{R,0})^2 + \cdots] \tag{138}$$

$$= \frac{\mathcal{D}_{R,0}}{1 - U_0 \mathcal{D}_{R,0}}. \tag{139}$$

Using this, we find for the dielectric function

$$\frac{1}{\varepsilon_{\mathrm{RPA}}(\ell, m; \omega)} = 1 + U_0 \mathcal{D}_R = 1 + \frac{U_0 \mathcal{D}_{R,0}}{1 - U_0 \mathcal{D}_{R,0}} = \frac{1}{1 - U_0 \mathcal{D}_{R,0}} \tag{140}$$

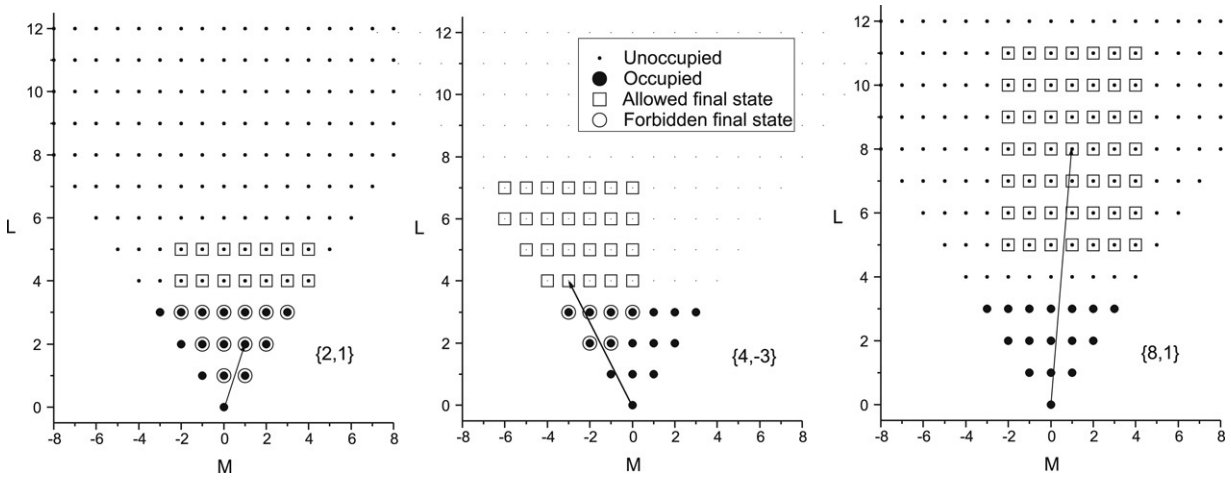

Fig. 17. Single-particle excitations and the Fermi sea of a S2DEG (from Ref. [60]).

$$\Rightarrow \varepsilon_{\mathrm{RPA}}(\ell, m; \omega) = 1 - U_0(\ell)\mathcal{D}_{R,0}(\ell, m; \omega), \tag{141}$$

which leads to

$$\varepsilon_{\mathrm{RPA}}(\ell, m; \omega) = 1 - \frac{\mathrm{e}^2}{2\varepsilon_{\mathrm{vac}}\hbar R}\frac{1}{2\ell+1}\mathcal{D}_{R,0}(\ell, m; \omega) \tag{142}$$

with $\mathcal{D}_{R,0}$ given by (134).

The interpretation of this result is found by considering Plemelj's rule:

$$\mathrm{Im}\,\frac{1}{\omega - (E_{L,m+m'} - E_{\ell',m'}) + \mathrm{i}\eta} = -\mathrm{i}\pi\delta[\omega - (E_{L,m+m'} - E_{\ell',m'})] \tag{143}$$

$$\mathrm{Re}\,\frac{1}{\omega - (E_{L,m+m'} - E_{\ell',m'}) + \mathrm{i}\eta} = \mathcal{P}\left[\frac{1}{\omega - (E_{L,m+m'} - E_{\ell',m'})}\right] \tag{144}$$

where $\mathcal{P}$ means the prime value integral. The imaginary part becomes

$$\begin{aligned}\mathrm{Im}\,\varepsilon_{\mathrm{RPA}}(\ell, m; \omega) &= \pi U_0(\ell)\sum_{\ell' m'}\sum_{L=|\ell-\ell'|}^{\ell+\ell'}\frac{(2\ell+1)(2\ell'+1)}{4\pi(2L+1)}n(\ell' m') \\ &\quad\times[1 - n(L, m+m')] \\ &\quad\times\left|\langle \ell, 0; \ell', 0|L, 0\rangle\right|^2\left|\langle \ell, m; \ell', m'|L, m+m'\rangle\right|^2 \\ &\quad\times\delta[\omega - (E_{L,m+m'} - E_{\ell',m'})].\end{aligned} \tag{145}$$

From (111), we know that the structure factor is given by

$$S(\ell, m; \omega) = -\frac{1}{\pi U_0(\ell)}\frac{\mathrm{Im}[\varepsilon]}{(\mathrm{Re}[\varepsilon])^2 + (\mathrm{Im}[\varepsilon])^2}. \tag{146}$$

The structure factor $S(\ell, m; \omega)$ can be interpreted as a probability function. It is the probability that an excitation can be created in the interacting electron system so that this excitation has angular momentum (ℓ, m) and energy $\hbar\omega$ [62]. We find that $S(\ell, m; \omega)$ is zero, unless adding the angular momentum (ℓ, m) can excite a single electron from an occupied state $n(\ell' m')$ into an unoccupied state $1 - n(L, m + m')$. These are the single-particle excitations (called the "Landau Continuum" in the case of the flat electron gas). Fig. 17 illustrate the concept of single-particle excitations.

For angular momentum transfers smaller than L_F, not all the final states can be reached, since some of the final states are Pauli blocked. In the example of the left panel of Fig. 17 the open circles and squares show the collection of states which can result from adding the angular momentum (2, 1) to the Fermi sea (filled circles), filled up to $L_F = 3$. The transfer of angular momentum (2, 1) is prohibited for final occupied states (open circles). The electrons which can participate in the exchange of angular momentum are close to the Fermi level (in fact, those from level $L_F - \ell$ up to L_F).

An example of angular momentum transfers between L_F and $2L_F$ is shown in the middle panel of Fig. 17 for transfers of $(\ell, m) = (4, -3)$. All the electrons in the Fermi sea can participate, but not all final states are unoccupied. Finally, in angular momentum transfers larger than $2L_F$, all the electrons can participate in the scattering and moreover all the resulting final states from the addition of the angular momenta are unoccupied and thus accessible. An example is shown in the right panel of Fig. 17 for transfers of $(\ell, m) = (8, 1)$.

The maximum energy difference between two states (such as those connected by a line in Fig. 17) is

$$\begin{aligned}\omega_{\max} &= \frac{\hbar^2}{2m_{\mathrm{e}}R^2}[(L_F + \ell)(L_F + \ell + 1) - (L_F)(L_F + 1)] \\ &= \frac{\hbar^2}{2m_{\mathrm{e}}R^2}[\ell^2 + \ell(2L_F + 1)].\end{aligned} \tag{147}$$

The smallest energy difference is, for transfers $\ell < 2L_F$

$$\begin{aligned}\omega_{\min} &= \frac{\hbar^2}{2m_{\mathrm{e}}R^2}[(L_F + 1)(L_F + 2) - (L_F)(L_F + 1)] \\ &= \frac{\hbar^2(L_F + 1)}{m_{\mathrm{e}}R^2}.\end{aligned} \tag{148}$$

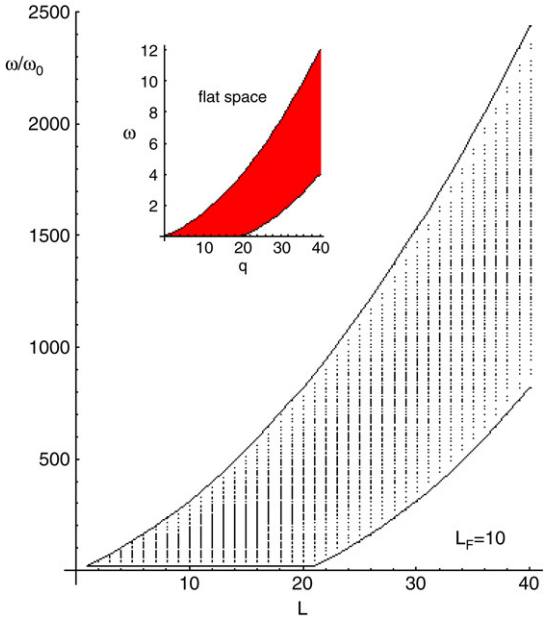

Fig. 18. Structure factor for single-particle excitations; $\omega_0 = \hbar/(m_e R^2)$.

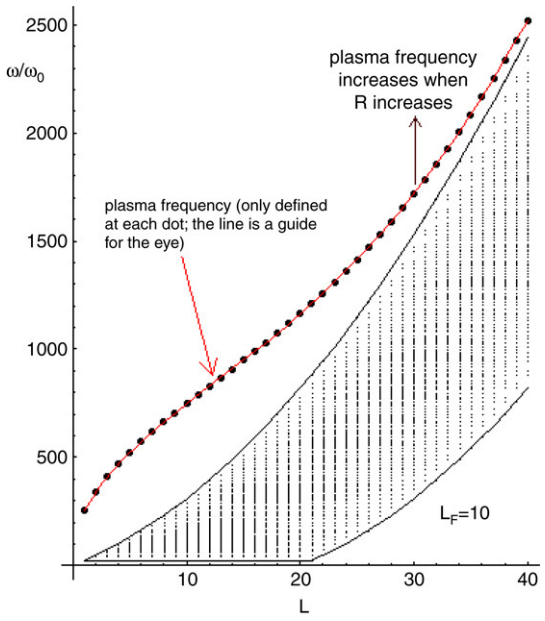

Fig. 19. Regions in the ℓ, ω plane where $S(\ell, \omega) \neq 0$.

The smallest energy difference, for angular momentum transfers with $\ell > 2L_F$ is

$$\omega_{\min} = \frac{\hbar^2}{2m_e R^2}\left[(\ell - L_F)(\ell - L_F + 1) - (L_F)(L_F + 1)\right]$$
$$= \frac{\hbar^2}{2m_e R^2}[\ell^2 - \ell(2L_F - 1) - 2L_F]. \quad (149)$$

In Fig. 18, the possible ℓ, ω combinations are shown for the single-particle excitations, in the case $L_F = 10$ (in the inset, the similar result for the flat electron gas is shown).The minimum and maximum frequencies $\omega_{\min}$ and $\omega_{\max}$ mark off an area in the (ℓ, ω) plane in which single-particle excitations can be created. In the non-curved electron gas these frequencies are $\omega_{\min} = \max(q^2/2 - q, 0)$ and $\omega_{\max} = q^2/2 + q$ as shown in the inset. For any q, ω in the dark area in the inset, a single-particle excitation can be created with this momentum and energy. This area of (q, ω) is commonly referred to as the Landau continuum. In the spherical electron gas, that continuum is discretized. When looking closely, you will see that it consists of a collection of dots. This is a result of the discrete nature of the energy spectrum in the case of the spherical electron gas. It will be averaged out when the temperature is raised $(k_b T \gg \hbar^2/(m_e R^2))$.

3.4.4. Plasmons of the S2DEG

Apart from single-particle excitations in the S2DEG, also collective excitations are possible. Technically speaking "Collective excitations" are defined as poles of the density–density Green's function $\mathcal{D}$, whereas single-particle excitations are defined as poles of the single-particle Green's function G. This means collective excitations appear when $\varepsilon = 0$. In the flat electron gas, these collective excitations are called plasmons. The imparted angular momentum is shared between all the particles.

In a collective mode the entire spherical shell of electrons will oscillate. The frequency of the collective modes (the plasma frequency) will depend on the type of oscillation (ℓ, m). The plasma frequency $\omega_{\rm pl}(\ell, m)$ of the S2DEG can be found by solving the equations

$$1 - \frac{e^2}{2\varepsilon_{\rm vac}\hbar R}\frac{1}{2\ell + 1}\mathrm{Re}\left[\mathcal{D}_{R,0}(\ell, m; \omega)\right] = 0 \quad (150)$$

$$\mathrm{Im}\left[\mathcal{D}_{R,0}(\ell, m; \omega)\right] = 0. \quad (151)$$

The last condition means for the flat electron gas that the plasma branch does not lie in the Landau continuum. In fact, as soon as the plasma branch reaches the Landau continuum, it will be strongly damped. For the spherical electron gas, the Landau continuum is no longer a continuum but a set of points. Does this mean that the S2DEG plasma branch will be much less damped than in the corresponding flat electron gas case? At temperature zero, yes, but as the temperature is raised this is no longer true; the typical temperature $k_B T_{\rm eff} = \hbar^2/(m_e R^2)$ (in the case $L_F = 10$) corresponding to the separation of the points is of the order of 10^{-2}–10^{-3} nK. So for practical purposes, we can continue to consider the region of the single-particle excitations as a continuum.

Fig. 19 shows the plasmon branch (or rather, the value of the plasma frequency $\omega_{\rm pl}(\ell, m)$ for every ℓ. The plasma frequency is the same for every m, it seems only to depend on ℓ. This corresponds to the fact that the plasma frequency of the flat electron gas does not depend on the direction of the wave vector but only on its magnitude. The plasma frequency is shown in units $\hbar/(m_e R^2)$. The spherical decomposition of the Coulomb interaction is given by $U_0/(2\ell + 1)$ so that $U_0 = e^2/(2\varepsilon_{\rm vac}\hbar R)$. In the units of frequency which we use, the dimensionless value of U_0 is $e^2 m_e R/(2\varepsilon_{\rm vac}\hbar^2)$ which is of the order of 10^4.

In Fig. 19 we have used $U_0 = 0.5\ 10^4$. Note that as R increases, U_0 also increases. The calculation shows that for

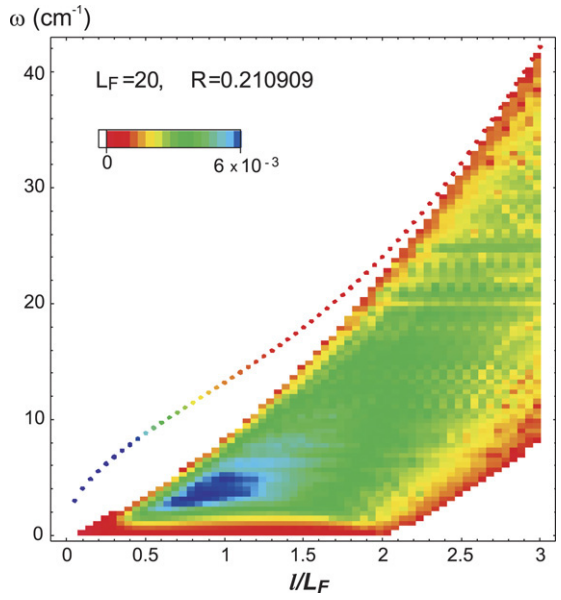

Fig. 20. The RPA dynamic structure factor of the S2DEG is shown color-coded and as a function of the angular momentum l and the energy $\hbar w$. In white regions the RPA dynamic structure factor is zero. In colored regions, the RPA dynamic structure factor differs from zero.

increasing U_0 the plasma frequency also increases. The plasma frequency shows a striking resemblance to the result of a flat 2DEG (the so-called "acoustic plasmons"). Yet it is no longer a continuous branch but rather a set of separate excitations. Another distinction from the 2DEG is that there exists a minimum value larger than zero for the plasmon frequency; the branch starts at a value $\omega_{\rm pl} \neq 0$ which is a characteristic of (optical) plasmons in the three-dimensional electron gas.

To find the spectral weight of the plasmon branch relative to the single-particle excitation band, sum rules can be used. The zeroth moment sum rule for the dynamic structure factor defines the static structure factor: $S(l, m)$:

$$S(l,m) = \int_0^\infty S(l,m;\omega)\mathrm{d}\omega = -\frac{1}{\pi v(l)}\int_0^\infty \mathrm{Im}\left[\frac{1}{\varepsilon(l,m;\omega)}\right]\mathrm{d}\omega. \quad (152)$$

Since the dynamic structure factor only depends on the magnitude of the angular momentum l and not on m, this will also be true for the static structure factor. Fig. 21 shows the static structure factor as a function of angular momentum l. The open squares are the result in the Hartree–Fock approximation [using $\varepsilon_{\rm HF}$, expression (136)], and the full circles are the result in the RPA approximation [using $\varepsilon_{\rm RPA}$, expression (142)]. As in the case of the flat 2DEG, the HF structure factor $S_{\rm HF}(l)$ is linear for small l/L_F, whereas the RPA structure factor approaches zero more rapidly with decreasing l. In the inset of Fig. 21, the first frequency moment of the dynamic structure factor,

$$\langle\omega(l)\rangle = \int_0^\infty \omega S(l,m;\omega)\mathrm{d}\omega, \quad (153)$$

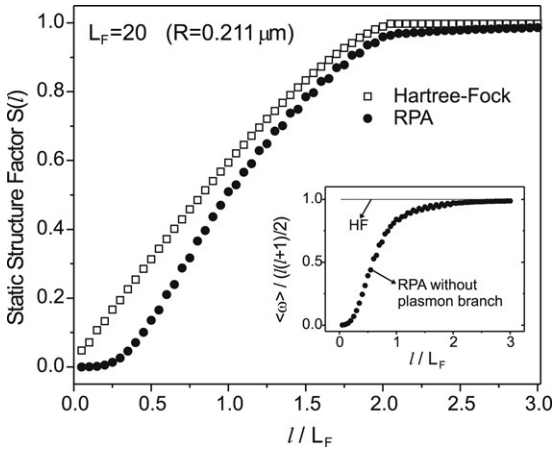

Fig. 21. Static structure factor for the spherical electron gas, in the Hartree–Fock approximation and in RPA.

is shown, again for both HF and RPA approximations. Inaoka [63] derived a sum rule for the first frequency moment of the angular momentum dependent dynamic structure factor. In units $\hbar = m_{\rm e} = R$, this is

$$\langle\omega(l)\rangle = \frac{l(l+1)}{2}. \quad (154)$$

From Fig. 21 it is clear that the HF dynamic structure factor obeys this sum rule. The RPA dynamic structure factor can be written as a sum of a contribution from the plasmon mode and the contribution $S_{\rm cont}$ from single-particle excitations:

$$S_{\rm RPA}(l;\omega) = A(l)\delta[\omega - \omega_{\rm pl}(l)] + S_{\rm cont}(l;\omega), \quad (155)$$

with $A(l)$ the spectral weight of the plasmon branch. The result for $S_{\rm RPA}$ is shown in Fig. 20. The inset of Fig. 21 shows $\int \omega S_{\rm cont}(l,\omega)\mathrm{d}\omega$. From the deficit of the RPA dynamic structure factor without the plasmon mode, shown in the inset of Fig. 21, the spectral weight of the plasmon mode can be derived:

$$A(l)\omega_{\rm pl}(l) = \frac{l(l+1)}{2} - \int_0^\infty \omega S_{\rm cont}(l,\omega)\mathrm{d}\omega. \quad (156)$$

The spectral weight of the single-particle excitation band, relative to the spectral weight of the plasmon mode, is shown in Fig. 22 as a function of L_F, at angular momentum $L/L_F \ll 1$. At small angular momentum ($l/L_F < 0.5$), the plasmon branch carries the most spectral weight, and the region of single-particle excitations only has a small fraction of the total spectral weight. Within the region of single-particle excitations, there is a local maximum in the dynamic structure factor around $l = L_F$.

Inelastic scattering experiments allow determining the dynamic structure factor. In particular the differential cross section for a probe particle of mass M (such as an incident ion) and initial momentum $\mathbf{p}_i$ to be scattered to a final state $\mathbf{p}_f$ with energy transfer between $\hbar\omega$ and $\hbar(\omega + \mathrm{d}\omega)$ to the scattering system is Ref. [64]:

$$\frac{\mathrm{d}\sigma}{\mathrm{d}\theta\mathrm{d}\omega} = \frac{M^2}{8\pi^3}\frac{p_f}{p_i}|V_k|^2 S(k,\omega). \quad (157)$$

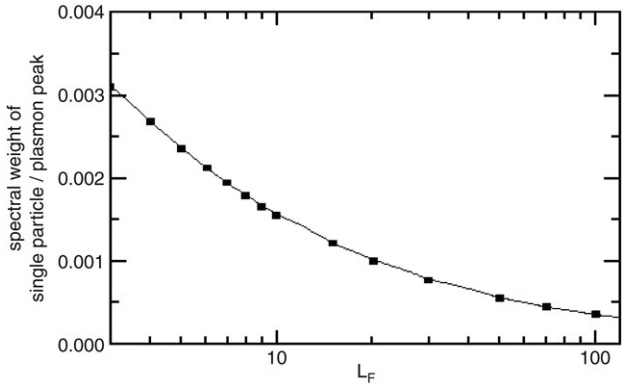

Fig. 22. Ratio of the spectral weight of the Landau continuum to the spectral weight of the plasmon peak.

In this expression, θ is the scattering angle between $\mathbf{p}_f$ and $\mathbf{p}_i$, $|V_\mathbf{k}|$ is the Fourier transform of the interaction potential between the probe particle, and the energy transfer ω is related to the momentum transfer $\mathbf{k}$ by $\hbar\omega = \hbar^2\mathbf{k}.\mathbf{p}_i/m + (\hbar k)^2/(2m)$. The relation between the Fourier decomposition and the spherical decomposition of the density is

$$\widehat{\rho}_\mathrm{e}(\mathbf{k}) = \sum_{j=1}^{N}\langle \mathrm{e}^{\mathrm{i}\mathbf{k}.\hat{\mathbf{r}}_j}\rangle = \sum_{j=1}^{N}\sum_{l}\sqrt{4\pi(2l+1)}i^l j_l(kR)\left\langle Y_{l,0}(\widehat{\theta}_j)\right\rangle = \sum_{l}\sqrt{4\pi(2l+1)}i^l j_l(kR)\widehat{\rho}_\mathrm{e}(l,0) \tag{158}$$

where the z-axis has been taken along the direction of the wave vector $\mathbf{k}$, and $j_l(x)$ is the spherical Bessel function of the first kind, and θ_j is the angle between $\mathbf{k}$ and the position operator of electron j, $\mathbf{r}_j$. The dynamic structure factor is determined by

$$S(k,\omega) = \sum_{l}\left|\sqrt{4\pi(2l+1)}j_l(kR)\right|^2 S(l,0;\omega) \tag{159}$$

which can be derived by writing the dynamic structure factor as a density–density correlation function in the Lehmann representation and substituting expression (158) for $\widehat{\rho}_\mathrm{e}(\mathbf{k})$.

3.5. Magnetic response

The Hamiltonian of a non-interacting S2DEG in a uniform magnetic induction field $\mathbf{B}$ is expressed through the familiar replacement $\mathbf{p} \to \mathbf{p} - q\mathbf{A}$. Here we have a charge $q = -\mathrm{e} = 1.602\,10^{-19}$ C. Using spherical coordinates, the vector potential $\mathbf{A} = A_r\mathbf{e}_r + A_\theta\mathbf{e}_\theta + A_\phi\mathbf{e}_\phi$ for a uniform magnetic induction in the z-direction, $\mathbf{B} = B\mathbf{e}_z$, can be expressed as

$$\begin{pmatrix} A_r \\ A_\theta \\ A_\phi \end{pmatrix} = \begin{pmatrix} 0 \\ 0 \\ \frac{1}{2}Br\sin\theta \end{pmatrix}. \tag{160}$$

We will use this particular gauge for the vector potential in the rest of this work note. Expressing the rotor in spherical coordinates, we can indeed easily see that this vector potential gives rise to the correct magnetic induction:

$$\mathrm{rot}\,\mathbf{A} = \begin{pmatrix} \frac{1}{r\sin\theta}\left\{\frac{\partial\left[\sin(\theta)A_\phi\right]}{\partial\theta} - \frac{\partial A_\theta}{\partial\phi}\right\} \\ \frac{1}{r\sin\theta}\left\{\frac{\partial A_r}{\partial\phi} - \sin\theta\frac{\partial[rA_\phi]}{\partial r}\right\} \\ \frac{1}{r}\left\{\frac{\partial[rA_\theta]}{\partial r} - \frac{\partial A_r}{\partial\theta}\right\} \end{pmatrix} = \begin{pmatrix} B\cos\theta \\ -B\sin\theta \\ 0 \end{pmatrix} = \mathbf{B}, \tag{161}$$

which is the correct answer, since $\mathbf{e}_z = \cos\theta\mathbf{e}_r - \sin\theta\mathbf{e}_\theta$. Similarly, the momentum components can be written in spherical coordinates as $\hat{\mathbf{p}} = \hat{p}_r\mathbf{e}_r + \hat{p}_\theta\mathbf{e}_\theta + \hat{p}_\phi\mathbf{e}_\phi$ where

$$\hat{p}_\phi = \frac{-\mathrm{i}\hbar}{r\sin\theta}\frac{\partial}{\partial\phi}. \tag{162}$$

Note that the z-component of the angular momentum in position representation is written as $L_z = (-\mathrm{i}\hbar)\partial/\partial\phi$, so that from expression (162) we have the equality $\hat{p}_\phi = \hat{L}_z/(r\sin\theta)$. Because the gauge we chose only has a component of the vector potential along $\mathbf{e}_\phi$, the paramagnetic term is given by

$$\frac{\mathrm{e}}{2m_\mathrm{e}}\left(\hat{\mathbf{p}}.A + A.\hat{\mathbf{p}}\right) = \frac{\mathrm{e}Br\sin\theta}{2m_\mathrm{e}}\hat{p}_\phi = \frac{\mathrm{e}B}{2m_\mathrm{e}}\hat{L}_z. \tag{163}$$

The diamagnetic term is given by

$$\frac{\mathrm{e}^2}{2m_\mathrm{e}}A^2 = \frac{(\mathrm{e}Br)^2}{8m_\mathrm{e}}\sin^2\theta. \tag{164}$$

Thus, the Hamiltonian of non-interacting electrons in a magnetic field can be written in the position representation as

$$\hat{H} = -\frac{\hbar^2}{2m_\mathrm{e}}\left(\frac{1}{r}\frac{\partial^2}{\partial^2 r}r\right) + \frac{\hat{L}^2}{2m_\mathrm{e}r^2} + \frac{\mathrm{e}B}{2m_\mathrm{e}}\hat{L}_z + \frac{(\mathrm{e}Br)^2}{8m_\mathrm{e}}\sin^2\theta. \tag{165}$$

Now, we impose that the electrons are on a spherical surface of radius R_b. This corresponds to a wave function of the electron that is factorized in the radial and angular directions where the radial factor is $\delta(r-R_b)$ (alternatively, we could use a Gaussian centered on R_b and with a width given by the thickness of the electron layer — this leads to the same conclusion. We then have for the remaining operator part of the Hamiltonian:

$$\hat{H} = \frac{\hat{L}^2}{2m_\mathrm{e}R_b^2} - \frac{\mathrm{e}B}{2m_\mathrm{e}}\hat{L}_z + \frac{(\mathrm{e}BR_b)^2}{8m_\mathrm{e}}\sin^2\theta. \tag{166}$$

The first term is the kinetic energy of electrons on a sphere. The second represents the paramagnetic effect (the angular momentum part; not the spin part). The third one represents the diamagnetic effect. All units are SI: charge in coulombs, magnetic induction in teslas, angular momentum in Joule × sec. When considering spin effects, an additional Zeeman term appears in the Hamiltonian, corresponding to adding an angular

momentum $2\hbar\hat{S}_z$ to $\hat{L}_z$:

$$\hat{H}^{\text{sphere}} = \frac{\hat{L}^2}{2m_e R_b^2} - \frac{eB}{2m_e}\left(\hat{L}_z + 2\hbar\hat{S}_z\right) + \frac{(eBR_b)^2}{8m_e}\sin^2\theta. \quad (167)$$

Introducing the Larmor frequency $\omega_L = eB/(2m_e)$ allows to write this Hamiltonian as

$$\hat{H}^{\text{sphere}} = \frac{\hat{L}^2}{2m_e R_b^2} - \hbar\omega_L\left(\hat{L}_z/\hbar + 2\hat{S}_z\right) + \frac{1}{2}m_e\omega_L^2 R_b^2\sin^2\theta. \quad (168)$$

3.5.1. From Landau levels to Landau bands

Since the Hamiltonian (168) commutes with $\hat{L}_z$, we factor the eigenfunctions into $\psi(\Omega) = P(\theta)e^{im\phi}$. This allows to rewrite the eigenfunction equation $\hat{H}\psi = E\psi$ as

$$-\frac{\hbar^2}{2m_e R_b^2}\frac{1}{\sin\theta}\frac{\partial}{\partial\theta}\left[\sin\theta\frac{\partial P(\theta)}{\partial\theta}\right] - \frac{eB\hbar}{2m_e}mP(\theta) + \left[\frac{m_e\omega_L^2 R_b^2}{2}\sin^2(\theta) + \frac{\hbar^2 m^2}{2m_e R_b^2\sin^2\theta}\right]P(\theta) = EP(\theta). \quad (169)$$

We express the energy in units $\hbar^2/(2m_e R_b^2)$ and introduce

$$R_L = \sqrt{\frac{\hbar}{m_e\omega_L}} = \sqrt{\frac{2\hbar}{eB}}, \quad (170)$$

the Larmor–cyclotron radius. This is typically $R_L = (36.283/\sqrt{B})$ nm if B is expressed in teslas. We get

$$-\frac{1}{\sin\theta}\frac{\partial}{\partial\theta}\left[\sin\theta\frac{\partial P(\theta)}{\partial\theta}\right] - \frac{2R_b^2}{R_L^2}mP(\theta) + \left[\frac{R_b^4}{R_L^4}\sin^2(\theta) + \frac{m^2}{\sin^2\theta}\right]P(\theta) = \epsilon P(\theta). \quad (171)$$

The only 'system' parameter that appears in this equation is R_b/R_L, the bubble radius divided by the Larmor–cyclotron radius. For even modest fields such as 100 G, $R_L = 363$ nm, so that usually $R_b/R_L > 1$. In fact, we can use this criterion to separate the paramagnetic $(R_b^2/R_L^2) \ll 1$ from the diamagnetic $(R_b^2/R_L^2) \gg 1$ regimes. The paramagnetic effect basically shifts the spherical harmonic energy spectrum by an amount $(R_b^2/R_L^2)m$ for level (l, m). This linear effect becomes negligible in comparison to the diamagnetic shifts $\propto (R_b^2/R_L^2)^2$ when the magnetic field becomes large. The diamagnetic term introduces a "potential" proportional to $\sin^2(\theta)$ that will push the electrons away from the equator and towards the poles of the bubble.

The crucial parameter (R_b^2/R_L^2) can be related to the number of flux quanta piercing the equatorial plane of the bubble. Indeed, the elementary flux quantum for 1 electron is given by $\phi_0 = 2\pi\hbar/e = 4.1357\times10^{-15}$ Wb, and the flux through the equatorial plane of the bubble is given by $\phi = \pi R_b^2 B$. Thus,

$$\Phi = \frac{\phi}{\phi_0} = \frac{\pi R_b^2 B}{2\pi\hbar/e} = \frac{eBR_b^2}{2\hbar} = \frac{R_b^2}{R_L^2}. \quad (172)$$

If less than one flux quantum is piercing the equatorial plane, we're in the paramagnetic regime, if much more than one flux quantum is piercing the equatorial plane, we're in the diamagnetic (Landau) regime.

Switching to $x = \cos\theta$ and $P(\theta) = f(\cos(\theta))$, we find that the differential equation we need to solve is given by

$$(1-x^2)\frac{d^2 f}{dx^2} - 2x\frac{df}{dx} + \left[(\epsilon - \Phi^2 - 2m\Phi) + \Phi^2 x^2 - \frac{m^2}{1-x^2}\right]f = 0. \quad (173)$$

This equation still has singular points, at $x = \pm1$. The regular differential equation associated with (173) can then be found by substituting $f(x) = (1-x^2)^{|m|/2}y(x)$, which yields

$$(1-x^2)y'' - 2x(m+1)y' + [(\epsilon - \Phi^2 - 2m\Phi) - \Phi^2 x^2 - m(m+1)]y = 0. \quad (174)$$

This differential equation was first encountered by Niven [65] in 1880, in connection with a problem involving heat conduction in spheroidal bodies (rugby balls, actually). It has since then been the subject of thorough investigation by mathematicians [70]. It is known as the oblate angular spheroidal equation and it's regular solutions are known as the oblate spheroidal functions of the first kind $S_\ell^{m(1)}(i\Phi, x)$, or the angular spheroidal harmonics. In the limit $\Phi \to 0$ these functions become the associated Legendre functions,

$$\lim_{c\to0} S_\ell^{m(1)}(c, x) = P_\ell^m(x), \quad (175)$$

as they should to obtain the physically relevant solutions. The parameter ℓ runs from $-m$ to m. The angular spheroidal harmonics obey the orthogonality relation

$$\int_{-1}^{1} S_\ell^{m(1)}(c, x)S_{\ell'}^{m(1)}(c, x)dx = \frac{2}{2\ell+1}\frac{(\ell+m)!}{(\ell-m)!}\delta_{\ell,\ell'}. \quad (176)$$

The spheroidal eigenvalues $\lambda_\ell^m(c)$ satisfy

$$\frac{d}{dx}\left[(1-x^2)\frac{dS}{dx}\right] + \left(\lambda_\ell^m(c) + c^2x^2 - \frac{m^2}{1-x^2}\right)S = 0 \quad (177)$$

and thus we find that the energy spectrum and eigenfunctions of electrons on a sphere, in a constant magnetic field, are given by

$$E_{\ell,m}(\Phi) = \frac{\hbar^2}{2m_e R_b^2}[\Phi^2 + 2m\Phi + \lambda_\ell^m(\Phi)], \quad (178)$$

$$\psi_{\ell,m}(\theta, \phi) = S_\ell^{m(1)}(i\Phi, \cos\theta)e^{im\phi}. \quad (179)$$

The single-particle energies are shown in Fig. 23. For weak magnetic fields ($\Phi < 1$) the angular momentum levels are

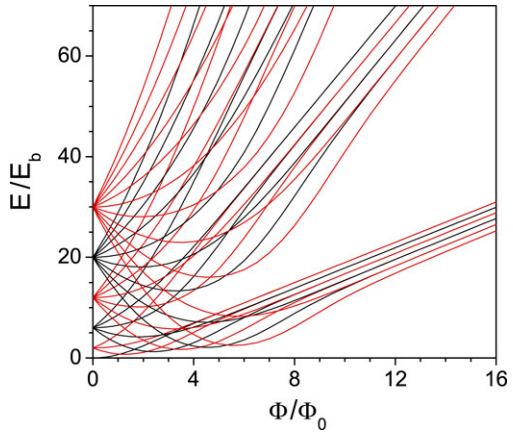

Fig. 23. Energy levels of electrons on a sphere, in a homogeneous and constant magnetic field parallel to the z-axis. The energy, in bubble energy units $\hbar/(2m_e R_b)$, is given as a function of the number of elementary flux quanta h/e piercing the equatorial plane of the bubble.

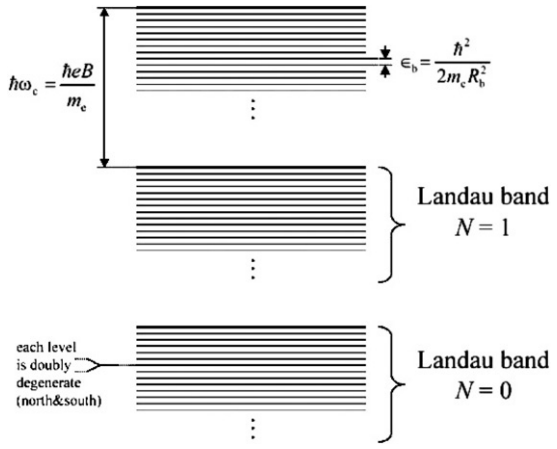

Fig. 24. The electronic energy spectrum of electrons on a spherical surface (with radius R_b) in a strong magnetic field.

Zeeman split. As the magnetic field rises, the levels become grouped in Landau bands rather than Landau levels, as shown in Fig. 24. In a flat 2DEG the Landau levels are highly degenerate, but in the curved S2DEG the Landau levels are only doubly degenerate although they collect in Landau bands [66–68]. The reason for lifting the large degeneracy of the Landau levels is that the magnetic field projection on the normal of the sphere is not the same everywhere on the sphere. On a flat 2DEG there is translational invariance: we can accommodate many electrons performing cyclotron oscillations, as many as the area available divided by the area of the cyclotron orbit. On the sphere, however, this is no longer the case, since moving the cyclotron-orbiting electron along the surface of the sphere causes it to experience a different magnetic field. The remaining degeneracy may be due to the fact that there is a north–south pseudosymmetry to the problem.

As the magnetic field is ramped up, the diamagnetic potential term $\Phi^2 \sin^2\theta$ in Eq. (171) becomes stronger. This term in the potential tends to push the electron wave function out towards the poles of the bubble, while the $m/\sin^2\theta$ term favours the equator. In Fig. 25 for $\Phi = 10$, this results in a depletion at the tempered latitudes. For larger fields, the electron density clumps at latitudes where the orbit corresponds to the cyclotron orbit. Note that the regime of strong magnetic field ($\Phi \gg 1$) is reached for small fields. Already for an $N = 10^4$ bubble at 100 G, $\Phi = 10$. The larger the bubble (or the field) the larger Φ.

Using the preceding results, we can now easily express the Fermi level as a function of the magnetic field by counting the single-electron levels. To find the magnetization of the ground state (assuming a spin polarized electron gas), we list all the occupied levels, sorted by energy, up to the Fermi level, and add up all the m_ℓ quantum numbers of these levels. The result is shown in Fig. 26. Having started with fully filled levels, the magnetization at $B = 0$ is zero. There are roughly four regimes to be distinguished. In the region 1, where the levels are Zeeman split but no level crossings have occurred yet, the magnetization stays zero. Next, there is a region (indicated by '2' in Fig. 1) where the Fermi energy stays roughly constant. This is a region where many level crossings appear as the different ℓ states start trading places in the ordered energy level diagram. Then a transition (region 3) to the regime of Landau bands (region 4) takes place; at the point indicated by the arrow, the system has settled down in the Landau band structure. The magnetization will decrease linearly, as more and more levels with large m_ℓ are added to the lowest Landau band. Steps can be seen, as more and more levels enter the Landau band; the period of these steps corresponds roughly to the magnetic field increase to have one extra elementary flux through the equatorial plane of the bubble.

3.5.2. *Surface magnetoplasmons*

To find how the plasmons are affected by the magnetic field, we return to the RPA result

$$\varepsilon_{\mathrm{RPA}}(\ell, m; \omega) = 1 - \frac{e^2}{2\varepsilon_{\mathrm{vac}}\hbar R}\frac{1}{2\ell+1}\mathcal{D}_{R,0}(\ell, m; \omega) \qquad (180)$$

where the retarded density–density Green's function is given by expression (134) as a function of the occupation numbers and the single-particle energies $E_{lm} = l(l+1)/2$. In a weak non-zero magnetic field in the z-direction an m-dependent term will appear, coming from the orbital moment.

$$E_{lm} = \frac{l(l+1)}{2} - \mu_{\mathrm{B}} m B$$

where μ_{B} is a Bohr magneton. Plasma frequencies are found as zeros of real part of ε in the region where imaginary part of ε is also zero, i.e. solving

$$1 - \frac{e^2}{2\varepsilon\hbar R}\frac{1}{2l+1}\mathrm{Re}[D_{R,0}(l, m, \omega_{\mathrm{pl}})] = 0$$

for the region where $\mathrm{Im}[D_{R,0}] = 0$. The exact calculation of the sums over occupied orbitals is computable only for relatively small total number of electrons.

By doing the calculation for $L_F = 10$ we get different plasma branches for different m shown by different colors in Fig. 27. This figure shows the location of the plasma branches (for each m, in rainbow colors) as a result of an exact summation over the occupied single-particle states for

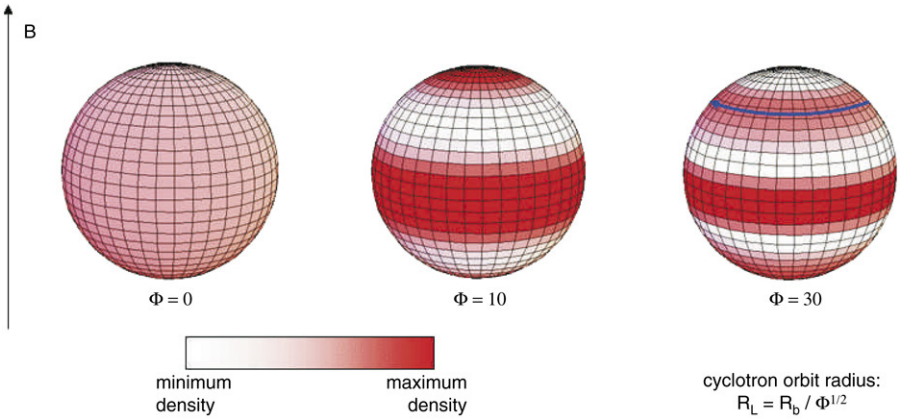

Fig. 25. The density distribution of electrons on the sphere is shown as a the magnetic field is ramped up. For weak fields, electrons are pushed away from the tempered latitudes towards the poles and the equator. For stronger fields, the electron density forms bands with radii corresponding to the cyclotron radii.

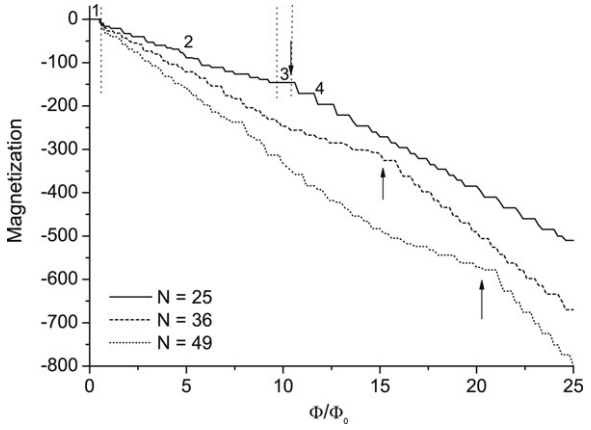

Fig. 26. Total magnetization of the multielectron bubble, as a function of the number of elementary flux quanta through the equatorial plane.

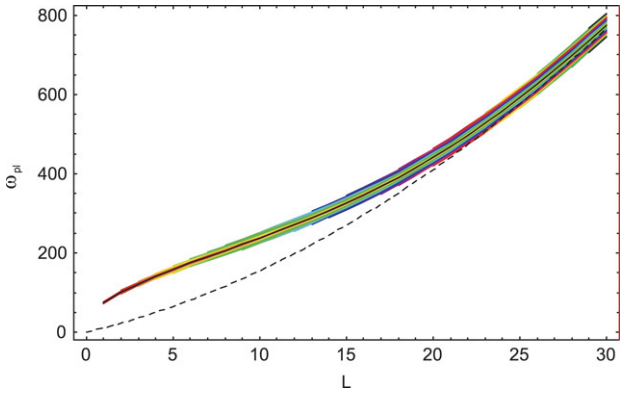

Fig. 27. "Band" of plasma frequencies for a sphere containing 10 electrons in magnetic field calculated from a microscopic model. Plasma frequencies for different quantum numbers m are shown by different colors. Even though the frequency is defined only at integer l, the line is drawn continuous for better visibility. The dashed line marks the region of continuum states.

a sphere with $L_F = 10$, where the spin degree of freedom has not been taken into account. The $m = 0$ line, in black, corresponds to the location of the (degenerate) plasma branch at zero magnetic field. The dotted line shows the edge of the continuum region, so that above this line $\mathrm{Im}[D_{R,0}] = 0$. The effect of the magnetic field is to lift the degeneracy, and

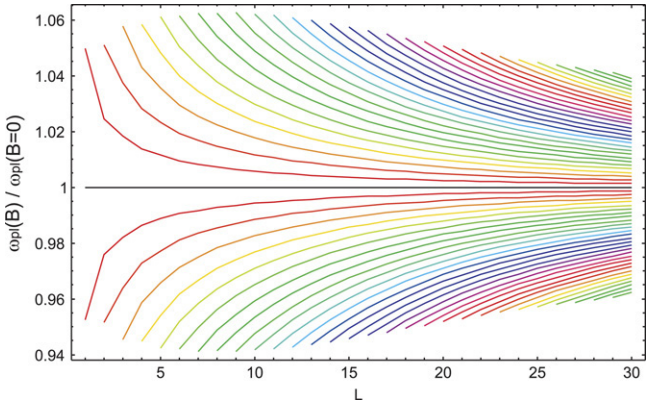

Fig. 28. Enlarged view of the m-dependent plasma frequencies from Fig. 27. All frequencies are normalized to the $m = 0$ plasma line. The lines are drawn as joined points for better visibility.

broaden the plasma branch [69]. This is to be contrasted with the behavior of bulk metals in a (weak) magnetic field; in the case of the nanoscopic spherical system, the coupling with the orbital momentum rapidly leads to a broad plasmon branch – Fig. 27 corresponds to about 0.13 T.

It is interesting to note that while the plasma branch for $m = 0$ always stays above the continuum states (depicted by dashed line), some of the $m < 0$ branches enter into the continuum at $l \gtrsim 20$, which will cause their damping. For better visibility of the structure of this "plasma band", Fig. 28 shows the ratio of the $m = 0$ plasma branch that is identical to the plasma frequency without magnetic field and other possible m's at certain values of l. In this plot, the lifting of the degeneracy (that itself increases as l is increased) is more clearly visible. We can qualitatively observe that with increasing quantum number l, the number of branches is increasing (for every l there are $2l + 1$ branches), but the distance between them is decreasing, keeping the overall width of the "plasma band" approximately constant. We verified that the width of the band is proportional to the magnetic field over a range of three orders of magnitude. If the system contains large numbers of electrons so that the frequency cannot be calculated exactly in this microscopic way, we can apply a phenomenological model, using the observation from the above case. Instead of having one resonant frequency

for the sphere given as

$$\omega_0(l) = \sqrt{\frac{Ne^2}{\sqrt{4\pi} m_e R^3 \epsilon_1} \frac{l(l+1)}{2l+1}}$$

it is possible to introduce phenomenologically a whole (quasicontinuous) "band" of m-dependent magnetoplasmons

$$\omega_B(l,m) = \omega_0(l)\left(1 + \Delta_{pl}\frac{m}{l}\right)$$

where Δ_{pl} is a constant and denotes the width of the "plasma band".

4. Surface polaron effects

4.1. Introduction

The two-dimensional (2D) electron system formed on the surface of liquid helium has been widely investigated, especially with regard to the formation and melting of a Wigner lattice [71]. An electric field pressing the electrons against the helium surface results in an interaction between the electrons and the quantized oscillation modes of the helium surface, the ripplons [72]. The electron–ripplon interaction can lead to the formation of a quasiparticle–ripplonic polaron (see, e.g., [56,73–76]), or "ripplopolaron". Mobility measurements on electrons near a liquid helium surface [77] have been interpreted in terms of ripplonic polarons [74].

Due to the acoustic nature of the ripplon dispersion at long wavelengths, the electron–ripplon coupling can be relatively strong, and self-trapping can be realized. In Ref. [56], the system of two-dimensional electrons on a film of liquid helium was studied as a polaron problem, and treated with the all-coupling Feynman approach. It was found that with increasing coupling constant the effective mass of a ripplopolaron undergoes a first-order transition from the bare electron mass to several helium atom masses, i.e., a localization transition occurs. Self-trapped ripplonic polarons "melt" at relatively low temperatures (≈17 mK for a 100 Å helium film) [73]. However, a switch to a polaron localized state for a two-dimensional electron system above a thin helium film was observed experimentally [78] for considerably higher temperatures $T \sim 1$ K. According to the theory of single ripplonic polarons [73], the polaron binding energy is far too low to allow for the polaron formation at the experimental temperatures of Ref. [78]. The presence of many electrons introduces a new energy scale — the Coulomb interaction energy, which for the experiment of Ref. [78] is about 10 K. It was supposed in Ref. [78] that the polaron formation in a many-electron system above the helium surface is facilitated with respect to the polaron formation for a single electron. The results of Ref. [78] indicate the importance of many-body effects for ripplonic polaron phenomena.

A characteristic of the electron–ripplon and electron–electron interactions is the appearance of collective oscillations of the electron–ripplon system. Early experimental evidence for a 2D Wigner crystallization of electrons on a liquid He surface [8] relied on the detection of the coupled plasmon–ripplon modes [79]. The energy spectrum of the coupled electron–ripplon system in a 2D electron crystal near the helium surface was studied theoretically (see, e. g., [80–82]) and experimentally [83–85]. The non-linear transport of an electron Wigner solid along a helium surface finds an explanation in terms of the electron–ripplon interaction [86].

In multielectron bubbles, because of the relatively high values of the electric field induced by the electrons and due to the high electron densities, the ripplonic polaron effects are expected to play a more significant role than in an electron system near a flat helium surface. This has stimulated our investigations of the vibrational modes and of the ripplonic polaron states in MEBs [17,87–90]. The Wigner lattice of ripplopolarons was analyzed in Refs. [88,90]. To study the ripplopolaron Wigner lattice at finite temperature and for arbitrary values of the electron–ripplon coupling, in Ref. [88] the all-coupling variational Feynman path integral approach [91] is applied. As discussed in Ref. [92], in the case of the melting of a Wigner lattice on a helium surface, the additional coupling of electrons to the helium degrees of freedom gives rise to interesting physics. The system of interacting electrons in a MEB can exist in different phases: (i) the electron gas, (ii) the electron liquid, (iii) the electron solid (the Wigner lattice) and possibly (iv) a superconducting phase [93]. The Wigner lattice is a sufficiently "rigid" structure, which may strongly resist a deformation. In this view, the approximation of an ideally conducting surface [17] is well-founded only for the two first phases, but it seems to be hardly applicable when the electron layer in a MEB is a Wigner crystal. Consequently, in order to describe oscillation modes of a MEB, the electron and ripplon motions must be considered together. In Ref. [87] the approach of Ref. [17] was extended to take into account the redistribution of charge along the bubble surface when the bubble deforms. The dynamical modes of a MEB were described [87] taking into account the interplay between the motion of the helium surface (ripplons) and the vibrations of the electron subsystem (plasmons). That treatment beyond the approximation of an ideally conducting surface results in the mixed electron–ripplon oscillations of a MEB. This allows us to derive the dispersion relation for the spherical plasmon modes and the plasmon–ripplon coupling peculiar for the spherical surface.

As mentioned in Ref. [94], there exists a similarity between the Wigner crystals of ripplonic polarons and Wigner crystals of large polarons in 3D and 2D. Although the electron–ripplon interaction is different from the Fröhlich interaction, the resonances in the optrical absorption spectrum observed by Grimes and Adams [8] are explained at low density [79] by analogous qualitative arguments as those developed in Ref. [94] for 3D and for 2D Fröhlich polarons. Also some properties of the liquid phase in polar doped semiconductors arise due to the mixing of plasmons and LO phonons [94].

Below, we represent the key properties of the electron–ripplon interaction and of ripplonic polarons in multielectron bubbles. Those properties will be used, in particular, for the analysis of the superconductivity in MEBs in Chapter 5.

4.2. Ripplons on the bubble surface

4.2.1. Dispersion relation on a sphere

The surface of a bubble in liquid helium can be described by a function $R(\Omega)$ which gives the distance of the helium surface from the center of the bubble, in a direction given by the spherical angle $\Omega = \{\theta, \phi\}$. In equilibrium (at zero pressure), the multielectron bubble has a spherical surface with radius R_b. We expand the deformation away from the spherical surface in spherical harmonics:

$$R(\Omega) = R_b + \sum_{\ell=1}^{\infty} \sum_{m=-\ell}^{\ell} Q_{\ell m} Y_{\ell m}(\Omega) \tag{181}$$

where R_b is the angle-averaged radius of the bubble, $Q_{\ell m}$ is the amplitude of the spherical harmonic deformation mode indexed by $\{\ell, m\}$, and $Y_{\ell m}(\Omega)$ is the corresponding spherical harmonic. These modes of deformation are referred to as ripplons in analogy with the surface modes of a flat surface of liquid helium. In Ref. [17] the dispersion relation for the ripplons in a multielectron bubble has been studied as a function of pressure and related to the bubble stability. In Ref. [87], the results of [17] are extended in order to take the coupling and mixing of the ripplons and the electronic modes into account.

In a multielectron bubble, the electrons are confined to a thin (1 nm) layer at the inner surface of the bubble. This layer is anchored to the surface of the bubble, so that when the surface deforms, the layer conforms to the new bubble surface. The electrons can redistribute themselves inside the spherical layer, so that the surface density of electrons is no longer uniform. We describe the surface density with the function $n_S(\Omega)$ giving the number of electrons in a solid angle $\mathrm{d}\Omega$ around Ω:

$$n_S(\Omega) = \frac{N}{4\pi R_b^2} + \sum_{\ell=1}^{\infty} \sum_{m=-\ell}^{\ell} n_{\ell m} Y_{\ell m}(\Omega). \tag{182}$$

This function is normalized such that $N = \int n_S(\Omega) R_b^2 \mathrm{d}\Omega$ is the total number of electrons in the bubble or on the droplet. The $n_{\ell m}$'s represent the amplitudes of charge redistributions corresponding to spherical harmonics $Y_{\ell m}$.

The total potential energy of the multielectron bubble or droplet can be separated into several contributions: (i) a term from the surface tension energy $U_S = \sigma S$, with $\sigma \approx 3.6 \times 10^{-4}$ J/m^2 and S the surface of the deformed bubble or droplet; (ii) a pressure related term $U_p = pV$, with p the difference in pressure outside and inside the bubble and V the volume of the bubble; (iii) a term representing the electrostatic energy U_C of the electron layer. In this last term, the quantum corrections (such as the exchange contribution) to the electrostatic energy can be neglected [15]. The first two terms, U_S and U_p, have been derived in [17]:

$$U_S = 4\pi\sigma R_b^2 + \frac{\sigma}{2} \sum_{\ell=1}^{\infty} \sum_{m=-\ell}^{\ell} (\ell^2 + \ell + 2) \left| Q_{\ell m} \right|^2, \tag{183}$$

$$U_p = \frac{4\pi}{3} p R_b^3 + p R_b \sum_{\ell=1}^{\infty} \sum_{m=-\ell}^{\ell} |Q_{\ell m}|^2 \tag{184}$$

whereas U_S is an exact expression, U_p is an expansion up to second order in $Q_{\ell m}$ and the third-order term has been neglected. In what follows, we assume small amplitude deformations and small amplitude charge redistributions such that

$$\sqrt{\ell(\ell+1)}\, |Q_{\ell m}| \ll R_b, \tag{185}$$

$$\sqrt{\ell(\ell+1)}\, |n_{\ell m}| \ll \frac{N}{4\pi R_b^2}. \tag{186}$$

The electrostatic potential $V(r)$ of the deformed MEB with a non-uniform surface electron density is calculated straightforwardly within the framework of the Maxwell equations by expanding the potential inside and outside the deformed bubble in their respective spherical decompositions and imposing the electrostatic boundary conditions at the surface. The potential energy associated with this electrostatic potential is given by

$$U_C = -(1/2) \int n_S(\Omega) V(R, \Omega) \mathrm{d}\Omega. \tag{187}$$

If we keep only terms up to second order in both $n_{\ell m}$ and $Q_{\ell m}$, we find

$$\begin{aligned} U_C = {} & \frac{\mathrm{e}^2 N^2}{2\varepsilon R_b} + 2\pi \mathrm{e}^2 R_b^3 \sum_{\ell=1}^{\infty} \sum_{m=-\ell}^{\ell} \frac{|n_{\ell m}|^2}{\varepsilon_1 \ell + \varepsilon_2 (\ell+1)} \\ & - \frac{\mathrm{e}^2 N^2}{8\pi\varepsilon R_b^3} \sum_{\ell=1}^{\infty} \sum_{m=-\ell}^{\ell} \frac{\varepsilon_1 \ell^2 - \varepsilon_2 (\ell+1)}{\varepsilon_1 \ell + \varepsilon_2 (\ell+1)} |Q_{\ell m}|^2 \\ & - \mathrm{e}^2 N \sum_{\ell=1}^{\infty} \sum_{m=-\ell}^{\ell} \frac{\ell+1}{\varepsilon_1 \ell + \varepsilon_2 (\ell+1)} n_{\ell m} Q_{\ell m}^*. \end{aligned} \tag{188}$$

where e is the electron charge, ε_1 is the dielectric constant of the medium inside the surface, and ε_2 is the dielectric constant of the medium outside the surface. For a multielectron bubble, $\varepsilon_2 = \varepsilon$ with $\varepsilon = 1.0572$ the dielectric constant of liquid helium, and $\varepsilon_1 = 1$ (if the temperature of the helium is low enough, the bubble has vacuum inside).

The ripplon contribution to the kinetic energy of the MEB is associated with the motion of the liquid helium surface. Following a derivation of Lord Rayleigh for oscillating liquid droplets [52], we find

$$T_r = \frac{\rho R_b^3}{2} \dot{R}_b^2 + \frac{\rho R_b^3}{2} \sum_{\ell=1}^{\infty} \sum_{m=-\ell}^{\ell} \frac{1}{\ell+1} \left| \dot{Q}_{\ell m} \right|^2. \tag{189}$$

where $\rho \approx 145$ kg/m^3 is the density of liquid helium. Note that for a bubble, $\ell + 1$ appears in the denominator instead of ℓ for the droplet in Lord Rayleigh's treatment.

The 'classical' kinetic energy of the electrons is given by

$$T_{\mathrm{e}} = \frac{m_{\mathrm{e}}}{2} \sum_{j=1}^{N} \dot{\mathbf{w}}^2(\mathbf{r}_j) \tag{190}$$

with m_{e} the electron mass, and $w(r_j)$ represents the displacement of electron j out of its equilibrium position r_j.

Since we assumed (186), we can use the formula

$$T_{\rm e} = \frac{N m_{\rm e}}{8\pi} \int_{\rm surface} \dot{\mathbf{w}}^2(\mathbf{r}) {\rm d}^2\mathbf{r} \tag{191}$$

and express the field of displacements $w(r)$ as a sum of a longitudinal field $w_L(r)$ and transverse field $w_{\rm T}(r)$. We investigate the effect of the longitudinal field, which can be written as a gradient of a scalar potential. The (divergence free) transverse field is not considered here since it does not couple to the ripplons. Using the relation

$$\nabla \cdot \mathbf{w}_L(\mathbf{r}) = 1 - \frac{4\pi R_b^2}{N} n_S(\theta, \phi) \tag{192}$$

we can express the kinetic energy of the electrons as

$$T_{\rm e} = \frac{1}{2} \sum_{\ell=1}^{\infty} \sum_{m=-\ell}^{\ell} \frac{4\pi m_{\rm e} R_b^6}{N\ell(\ell+1)} |\dot{n}_{\ell m}|^2 . \tag{193}$$

It is easy to check that the present approach yields, for the 3D and the 2D electron gas, the known expressions for the plasma frequencies.

The full Lagrangian of the bubble, including the ripplon modes and charge redistribution modes, is given by substituting expressions (189), (193), (183), (184) and (188) in $L = T_r + T_{\rm e} - U_S - U_p - U_C$. The result can be brought in the following form

$$\mathcal{L} = \mathcal{L}_R + \sum_{\ell,m} \frac{M_\ell}{2} \left(\dot{Q}_{\ell m}^2 - \omega_r^2(\ell) Q_{\ell m}^2 \right) + \sum_{\ell,m} \frac{m_\ell}{2} \left(\dot{n}_{\ell m}^2 - \omega_p^2(\ell) n_{\ell m}^2 \right) + \sum_{\ell,m} \gamma_\ell n_{\ell m} Q_{\ell m}. \tag{194}$$

The first term in expression (194) contains the Lagrangian describing the radial motion (the anharmonic breathing mode):

$$\mathcal{L}_R = \frac{\rho R_b^3}{2} \dot{R}_b^2 - \frac{4\pi}{3} p R_b^3 - 4\pi\sigma R_b^2 - \frac{N^2 {\rm e}^2}{2\varepsilon R_b}. \tag{195}$$

In what follows we assume that $\dot{R}_b = 0$ and the bubble radius is given by its equilibrium value.

4.2.1.1. Ripplon modes. The Lagrangian L also contains a part representing the harmonic oscillation of the ripplon modes, with oscillator mass term

$$M_\ell = \frac{\rho R_b^3}{\ell + 1}, \tag{196}$$

and the bare ripplon frequency:

$$\omega_r(\ell) = \sqrt{\frac{1}{M_\ell} \left[\sigma(\ell^2 + \ell + 1) + p R_b - \frac{N^2 {\rm e}^2}{4\pi\varepsilon R_b^3} \frac{\ell^2 - \varepsilon(\ell+1)}{\ell + \varepsilon(\ell+1)} \right]}. \tag{197}$$

The bare ripplon frequencies and their dependence on the pressure were the subject of [17]. In the limit of very large bubbles, $R_b \to \infty$, the dispersion relation for ripplons on a flat helium surface [95] is recovered: if the momentum k is identified with ℓ/R_b, then the typical $k^{3/2}$ is retrieved. When R_b is set equal to the equilibrium Coulomb radius, the modes $\ell = 1, 2$ obtain a zero frequency in agreement with the result of Salomaa and Williams [14]. For typical multielectron bubbles with radii in the range of 1–100 μm (and numbers of electrons of the order 10^4–10^7) the ripplon frequencies for $\ell < 1000$ lie typically in the MHz–GHz range.

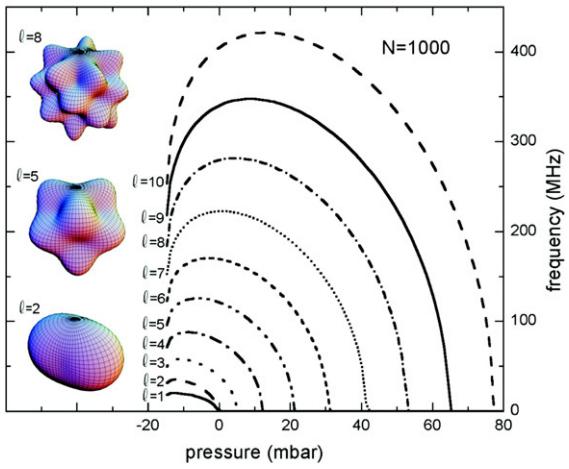

Fig. 29. The frequency of ripplon modes $\ell = 1, \ldots, 10$ is shown as a function of external applied pressure (not vapor pressure) for $N = 1000$. The leftmost points of the graphs start at the critical underpressure: for a pressure more negative than this value, the bubble is unstable against isotropic expansion. As the pressure is increased, more and more modes obtain a vanishing frequency. On the left the deformations (exaggerated) are shown for a few of the modes. (From Ref. [17].)

In [17], it was shown that small negative pressures can stabilize a bubble against dynamic instability, while positive pressures can drive all ripplon modes unstable (see Fig. 29). Since both negative and positive pressures are easily achievable experimentally, it will be interesting if bubbles can be created in a "stable" configuration that can be visually observed to study these predictions.

4.2.1.2. Longitudinal plasmon modes. Next, the Lagrangian (194) contains a part representing the (small amplitude) harmonic oscillation of the classical charge redistribution around its equilibrium. The oscillator mass term for these oscillations is

$$m_\ell = \frac{4\pi m_{\rm e} R_b^6}{N\ell(\ell+1)}, \tag{198}$$

and the corresponding frequencies are given by

$$\omega_p(\ell) = \sqrt{\frac{N{\rm e}^2}{m_{\rm e} R_b^3} \frac{\ell(\ell+1)}{\ell + \varepsilon(\ell+1)}}. \tag{199}$$

In the limit of large bubbles, this frequency corresponds to that of the longitudinal plasmon frequency of a 2D electron system on the helium surface [96]. If the electrons form a Wigner lattice, this is the longitudinal phonon frequency. If the momentum k is identified with ℓ/R_b, then the typical $k^{1/2}$ dispersion for this longitudinal plasmon is retrieved. Based

on this correspondence, we will refer to these modes in a multielectron bubble as the '(longitudinal) plasmon modes of the MEB' (or 'longitudinal phonon modes of the MEB' if the electrons form a Wigner lattice).

For typical multielectron bubbles with radii in the range of 1–100 μm (and numbers of electrons of the order 10^4–10^7) the longitudinal plasmon frequencies for $\ell < 1000$ lie typically in the GHz–THz range. For bubbles with $N > 10^5$, the longitudinal plasmon frequencies are larger than the ripplon frequencies, $\omega_p(\ell) \gg \omega_r(\ell)$.

The equations of motion for the electron charge redistribution on a deformed bubble are given by:

$$\frac{\mathrm{d}}{\mathrm{d}t}\frac{\partial \mathcal{L}}{\partial \dot{n}_{\ell m}} = \frac{\partial \mathcal{L}}{\partial n_{\ell m}} \Leftrightarrow m_\ell \ddot{n}_{\ell m} = -m_\ell \omega_p^2(\ell) n_{\ell m} + \gamma_\ell Q_{\ell m}. \quad (200)$$

When $\omega_p(\ell) \gg \omega_r(\ell)$ the electrons can redistribute much faster on the surface of the bubble than the bubble surface can deform. Thus, we can make an adiabatic approximation to find the charge redistribution of the electrons on a bubble with a given deformation. We find from (200) that if the bubble surface deformation is described by a given set of spherical deformation amplitudes $Q_{\ell m}$, the equilibrium charge distribution on the deformed bubble must satisfy the relation

$$\frac{n_{\ell m}}{n_0} = \frac{(\ell+1)}{2}\frac{Q_{\ell m}}{R_b}, \quad (201)$$

with $n_0 = N/(4\pi R_b^2)$.

4.2.2. Ripplon–plasmon mixing

The last term in the Lagrangian (194) represents the coupling between the longitudinal plasmons and the ripplons, with coupling strength given by

$$\gamma_\ell = N\mathrm{e}^2 \frac{(\ell+1)}{\ell + \varepsilon(\ell+1)}. \quad (202)$$

For electrons on a flat helium surface, such a coupling between ripplons and longitudinal plasmons/phonons was derived by Fisher et al. [79] and detected experimentally [8]. For electrons on the inner surface of a deformed bubble, we find a similar coupling, but only ripplon and longitudinal plasmon modes which have the same angular momentum couple to each other. After the diagonalization of the ripplon–plasmon part of the Lagrangian (194), we arrive at the eigenfrequencies,

$$\Omega_{1,2}(\ell) = \sqrt{\frac{1}{2}\left[\omega_p^2(\ell) + \omega_r^2(\ell)\right] \pm \frac{1}{2}\sqrt{\left[\omega_p^2(\ell) - \omega_r^2(\ell)\right]^2 + 4\gamma_\ell^2}}. \quad (203)$$

In Fig. 30, we show the eigenfrequencies $\Omega_1(\ell)$ and $\Omega_2(\ell)$ for $N = 10^5$ as a function of ℓ and p. The frequency $\Omega_2(\ell)$ is close to the ripplon frequency derived for an MEB within the approximation of a conducting surface [17]. Consequently, this frequency can be attributed to the ripplon modes, renormalized due to the ripplon–plasmon mixing. The other branch of oscillations with the frequencies $\Omega_2(\ell)$ can be related to the longitudinal plasmon mode admixed with a small component of ripplon nature. In typical multielectron bubbles, the difference in frequency between the ripplon and the plasmon modes weakens the coupling between these modes. Note that the multielectron bubble will be stable when both Ω_1^2 and Ω_2^2 are positive. This condition is equivalent to

$$\omega_p^2(\ell)\omega_r^2(\ell) > \gamma_\ell. \quad (204)$$

By substituting the (199), (197) and (202) in the inequality (204) it can easily be seen that when the radius of the bubble is equal to the equilibrium radius, the ripplon–plasmon mixing does not change the criterion of stability for a MEB formulated in Ref. [17].

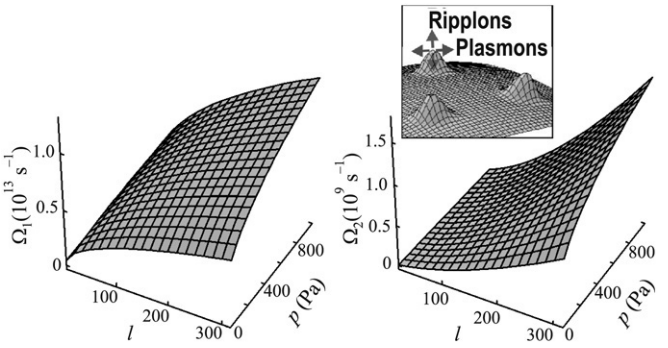

Fig. 30. Vibrational eigenfrequencies of an MEB in liquid helium, $\Omega_1(l)$ (phonon modes) and $\Omega_2(l)$ (renormalized ripplon modes) given by Eq. (203) for $N = 10^5$ as a function of l and of p. Inset: a schematic picture of the directions of motion for phonons and ripplons in an MEB. The ripplons are excitations of the helium surface (with typical frequencies in the MHz–GHz range), while the phonons are related to the motion of electrons (with typical frequencies in the THz regime) tangential to the bubble surface. Note the different scales for Ω_1 and Ω_2. (From Ref. [87].)

4.3. Electron–ripplon interaction

In Ref. [88], the effects of the electron–ripplon coupling in a multielectron bubble in liquid helium are investigated, and the differences with the case of electrons on a flat helium surface are highlighted. The interaction energy between the ripplons and the electrons in the multielectron bubble is derived from the following considerations: (i) the distance between the layer electrons and the helium surface is fixed (the electrons find themselves confined to an effectively 2D surface anchored to the helium surface) and (ii) the electrons are subjected to a force field, arising from the electric field of the other electrons. It occurs that the enhanced electron–ripplon coupling in the bubble leads to a new solid phase, a lattice of ripplonic polarons, that is distinct from the electron Wigner lattice.

4.3.1. The ripplonic subsystem

The ripplon gas (without the breathing mode) is described by the Hamiltonian

$$\hat{H}^{(\mathrm{rip})} = \sum_{\ell>0,m} \hbar\omega_\ell \hat{a}_{\ell,m}^+ \hat{a}_{\ell,m}. \quad (205)$$

The bare ripplonic frequencies are

$$\omega_\ell = \sqrt{\frac{\sigma}{\rho R^3}(\ell+1)(\ell^2+\ell+2) + \frac{p}{\rho R^2}2(\ell+1)}. \tag{206}$$

Two regimes exist: a surface tension dominated regime with $pR/\sigma < 1$ and a pressure dominated regime with $pR/\sigma > 1$.

Regime parameter pR/σ

	10^4	10^6	10^8
0 mbar	0	0	0
100 mbar	14.734	151.74	1522.0
3 bar	194.61	1951.1	19516

. (207)

The first line is clearly surface tension dominated, and the second and third lines are pressure dominated (until $\ell^2+\ell+2$ equals pR/σ). We keep the density at 145 kg/m^3. In the surface tension dominated regime, $\omega_\ell \approx \omega_\sigma \ell^{3/2}$ with

Frequency unit $\omega_\sigma = \sqrt{\sigma/(\rho R^3)}$ in MHz (=7.6382 μK)

	10^4	10^6	10^8
0 mbar	1.4391	0.014354	1.4349×10^{-4}
100 mbar	4.1585	0.12582	0.0039609
3 bar	14.235	0.44841	0.014175

. (208)

In the pressure dominated regime, $\omega_\ell = \omega_p \ell^{1/2}$ with

Frequency unit $\omega_p = \sqrt{2p/(\rho R^2)}$ in MHz (=7.6382 μK)

	10^4	10^6	10^8
0 mbar	0	0	0
100 mbar	22.574	2.1920	0.21853
3 bar	280.84	28.012	2.8004

. (209)

Finally, two tables that shows which mode has enough energy to change the angular momentum of an electron at the Fermi level, and at which mode the dispersion crosses over from p-dominated to σ-dominated:

ℓ such that $\hbar\omega_\ell = \epsilon_0(L_F+1)$

	10^4	10^6	10^8
0 mbar	295	490	817
100 mbar	372	794	1708
3 bar	490	1053	2263

ℓ such that $\sigma(\ell^2+\ell+2) = 2pR$

	10^4	10^6	10^8
0 mbar	0	0	0
100 mbar	5	17	55
3 bar	20	62	197

. (210)

We define the ripplon Green's function in analogy to the conventional phonon Green's function:

$$D(\ell,m;t) = -\mathrm{i}\left\langle \mathcal{T}[\hat{A}_{\ell,m}(t)\hat{A}^+_{\ell,m}(0)]\right\rangle$$

with $\hat{A}_{\ell,m} = \hat{a}_{\ell,m} + \hat{a}^+_{\ell,-m}$.

We have introduced the auxiliary creation and annihilation functions $\hat{A}_{\ell,m}$. The electron–ripplon interaction can be written as

$$\hat{H}_{\mathrm{int}} = \sum_{j,n} M_j \hat{A}_{jn} \sum_{\ell,m} \hat{c}^+_{(\ell,m)\otimes(j,n)}\hat{c}_{\ell,m}, \tag{211}$$

where M_ℓ is the electron–ripplon interaction amplitude. In the original ripplon operators, the unperturbed ripplon Green's function is

$$\begin{aligned} D^{(0)}(\ell,m;t) = &-\mathrm{i}\langle\mathcal{T}[(\hat{a}_{\ell,m}\mathrm{e}^{-\mathrm{i}\omega_\ell t} + \hat{a}^+_{\ell,-m}\mathrm{e}^{\mathrm{i}\omega_\ell t}) \\ &\times(\hat{a}^+_{\ell,m} + \hat{a}_{\ell,-m})]\rangle\theta(t>0) \\ &-\langle\mathcal{T}[(\hat{a}_{\ell,-m} + \hat{a}^+_{\ell,m}) \\ &\times(\hat{a}^+_{\ell,-m}\mathrm{e}^{\mathrm{i}\omega_\ell t} + \hat{a}_{\ell,m}\mathrm{e}^{-\mathrm{i}\omega_\ell t})]\rangle\theta(t<0). \end{aligned}$$

Here unperturbed means that the presence of and the interaction with the electrons is not taken into account. The only expectation value different from zero are $\langle\hat{a}_{\ell,m}\hat{a}^+_{\ell,m}\rangle = n_{\ell m}+1$ and $\langle\hat{a}^+_{\ell,m}\hat{a}_{\ell,m}\rangle = n_{\ell m}$ where the ripplon occupation number is $n_{\ell m} = 1/(\exp\{\hbar\omega_\ell/k_\mathrm{B}T\}-1)$. At zero temperature, all $n_{\ell m}=0$ and so

$$D^{(0)}(\ell,m;t) = -\mathrm{i}[\theta(t>0)\mathrm{e}^{-\mathrm{i}\omega_\ell t} + \theta(t<0)\mathrm{e}^{\mathrm{i}\omega_\ell t}].$$

Its temporal Fourier transform is defined by

$$\begin{aligned} D^{(0)}(\ell,m;\omega) &= \int_{-\infty}^{+\infty}\mathrm{e}^{\mathrm{i}\omega t}D^{(0)}(\ell,m;t)\mathrm{d}t \\ &= \frac{1}{\omega-\omega_\ell+\mathrm{i}\eta} - \frac{1}{\omega+\omega_\ell-\mathrm{i}\eta}, \end{aligned}$$

which simplifies to

$$D^{(0)}_{\mathrm{rip}}(\ell,m;\omega) = \frac{2\omega_\ell}{\omega^2-\omega_\ell^2+\mathrm{i}\eta}, \tag{212}$$

with again η an infinitesimal.

In Table 1, for typical multielectron bubbles, the values of the several physical quantities are given at zero applied external pressure. The number of electrons in the bubble (N), the bubble radius (R_b), the average interelectron distance (d), the surface density of electrons (n_s), the pressing field generated by the electrons $|E|$, the characteristic energy scale of the electron–ripplon interaction $[(\mathrm{e}|E|)^2/\sigma$, cf. formula (234)], and the characteristic frequency of the lattice potential (ω_{lat}) are given. Compare these quantities to, for example, the maximum density ($\approx 2\times10^9$ cm^{-2}) and the maximum pressing field ($\approx$3 kV/cm) achievable on a flat helium surface over bulk. We can see that, using pressure, the surface of the MEB can be compressed to achieve 2D electron densities as high as 10^{14} cm^{-2} [17], whereas flat surfaces are limited to 2×10^9 cm^{-2} due to an instability [11]. This instability is not present in multielectron bubbles [38], although the bubbles may be unstable to bifurcation under pressure, as discussed in Chapter 2. As a result very large electric fields exist on an electron, normal to the surface (due to all other electrons in the MEB), whereas for a flat surface the maximum field is around 3 kV/cm.

Table 1
Parameters of multielectron bubbles

N	R_b (μm)	d (nm)	n_s (cm^{-2})
10^3	0.228	25.57	1.529×10^{11}
10^5	4.937	55.34	3.265×10^{10}
10^7	106.4	119.3	7.025×10^{9}
N	$\|\mathbf{E}\|$ (kV/cm)	$e^2\|\mathbf{E}\|^2/\sigma$ (meV)	$\omega_{\rm lat}$ (THz)
10^3	138.3	85.16	3.891
10^5	63.80	3.884	1.222
10^7	6.350	0.180	0.386

From Ref. [88].

The Hamiltonian of a single electron on a flat helium surface is given by

$$\hat{H} = \frac{\hat{p}^2}{2m_e} + \sum_q \omega(q)\hat{a}^+_{\mathbf{q}}\hat{a}_{\mathbf{q}} + \sum_q M_q e^{-i\mathbf{q}.\mathbf{r}}\left(\hat{a}_{\mathbf{q}} + \hat{a}^+_{-\mathbf{q}}\right), \quad (213)$$

where $\hat{p}$ is the electron momentum operator, m_e is the electron mass, and $\omega(q) = q\sqrt{\sigma q/\rho}$ is the ripplon dispersion relation with $\sigma \approx 3.6\times10^{-4}$ J/m^2 the surface tension of helium and $\rho = 145$ kg/m^3 the mass density of helium. In this Hamiltonian, we restrict ourselves to 2D position and momentum operators, assuming that the part of the wave function of the electrons relating to the direction perpendicular to the surface can be factored out exactly. The second-quantization operators $\hat{a}^+_{\mathbf{q}}, \hat{a}_{\mathbf{q}}$ create/annihilate a ripplon with planar wave number q. The electron–ripplon coupling amplitude is given by

$$M_q = \sqrt{\frac{\hbar q}{2\rho\omega(q)}}e|\mathbf{E}|, \quad (214)$$

where E is the electric field perpendicular to the surface (the so-called 'pressing field'), and e is the electron charge. The pressing field pushes the electrons with a force eE towards the helium surface, that acts like a sheet with surface tension σ. Note that there is a 1 eV barrier preventing single electrons from penetrating the helium surface. The self-induced trapping potential of the electron on the helium surface is manifested by the appearance of a dimple in the helium surface underneath the electron, much like the deformation of a rubber sheet when a person is pulled down on it by a gravitational force. The resulting quasiparticle consists of the electron together with its dimple and can be called a ripplonic polaron or ripplopolaron [97].

Hamiltonian (213) for the ripplopolarons is very similar to the Fröhlich Hamiltonian describing polarons [98]; the role of the phonons is now played by the ripplons. Methods suitable for the study of single polarons have been used to analyze the single ripplopolaron on a flat surface [73, 99]. Recently, Fratini and Quémerais [100] have proposed a path integral treatment for a Wigner lattice of polarons. In their treatment of the electron Wigner lattice embedded in a polarizable medium such as a semiconductors or an ionic solid, Fratini and Quémerais [100] described the effect of the electrons on a particular electron through a mean-field lattice

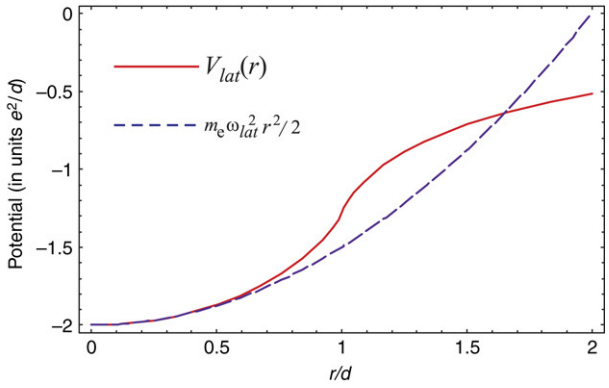

Fig. 31. The mean-field potential for an electron in a MEB $V_{\rm lat}(r)$ (the solid curve) and its quadratic approximation, Eq. (216) (the dashed curve) in units of e^2/d.

potential. The (classical) lattice potential $V_{\rm lat}$ is obtained by approximating all the electrons acting on one particular electron by a homogeneous charge density in which a hole is punched out; this hole is centered in the lattice point of the particular electron under investigation and has a radius given by the lattice distance d. Thus, in their approach, the anisotropy effects are neglected. A second assumption implicit in this approach is that the effects of exchange are neglected. This can be justified by noting that for the electrons to form a Wigner lattice it is required that their wave function be localized to within a fraction of the lattice parameter as follows from the Lindemann melting criterion [101,102]. As can be read from Table 1, the typical distance between electrons (the lattice parameter) is 10–100 nm.

Within the particular mean-field approximation, the lattice potential can be calculated from classical electrostatics and we find that for a 2D electron gas it can be expressed in terms of the elliptic functions of first and second kind, $E(x)$ and $K(x)$,

$$V_{\rm lat}(\mathbf{r}) = -\frac{2e^2}{\pi d^2}\left\{|d-r|\,E\left[-\frac{4rd}{(d-r)^2}\right] + (d+r)\,\mathrm{sgn}(d-r)\,K\left[-\frac{4rd}{(d-r)^2}\right]\right\}. \quad (215)$$

Here, $\mathbf{r}$ is the position vector of an electron measured from the lattice position. We can expand this potential around the origin to find the small amplitude oscillation frequency of the electron lattice:

$$\lim_{r\ll d} V_{\rm lat}(\mathbf{r}) = -\frac{2e^2}{d} + \frac{1}{2}m_e\omega_{\rm lat}^2 r^2 + \mathcal{O}\left(r^4\right), \quad (216)$$

with the confinement frequency

$$\omega_{\rm lat} = \sqrt{\frac{e^2}{m_e d^3}}. \quad (217)$$

The potential $V_{\rm lat}(\mathbf{r})$is shown in Fig. 31.

Although that mean-field approach may seem crude, it has the distinct advantage that the 'phonon' frequency $\omega_{\rm lat}$ of the electron lattice corresponds closely to the longitudinal plasmon frequency that can be derived using an entirely different

approach based on a more rigorous study of the modes of oscillations of both the bubble and the charge distribution on the bubble surface. This frequency lies typically in the THz range and the lattice parameter d in MEBs ranges roughly from 10 to 100 nm. From this, and from the successful application of this mean-field approach to polaron crystals in solids, we conclude that the approach based on that of Fratini and Quémerais describes the influence of the other electrons well in the framework of small amplitude oscillations of the electrons around their lattice point. The (modified) Lindemann melting criterion [88] suggests that the lattice will melt when the electrons are on average displaced more than ca. 10% from their lattice position; thus in the regime of interest the Fratini–Quémerais approach is applicable. In the mean-field approximation, the Hamiltonian for a ripplopolaron in a lattice on a locally flat helium surface is given by

$$\hat{H} = \frac{\hat{p}^2}{2m_e} + V_{\text{lat}}\left(\hat{\mathbf{r}}\right) + \sum_{\mathbf{q}} \hbar\omega(q)\hat{a}^+_{\mathbf{q}}\hat{a}_{\mathbf{q}} + \sum_{\mathbf{q}} M_q e^{-i\mathbf{q}.\mathbf{r}}\left(\hat{a}_{\mathbf{q}} + \hat{a}^+_{-\mathbf{q}}\right), \tag{218}$$

where $\hat{r}$ is the electron position operator.

Now that the lattice potential has been introduced, we can move on and include effects of the bubble geometry. If we restrict our treatment to the case of large bubbles (with $N > 10^5$ electrons) such as those already experimentally observed [5], then both the ripplopolaron radius and the interelectron distance d are much smaller than the radius of the bubble R_b. This gives us ground to use the locally flat approximation using the auxiliary model of a ripplonic polaron in a planar system described by (218), but with a modified ripplon dispersion relation and an modified pressing field.

The interaction energy between the ripplons and the electrons in the multielectron bubble can be derived from the following considerations: (i) the distance between the layer electrons and the helium surface is fixed (the electrons find themselves confined to an effectively 2D surface anchored to the helium surface [14]) and (ii) the electrons are subjected to a force field, arising from the electric field of the other electrons.

The interaction term in the Hamiltonian taking into account the bubble geometry is

$$\hat{H}_{\text{int}} = \sum_{\ell,m}\sum_{j,n} M_\ell \hat{A}_\ell \hat{c}^+_{(j,n)\otimes(\ell,m)}\hat{c}_{(j,n)}, \tag{219}$$

where $\sum_{j,n}\hat{c}^+_{(j,n)\otimes(\ell,m)}\hat{c}_{(j,n)}$ is the (ℓ, m) spherical component of the electron density, and $\hat{A}_\ell$ is a sum of ripplon creation and annihilation operators defined in the previous subsection. The coupling factor M_ℓ arises from two effects. It can be calculated as an effect of the radial electric field generated by the electrons and pressing the electrons against the helium surface, or it can be derived as the change in polarization energy of the electron–helium system when the helium surface is deformed and the electrons are at rest. Both mechanisms will play a role, and need to be compared in magnitude. First, we examine the polarization energy (as done in flat space by Cole [54]). The resulting factor is

$$M_\ell = c_\ell \frac{n\alpha e^2}{2R^3}\sqrt{\frac{\hbar(\ell+1/2)}{2\rho R\omega_\ell}}, \tag{220}$$

where the polarizability is $\alpha = \frac{m}{4\pi\rho}\frac{\varepsilon-1}{\varepsilon+1}$ with m is the mass of a helium atom and $\varepsilon = 1.0572$ is the dielectric constant of helium. n is the mass density so that $na = 2.2126343 \times 10^{-3}$. The factor c_ℓ is a geometrical factor, given by

$$c_\ell = 2\pi\int_{-1}^{1}\frac{P_\ell(\mu)}{(1+x^2-2x\mu)^2}\mathrm{d}\mu \quad \text{with } x = 1 - \frac{d}{R}.$$

In the limit of a flat surface this should go to the following value to give a correspondence with Cole's results [54],

$$M_{\mathbf{q}} = \pi\frac{n\alpha e^2\lambda^2}{4}A^{-1/2}\sqrt{\frac{\hbar q}{2\rho_{\text{He}}\omega_{\mathbf{q}}}}$$

since

$$c_\ell \to \frac{9\sqrt{\pi}}{4(d/R)^2}.$$

To study the electron–ripplon coupling, we introduce a coupling constant given by

$$g^{(p)} = \frac{9\sqrt{\pi}}{8}\frac{n\alpha e^2}{d^2R}\sqrt{\frac{\hbar}{2\rho R\omega_\sigma}}$$

$$\Rightarrow M_\ell = g^{(p)}\frac{(\ell+1/2)^{1/2}}{[(\ell+1)(\ell^2+\ell+2+2pR/\sigma)]^{1/4}}. \tag{221}$$

Here $g^{(p)}$ itself has units of energy. It is very sensitive to d and to small changes in ε. At large ℓ we have $M_\ell \approx g^{(p)}\ell^{-1/4}$.

Electron–ripplon coupling constant $g^{(p)}$ in mK

	10^4	10^6	10^8
0 mbar	16.280	0.77571	0.038648
100 mbar	57.029	9.6077	1.6990
3 bar	257.19	45.424	8.0723

. (222)

These values for $g^{(p)}$ are relatively large compared to the ripplon energy scale, denoting a very strong electron–ripplon coupling.

An electrical field, perpendicular to the helium surface and acting on the electrons will also give rise to a coupling between the electrons and surface deformations. If the surface deforms and the electrons conform to the surface, the energy associated with a displacement u of an electron in an electrical field E is eEu. The electrical field in the case of a bubble is not an externally applied field but is generated by the electrons themselves:

$$\mathbf{E} = -\frac{eN}{R^2}\mathbf{e}_{\mathbf{r}}.$$

Values of this field under various conditions are given in the table below:

Electric field at the bubble surface, in kV/cm

	10^4	10^6	10^8
0 mbar	127.61	27.397	5.9000
100 mbar	525.19	495.17	492.17
3 bar	2709.4	2695.5	2694.1

. (223)

In experiments with electrons on helium films, an external applied electric field has been used to enhance the electron–ripplon coupling. The electric fields produced in these experiments are of the order of 10–100 kV/cm [103]. It is clear that, using pressure to compress the bubbles, we can achieve higher coupling in bubbles. The electron–ripplon coupling constant due to the electric field is given by [56]

$$g^{(e)} = \frac{1}{2\sqrt{\pi}} \frac{-eE}{R} \sqrt{\frac{\hbar}{2\rho R\omega_\sigma}}, \tag{224}$$

where the factor $\sqrt{4\pi R^2}$ corresponds to the square root of the surface, $\sqrt{A}$ in the flat-surface equivalent.

Electron–ripplon coupling constant $g^{(e)}$ in mK

	10^4	10^6	10^8
0 mbar	19.179	0.41123	0.0088538
100 mbar	134.18	22.006	3.8807
3 bar	1280.7	226.13	40.184

. (225)

These values are comparable to the values of the polarization induced interaction. Low pressure and large electron numbers make the polarization interaction the dominant effect, whereas raising the pressure or lowering the number of electrons increase the effect of the electric field induced interaction. The total electron–ripplon interaction is then given by

$$M_\ell = [g^{(p)} + g^{(e)}] \frac{(\ell + 1/2)^{1/2}}{[(\ell+1)(\ell^2 + \ell + 2 + 2pR/\sigma)]^{1/4}}, \tag{226}$$

with

Total electron–ripplon coupling constant $g = g^{(p)} + g^{(e)}$ in mK

	10^4	10^6	10^8
0 mbar	35.459	1.1869	0.047502
100 mbar	191.21	31.613	5.5797
3 bar	1537.9	271.56	48.257

. (227)

As mentioned before, these numbers are large compared to the ripplon energies. Both the electric field and the helium polarization contribute on a similar order of magnitude to the total electron–ripplon coupling.

Note that the electric field in the bubble is larger than the typical pressing fields (of the order of 10^2–10^3 V/cm) applied on electrons on a flat helium surface. Thus, the electron–ripplon coupling will be stronger in the multielectron bubble. The modified ripplon dispersion relation (and the dependence of the bubble radius on the number of electrons and the pressure) was studied in more detail in Ref. [17], and the stability of the multielectron bubble against surface deformation modes was investigated in detail in Refs. [14,38]. These studies concluded that even though a large effective electric pressing field is present at zero pressure, the bubbles can be stable in contrast to the flat surface which can only sustain a moderate electric pressing field.

The crucial differences that exist between the case of a ripplopolaron in the multielectron bubble and on the flat surface (and that are preserved in the locally flat approximation) are (i) the electric pressing field E is stronger than that typically realized for electrons on helium films (see Table 1) and thus the electron–ripplon coupling is enhanced as compared to the normal film; (ii) the interaction energy arising from the change in polarization of the helium due to the displacement of the electron has a similar form, but is much weaker and can be neglected. In addition the electric field, and thus the electron–ripplon coupling increases as the bubble radius is decreased. Thus, pressurizing the bubbles, which decreases the radius, also increases the electron–ripplon coupling strength (roughly as R_b^{-2}). In the high pressure regime ($p \gg \sigma/R_b$), the bubble radius goes as $p^{-1/4}$ and thus the electron–ripplon coupling increases as $\sqrt{p}$. The pressure provides a 'tuning knob' to set the electron–ripplon interaction strength at a desired level. There is uncertainty concerning the stability of pressurized bubbles against bifurcation and this calls for experimental study. However, small bubbles can have large electron–ripplon couplings.

4.4. Ripplonic polarons

As follows from the aforesaid treatment, two different forces act on the electron to localize it in a multielectron bubble. Firstly, there is the Coulomb lattice potential from the electrons at neighboring lattice sites. This potential was described in a mean-field classical approach by Fratini and Quémerais [100]. Near the lattice site ($r = 0$) the Coulomb lattice potential is quadratic with a characteristic frequency $\omega_{\text{lat}} = \sqrt{e^2/(m_e d^3)}$ on the order of THz, consistent with our results for the phonon frequencies.

The second force that acts on the electron and tends to localize it, is caused by the electron–ripplon interaction. Due to the coupling with the ripplons, the electron generates a self-induced trapping potential [73] and forms a "ripplopolaron", similar to Fröhlich's polaron formed by an electron in a bath of longitudinal optical phonons. This can be understood intuitively as follows. The static electric field of the multielectron bubble, acting on the electron at the surface, is $E = e_{\mathbf{r}} Ne/(2\varepsilon R_b^2)$ where $e_{\mathbf{r}}$ is the unit vector in the radial direction. This field pushes the electrons with a force eE towards the helium surface, that acts like a sheet with surface tension σ. Note that there is a 1 eV barrier preventing the electrons from penetrating the helium surface. The self-induced trapping potential of the electron on the helium surface is manifested by the appearance of a dimple in the helium surface underneath the electron, much like the deformation of a rubber sheet when a person is pulled down on it by a gravitational force. The ripplopolaron is the quasiparticle consisting of the electron together with its dimple.

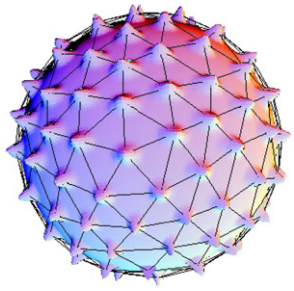

Fig. 32. Ripplopolaron Wigner crystal in a MEB (schematic picture). The ripplons and the Coulomb lattice potential give rise to a ripplopolaron Wigner crystal. The electrons are localized in the dimples.

Ripplopolarons are well described by the Feynman path integral variational method [91] which is successful in determining the properties of polarons in ionic and polar crystals. Extensions of this theory exist both for the description of polaron lattices [100] and for ripplopolarons on a flat surface [73]. These theories represent the system of electrons and ripplons by a variational model system consisting of an electron coupled to a fictitious mass through a spring. The center of mass of the ripplopolaron is well approximated by the center of mass of the model system, R_C. The distance ρ between the fictitious mass and the electron is a measure for the extent of the ripplopolaron wave function.

Given the two localizing potentials (the Coulomb lattice potential and the ripplopolaron self-trapping potential), four phases can be construed.

(i) A ripplopolaron Wigner crystal: In this phase the electrons are localized on lattice sites, and the electron–ripplon interaction is strong enough to create, underneath each electron, a dimple which is also localized within the lattice parameter (see Fig. 32).
(ii) A ripplopolaron liquid: This occurs if the electrons are delocalized and form a liquid, but the electron–ripplon interaction is still strong enough to form a dimple underneath the electron, and the electrons move with a velocity small enough so that the dimple can follow the electron.
(iii) An electron liquid: In this phase the electrons are not localized, and have a kinetic energy corresponding to velocities too large to have a dimple following them (they "outrun their dimple").
(iv) An electron solid (electron Wigner crystal): this occurs if the electrons are localized by the Coulomb lattice potential, but the electron–ripplon interaction is too weak to create a dimple (or creates a dimple wider than the distance between two neighboring electrons).

4.4.1. Strong coupling results

4.4.1.1. Ground state. To gain insight into the nature of the Wigner solid of ripplopolarons, we will analyze Hamiltonian (218) first in the strong coupling approach. In the next subsection, the more general and more accurate Feynman variational path integral method will be applied, generalizing the results of this subsection to finite temperature. Noting that the frequency associated with the electron's motion, $\omega_{\rm lat}$, is typically several orders of magnitude larger than the frequency associated with the ripplons [87], $\omega(q)$, we can safely make the product ansatz for the wave function of the ripplopolaron in the lattice: $|\Psi\rangle = |\psi_{\rm e}\rangle\,|\phi\rangle$. Here $|\phi\rangle$ is the factor of the wave function that contains the ripplon coordinates, and $|\psi_{\rm e}\rangle$ is the electronic part of the wave function. For small amplitude oscillations of the electrons around their lattice site, the lattice potential $V_{\rm lat}$ is well approximated by a parabolic potential (216), so we choose a Gaussian trial wave function for the electronic part:

$$|\psi_{\rm e}\rangle = \frac{1}{\pi^{1/2}a}{\rm e}^{-r^2/(2a^2)}. \tag{228}$$

In this trial wave function, the variational parameter is a, the width of the electron wave function. Taking the expectation value of Hamiltonian (218) with respect to this electronic part of the wave function yields:

$$\begin{aligned}\langle\psi_{\rm e}|\hat{H}|\psi_{\rm e}\rangle = {}& \frac{\hbar^2}{2m_{\rm e}a^2} + \frac{m_{\rm e}\omega_{\rm lat}^2}{2}a^2 + \sum_{\mathbf{q}}\hbar\omega(q)\hat{a}_{\mathbf{q}}^{+}\hat{a}_{\mathbf{q}} \\ & + \sum_{\mathbf{q}} M_q {\rm e}^{-a^2q^2/4}\left(\hat{a}_{\mathbf{q}} + \hat{a}_{-\mathbf{q}}^{+}\right).\end{aligned} \tag{229}$$

The ripplonic part of $\langle\psi_{\rm e}|\hat{H}|\psi_{\rm e}\rangle$ represents a displaced harmonic oscillator and can be rewritten as

$$\begin{aligned}\langle\psi_{\rm e}|\hat{H}|\psi_{\rm e}\rangle = {}& \frac{\hbar^2}{2m_{\rm e}a^2} + \frac{m_{\rm e}\omega_{\rm lat}^2}{2}a^2 - \sum_{\mathbf{q}}\frac{|M_q|^2{\rm e}^{-a^2q^2/2}}{\hbar\omega(q)} \\ & + \sum_{\mathbf{q}}\hbar\omega(q)\left[\hat{a}_{\mathbf{q}}^{+} + \frac{M_q{\rm e}^{-a^2q^2/4}}{\hbar\omega(q)}\right] \\ & \times\left[\hat{a}_{\mathbf{q}} + \frac{M_q{\rm e}^{-a^2q^2/4}}{\hbar\omega(q)}\right].\end{aligned} \tag{230}$$

The ground state of the displaced (2D) harmonic oscillator at temperature zero has energy $\hbar\omega(q)$, independent of the variational parameter a. To find the variational optimal value of a, we minimize the ripplopolaron energy

$$E(a) = \frac{\hbar^2}{2m_{\rm e}a^2} + \frac{m_{\rm e}\omega_{\rm lat}^2}{2}a^2 - \sum_{\mathbf{q}}\frac{|M_q|^2{\rm e}^{-a^2q^2/2}}{\hbar\omega(q)}. \tag{231}$$

The sum over momenta can be rewritten as an integral, remembering

$$\sum_{\mathbf{q}} \to \int_{q>1/R_b}\frac{{\rm d}^2\mathbf{q}}{(2\pi)^2} = \int_{\tilde{q}>1}\frac{{\rm d}^2\tilde{\mathbf{q}}}{(2\pi)^2R_b^2}. \tag{232}$$

The lower limit appears since the largest wavelength available is $1/R_b$. We checked that the final results do not depend crucially on the value of this naturally occurring cut-off. A dimensionless integration variable $\tilde{q} = qR_b$ is introduced. The ground state energy of the ripplopolaron can then be evaluated analytically:

$$E(a) = \frac{\hbar^2}{2m_{\rm e}a^2} + \frac{m_{\rm e}\omega_{\rm lat}^2}{2}a^2$$

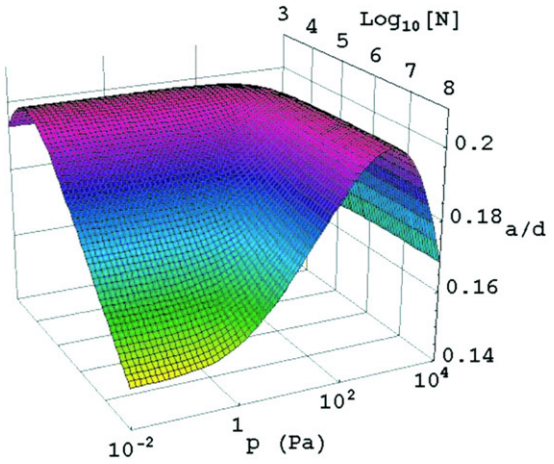

Fig. 33. The variational parameter a describing the width of the electron wave function in the strong coupling approach as a function of number of electrons and pressure in the multielectron bubble. d is the interelectron separation. (From Ref. [88].)

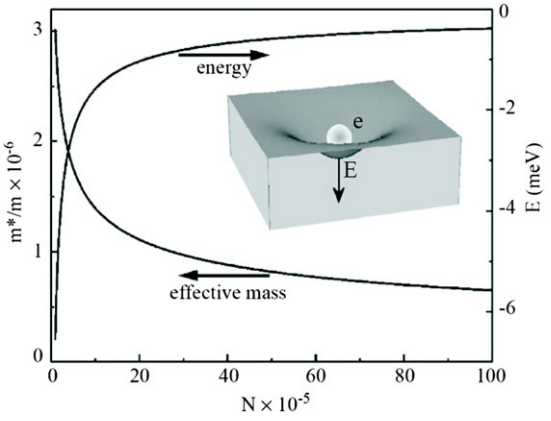

Fig. 34. Energy and effective mass of the ripplonic polaron at zero temperature and zero pressure, as a function of the number of electrons in the bubble. (From Ref. [89].)

$$-\frac{(\mathrm{e}|\mathbf{E}|)^2}{2\pi\sigma}\int_1^\infty \mathrm{d}\tilde{q}\,\frac{\tilde{q}}{\tilde{q}^2+\frac{pR_b}{\sigma}}\exp\left[-\frac{a^2}{2R_b^2}\tilde{q}^2\right] \tag{233}$$

$$=\frac{\hbar^2}{2m_\mathrm{e}a^2}+\frac{m_\mathrm{e}\omega_\mathrm{lat}^2}{2}a^2-\frac{(\mathrm{e}|\mathbf{E}|)^2}{4\pi\sigma}\exp\left[\frac{pa^2}{2\sigma R_b}\right]\Gamma\times\left[0,\frac{a^2}{2R_b^2}\left(1+\frac{pR_b}{\sigma}\right)\right], \tag{234}$$

where Γ is the incomplete gamma function. Fig. 33 shows the result for the variational parameter a as a function of number of electrons and pressure in the multielectron bubble. If this figure, a is expressed relative to the interelectron distance $\sqrt{4\pi R_b^2/N}$.

The self-induced trapping energy of the electron in its dimple, and the ripplopolaron effective mass are shown in Fig. 34 as a function of N.

4.4.1.2. Dimple shape. The ripplonic part of the Hamiltonian (230) represents oscillations of the helium surface no longer around the original bubble surface, but around a new, displaced equilibrium surface. This displacement of the helium surface is the dimpling. Underneath each electron, a dimple appears. The new equilibrium surface, described by the function $u(r)$ (cf. Eq. (181)), can be found by using the canonical relation between the surface displacement operator and the ripplon creation and annihilation operators:

$$\hat{Q}_\mathbf{q}=\sqrt{\frac{\hbar q}{2\rho\omega(q)}}(\hat{a}_\mathbf{q}+\hat{a}^+_{-\mathbf{q}}), \tag{235}$$

and evaluating

$$u(\mathbf{r})=\sum_\mathbf{q}\left\langle\Psi\left|\hat{Q}_\mathbf{q}\right|\Psi\right\rangle\mathrm{e}^{\mathrm{i}\mathbf{q}.\mathbf{r}}. \tag{236}$$

The result is given by

$$u(\mathbf{r})=\frac{\mathrm{e}|\mathbf{E}|}{2\pi\sigma}\int_1^\infty \mathrm{d}\tilde{q}\,\frac{\tilde{q}}{\tilde{q}^2+\frac{pR_b}{\sigma}}J_0\left(\frac{\tilde{q}r}{R_b}\right)\mathrm{e}^{-a^2\tilde{q}^2/(4R_b^2)}. \tag{237}$$

In the limiting case of a large bubble, this result corresponds to that of Shikin and Monarkha [97] for electrons on a flat helium surface; the role of the capillary constant is played by $p/(\sigma R_b)$. Fig. 35 shows, for a bubble with $N=10^5$ electrons, at different pressures the shape of the dimpled surface. Several dimples are shown — above the center of each dimple an electron is present. The dotted curve represents the non-dimpled $u(r)=0$ surface; the curvature of the bubble surface is visible in this curve. The electrons are separated by the interelectron distance $d=\sqrt{4\pi R_b^2/N}$. As the pressure increases, the radius of the bubble decreases. Since the number of electrons is fixed the electric pressing field increases, making on its turn the electron–ripplon coupling larger. This results in deeper, narrower dimples. Note that while the deformation here can be several angstroms, for a flat surface on bulk helium the maximum deformation of a dimple is less than one angstrom citeIkeziPRB25. Also for electrons on a thin helium film above a dielectric substrate, the dimple depth can reach several angstroms [74].

4.4.2. Path integral treatment

The simple but intuitive approach of the previous subsection describes the system in the limit of temperature zero. To study the ripplopolaron Wigner lattice at finite temperature (and for any value of the electron–ripplon coupling), we use the variational path integral approach [91]. This variational principle distinguishes itself from Rayleigh–Ritz variation in that it uses a trial action functional S_trial instead of a trial wave function.

The action functional of the system described by Hamiltonian (218), becomes, after elimination of the ripplon degrees of freedom,

$$S=-\frac{1}{\hbar}\int_0^{\hbar\beta}\mathrm{d}\tau\left\{\frac{m_\mathrm{e}}{2}\dot{r}^2(\tau)+V_\mathrm{lat}[r(\tau)]\right\}+\sum_\mathbf{q}|M_q|^2\times\int_0^{\hbar\beta}\mathrm{d}\tau\int_0^{\hbar\beta}\mathrm{d}\sigma\,G_{\omega(q)}(\tau-\sigma)\mathrm{e}^{\mathrm{i}\mathbf{q}\cdot[\mathbf{r}(\tau)-\mathbf{r}(\sigma)]}, \tag{238}$$

with

$$G_\nu(\tau-\sigma)=\frac{\cosh[\nu(|\tau-\sigma|-\hbar\beta/2)]}{\sinh(\beta\hbar\nu/2)}. \tag{239}$$

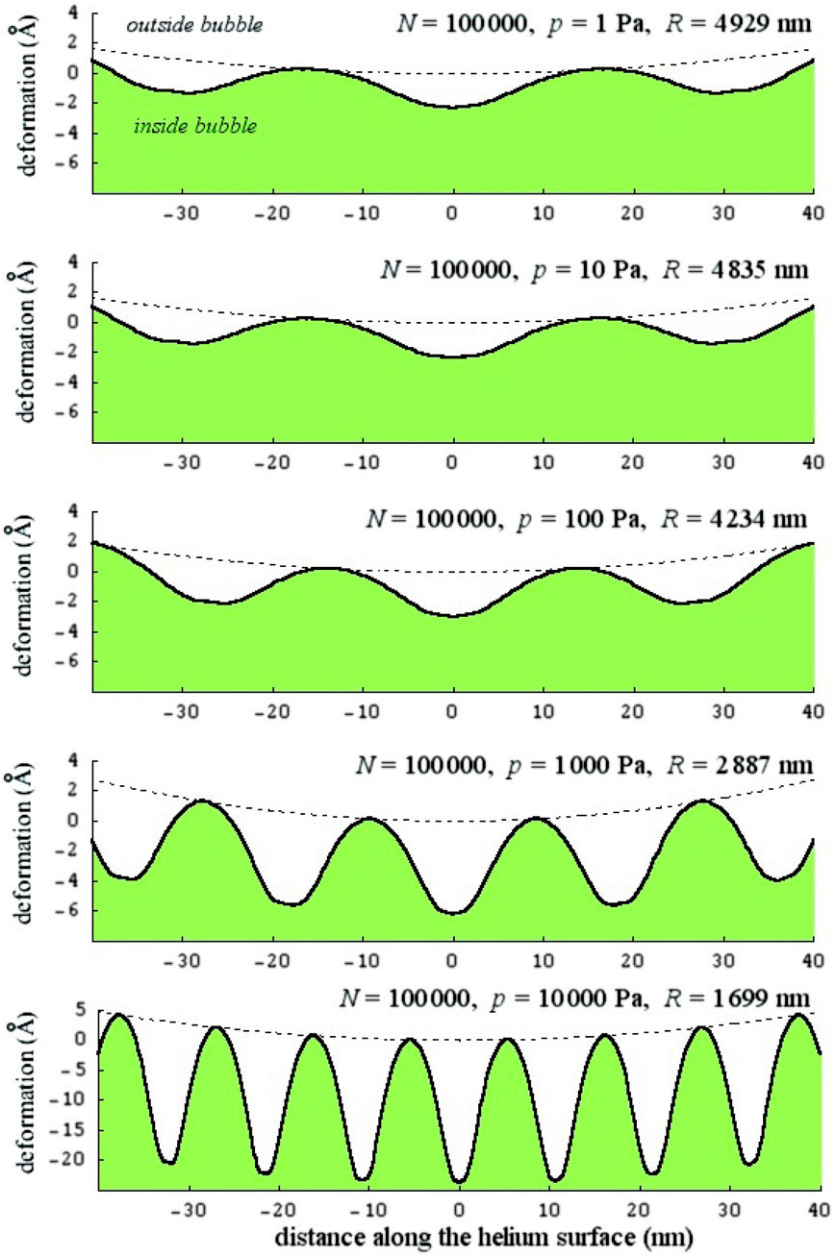

Fig. 35. For a bubble with $N = 10^5$ electrons, at different pressures the shape of the dimpled surface is shown. Electrons are present on the surface, separated from each other by the lattice parameter d. Underneath each electron there is an individual dimple, induced by the electron–ripplon interaction. As the pressure is increased, the bubble radius decreases, and the electron–ripplon interaction becomes stronger, resulting in a stronger dimpling effect. (From Ref. [88].)

In preparation of its customary use in the Jensen–Feynman inequality, the action functional (238) is written in imaginary time $t = \mathrm{i}\tau$ with $\beta = 1/(k_\mathrm{B}T)$ where T is the temperature. Following an approach analogous to that of Fratini and Quémerais for a lattice of polarons in a semiconductor [100], and to that of Klimin et al. for N polarons in a quantum dot [104], we introduce a quadratic trial action of the form

$$S_\mathrm{trial} = -\frac{1}{\hbar}\int_0^{\hbar\beta} \mathrm{d}\tau \left[\frac{m_\mathrm{e}}{2}\dot{r}^2(\tau) + \frac{m_\mathrm{e}\Omega^2}{2}r^2(\tau)\right] - \frac{Mw^2}{4\hbar}\int_0^{\hbar\beta}\mathrm{d}\tau\int_0^{\hbar\beta}\mathrm{d}\sigma\, G_w(\tau-\sigma)\mathbf{r}(\tau)\cdot\mathbf{r}(\sigma). \quad (240)$$

where M, w, and Ω are the variationally adjustable parameters. This trial action corresponds to the Lagrangian

$$\mathcal{L}_0 = \frac{m_\mathrm{e}}{2}\dot{r}^2 + \frac{M}{2}\dot{R}^2 - \frac{\kappa}{2}r^2 - \frac{K}{2}(\mathbf{r}-\mathbf{R})^2, \quad (241)$$

from which the degrees of freedom associated with R have been integrated out. This Lagrangian can be interpreted as describing an electron with mass m_e at position r, coupled through a spring with spring constant κ to its lattice site, and to which a fictitious mass M at position R has been attached with another spring, with spring constant K. The relation between the spring constants in (241) and the variational parameters w, Ω is given

by

$$w = \sqrt{K/m_e}, \tag{242}$$

$$\Omega = \sqrt{(\kappa + K)/m_e}. \tag{243}$$

Based on the trial action S_{trial}, Feynman's variational method allows one to obtain an upper bound for the free energy F of the system (at temperature T) described by the action functional S by minimizing the following function:

$$F = F_0 - \frac{1}{\beta}\left\langle S - S_{\text{trial}}\right\rangle, \tag{244}$$

with respect to the variational parameters of the trial action. In this expression, F_0 is the free energy of the trial system characterized by the Lagrangian L_0, $\beta = 1/(k_b T)$ is the inverse temperature, and the expectation value $\langle S - S_{\text{trial}}\rangle$ is to be taken with respect to the ground state of this trial system. The evaluation of expression (244) is straightforward though lengthy. We find

$$\begin{aligned} F = {} & \frac{2}{\beta}\ln\left[2\sinh\left(\frac{\beta\hbar\Omega_1}{2}\right)\right] + \frac{2}{\beta}\ln\left[2\sinh\left(\frac{\beta\hbar\Omega_2}{2}\right)\right] \\ & - \frac{2}{\beta}\ln\left[2\sinh\left(\frac{\beta\hbar w}{2}\right)\right] - \frac{\hbar}{2}\sum_{i=1}^{2} a_i^2\,\Omega_i\coth\left(\frac{\beta\hbar\Omega_i}{2}\right) \\ & - \frac{\sqrt{\pi}e^2}{D}e^{-d^2/(2D)}\left[I_0\left(\frac{d^2}{2D}\right) + I_1\left(\frac{d^2}{2D}\right)\right] \\ & - \frac{1}{2\pi\hbar\beta}\int_{1/R_b}^{\infty} dq\, q|M_q|^2\int_0^{\hbar\beta/2} d\tau \\ & \times \frac{\cosh[\omega(q)(\tau-\hbar\beta/2)]}{\sinh[\beta\hbar\omega(q)/2]}\exp\left[-\frac{\hbar q^2}{2m_e}\sum_{j=1}^{2} a_j^2\right. \\ & \left. \times \frac{\cosh(\hbar\Omega_j\beta/2) - \cosh[\hbar\Omega_j(\tau-\beta/2)]}{\Omega_j\sinh(\hbar\Omega_j\beta/2)}\right]. \end{aligned} \tag{245}$$

In this expression, I_0 and I_1 are Bessel functions of imaginary argument, and

$$D = \frac{\hbar}{m_e}\sum_{j=1}^{2}\frac{a_j^2}{\Omega_j}\coth\left(\hbar\Omega_j\beta/2\right), \tag{246}$$

$$a_1 = \sqrt{\frac{\Omega_1^2 - w^2}{\Omega_1^2 - \Omega_2^2}}; \qquad a_2 = \sqrt{\frac{w^2 - \Omega_2^2}{\Omega_1^2 - \Omega_2^2}}. \tag{247}$$

Finally, Ω_1 and Ω_2 are the eigenfrequencies of the trial system, given by

$$\Omega_{1,2}^2 = \frac{1}{2}[\Omega^2 + w^2 \pm \sqrt{(\Omega^2 - w^2)^2 + 4K/(Mm_e)}]. \tag{248}$$

Optimal values of the variational parameters are determined by the numerical minimization of the variational functional F as given by expression (245). As the reader may notice, the result of the variational path integral method is slightly less intuitive than that of the strong coupling approach of the previous subsection, nevertheless it is much more general and will allow us to introduce temperature to examine the melting of the Wigner lattice of ripplopolarons in the next subsection.

4.4.3. Wigner lattice on a sphere

On a flat surface electrons see an image charge in the helium or are pulled towards the surface of the helium by an external electric field. Due to the electron–ripplon interaction a shallow dimple is formed under the electron; however the Wigner lattice is formed because of the electronic interactions, not because of the dimple. In the MEB the electron not only feels the field from its image charge but also the electric field normal to the surface below it from all of the other electrons in the bubble. This can be two orders of magnitude stronger than the fields where instability develops on a flat surface and a narrow deep dimple forms under each electron that localizes the electrons into a lattice. As shown below, the mechanism of melting in MEB is that the electrons shed their dimples.

The Lindemann melting criterion [101,102] states in general that a crystal lattice of objects (be it atoms, molecules, electrons, or ripplopolarons) will melt when the average motion of the objects around their lattice site is larger than a critical fraction δ_0 of the lattice parameter d. It would be a strenuous task to calculate from first principles the exact value of the critical fraction δ_0, but for the particular case of electrons on a helium surface, we can make use of an experimental determination. Grimes and Adams [8] found that the Wigner lattice melts when $\Gamma = 137 \pm 15$, where Γ is the ratio of potential energy to the kinetic energy per electron. In their experiment, the electron density varied from 10^8 cm^{-2} to 3×10^8 cm^{-2} while the melting temperature T_c varied from 0.23 K to 0.66 K. At temperature T the average kinetic energy in a lattice potential V_{lat} is

$$E_{\text{kin}} = \frac{\hbar\omega_{\text{lat}}}{2}\coth\left(\frac{\hbar\omega_{\text{lat}}}{2k_B T}\right), \tag{249}$$

and the average distance that an electron moves out of the lattice site is determined by

$$\langle \mathbf{r}^2\rangle = \frac{\hbar}{m_e\omega_{\text{lat}}}\coth\left(\frac{\hbar\omega_{\text{lat}}}{2k_B T}\right) = \frac{2E_{\text{kin}}}{m_e\omega_{\text{lat}}^2}. \tag{250}$$

From this we find that for the melting transition in Grimes and Adams' experiment [8], the critical fraction equals $\delta_0 \approx 0.13$. This estimate is in agreement with previous (empirical) estimates yielding $\delta_0 \approx 0.1$ [23], and we shall use it in the rest of this treatment.

The unmodified Lindemann criterion as stated above cannot be applied to an infinite layer of electrons on helium at non-zero temperature, because (when a thermal occupation of the ripplon modes is assumed) a straightforward calculation of the average distance that an electron moves out of its lattice site yields a divergent result. This divergence is closely related to Hohenberg's theorem forbidding Bose–Einstein condensation in 2D. Therefore, many authors rely on a modified Lindemann criterion [22] that considers the average distance between two nearest neighbors instead of the average distance of a lattice resident from its lattice site. However, for the current geometry

this modification is unnecessary: the multielectron bubble is a finite and confined system, for which considerations based on Hohenberg's theorem do not apply. Hence, we shall use the unmodified Lindemann criterion to study the melting of the ripplopolaron lattice. In practice, we see that the above-mentioned divergence is not present because there is a natural cut-off wavelength for the ripplons: the lowest ripplon mode on a sphere corresponds to an $\ell = 1$ spherical harmonic, to which a characteristic wavelength of the order of $1/R_b$ can be associated. We have checked that the results do not depend on the precise value of the cut-off wavelength λ/R_b with λ on the order of 1.

Within the approach of Fratini and Quémerais [100], the Wigner lattice of (ripplo)polarons melts when at least one of the two following Lindemann criteria are met:

$$\delta_r = \frac{\sqrt{\langle \mathbf{R}_{\rm cms}^2 \rangle}}{d} > \delta_0, \tag{251}$$

$$\delta_\rho = \frac{\sqrt{\langle \boldsymbol{\rho}^2 \rangle}}{d} > \delta_0 \tag{252}$$

where ρ and $R_{\rm cms}$ are, respectively, the relative coordinate and the center of mass coordinate of the model system (241): if r is the electron coordinate and R is the position coordinate of the fictitious ripplon mass M, this is

$$\mathbf{R}_{\rm cms} = \frac{m_{\rm e}\mathbf{r} + M\mathbf{R}}{m_{\rm e} + M}; \boldsymbol{\rho} = \mathbf{r} - \mathbf{R}. \tag{253}$$

The appearance of two Lindemann criteria takes into account the composite nature of (ripplo)polarons. As follows from the physical sense of the coordinates ρ and $R_{\rm cms}$, the first criterion (251) is related to the melting of the ripplopolaron Wigner lattice towards a ripplopolaron liquid, where the ripplopolarons move as a whole, the electron together with its dimple. The second criterion (252) is related to the dissociation of ripplopolarons: the electrons shed their dimple.

The path integral variational formalism outlined in the previous section allows to calculate the expectation values $\langle \mathbf{R}_{\rm cms}^2 \rangle$ and $\langle \boldsymbol{\rho}^2 \rangle$ with respect to the ground state of the variationally optimal model system. We find

$$\begin{aligned}\langle \mathbf{R}_{\rm cms}^2 \rangle \;=\; & \frac{\hbar w^4}{m_{\rm e}[w^2(\Omega_1^2+\Omega_2^2) - \Omega_1^2\Omega_2^2]\left(\Omega_1^2-\Omega_2^2\right)} \\ & \times [\Omega_2^4(\Omega_1^2 - w^2)\coth(\hbar\Omega_1\beta/2)/\Omega_1 \\ & + \Omega_1^4(w^2-\Omega_2^2)\coth(\hbar\Omega_2\beta/2)/\Omega_2],\end{aligned} \tag{254}$$

$$\begin{aligned}\langle \boldsymbol{\rho}^2 \rangle \;=\; & \frac{\hbar}{m_{\rm e}\left(\Omega_1^2-\Omega_2^2\right)\left(\Omega_1^2-w^2\right)\left(w^2-\Omega_2^2\right)} \\ & \times [\Omega_1^3(w^2-\Omega_2^2)\coth\left(\hbar\Omega_1\beta/2\right) \\ & + \Omega_2^3(\Omega_1^2-w^2)\coth(\hbar\Omega_2\beta/2)].\end{aligned} \tag{255}$$

The procedure to find whether the Lindemann criteria are fulfilled is then as follows: first the optimal values of the variational parameters are obtained by minimization of the free energy (245), and then these optimal values are substituted in (254) and (255). Numerical calculation shows that for ripplopolarons in an MEB the inequality $\Omega_1 \gg w$ is fulfilled ($w/\Omega_1 \approx 10^{-3}$ to 10^{-2}) so that the strong coupling regime is realized, in agreement with the results of the consideration above. Owing to this inequality, we find from Eqs. (254) and (255) that

$$\langle \mathbf{R}_{\rm cms}^2 \rangle \ll \langle \boldsymbol{\rho}^2 \rangle. \tag{256}$$

So, the destruction of the ripplopolaron Wigner lattice in an MEB occurs through the dissociation of ripplopolarons, since the second criterion (252) will be fulfilled before the first (251). The results for the melting of the ripplopolaron Wigner lattice are summarized in the phase diagram shown in Fig. 36. For every value of N, pressure p and temperature T in an experimentally accessible range, this figure shows whether the ripplopolaron Wigner lattice is present (points above the surface) or molten (points below the surface). Below a critical pressure (on the order of 10^4 Pa) the ripplopolaron solid will melt into an electron liquid. This critical pressure is nearly independent of the number of electrons (except for the smallest bubbles) and is weakly temperature dependent, up to the helium critical temperature 5.2 K. This can be understood since the typical lattice potential well in which the ripplopolaron resides has frequencies of the order of THz or larger, which correspond to ~10 K.

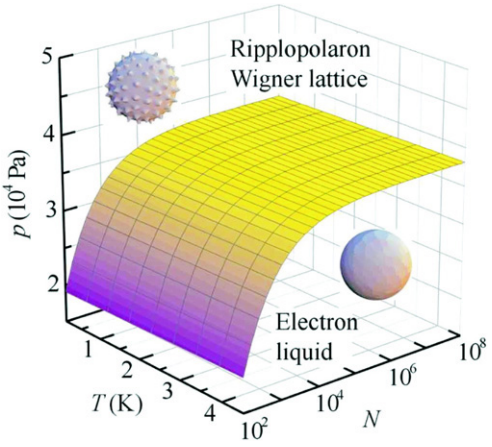

Fig. 36. The phase diagram for the spherical 2D layer of electrons in the MEB. Above a critical pressure, a ripplopolaron solid (a Wigner lattice of electrons with dimples in the helium surface underneath them) is formed. Below the critical pressure, the ripplopolaron solid melts into an electron liquid through dissociation of ripplopolarons. (From Ref. [88].)

We have established that the ripplopolaron Wigner lattice will not melt into a liquid of ripplopolarons, but rather melt through dissociation of the composite quasiparticle that is the ripplopolaron. The absence of a ripplopolaron liquid phase can be understood intuitively from the fact that the ripplon frequencies (typically GHz) are several orders of magnitude smaller than the electron frequencies in the lattice potential (typically THz). In order to create a liquid of ripplopolarons, the ripplopolarons have to move with an average velocity large enough to keep the ripplopolaron lattice molten. This motion has to be of the entire object, namely the electron and its dimple. But, at the velocities required to keep the ripplopolaron

liquid from freezing into a lattice, the dimples cannot follow the electrons. Thus, ripplopolarons only exist in a crystallized state.

The method of Ref. [58] does not allow us to derive the structure of this lattice — the mean-field approximation made for the lattice potential prohibits this. The problem of the exact lattice structure is complicated by the topology of the surface [25]: unlike for a flat surface, it is impossible to tile a sphere with a triangular lattice; frustration of the lattice in the form of point defects is unavoidable, providing nucleation points for melting the lattice. The problem of placing classical point charges on a sphere was first considered by Thomson [105] and was recently reconsidered for localized electrons in multielectron bubbles [55].

The method of Ref. [58] does allow us to study also the electron Wigner lattice, by putting $e|E| = 0$ in the above results, thus switching the electron–ripplon coupling off. A Wigner lattice of electrons is to be distinguished from a Wigner lattice of ripplopolarons. The lattice of ripplopolarons on the one hand melts through dissociation of the ripplopolarons, and this melting line is almost temperature independent. The lattice of electrons on the other hand melts though either classical thermal motion (when the temperature reaches a melting temperature of about 0.5 K), or through quantum melting when the density of electrons is large enough so that the extent of the zero-point motion becomes comparable to the lattice parameter. In the Wigner lattice of the ripplopolarons on the one hand, the particles are localized by the self-induced polaronic trapping potential (the dimple) due to the electron–ripplon interaction. In the Wigner lattice of electrons, the electrons are localized through the Coulomb interaction between the electrons. Finally, the region in phase space where the ripplopolaron Wigner lattice resides is different from the region where the electron Wigner lattice is found. This is illustrated in Fig. 37, where the phase diagram drawn in Fig. 36 is extended to huge bubbles (approaching the flat surface geometry). In the corner of largest N ($N > 10^9$, $R_b \gtrsim 1$ mm, $n_s \lesssim 10^9 - 10^{10}$ cm^{-2}) and lowest pressure ($p < 0.1$ Pa), we find that an electron Wigner lattice (without individual dimples) can still be formed below $T = 0.4$ K. The electron Wigner lattice is recovered and the melting temperature derived from our treatment is in agreement with the experimentally observed temperature [8].

The results of Ref. [58] show that, as the bubble is compressed, the electron Wigner lattice will quantum melt because of the increased density of electrons. As discussed in the introduction, the critical density for quantum melting of the electron Wigner lattice found by the present method differs from the value expected on a flat helium surface. A possible reason for this quantitative difference is that the electron–ripplon model system used in the Jensen–Feynman treatment becomes a poor trial system when the Coulomb interactions dominate the electron–ripplon interaction: the model is designed to describe the Wigner lattice of ripplopolarons rather than the electron Wigner lattice. The critical surface density for quantum melting of the electron Wigner lattice, obtained in the present formalism, turns out to be sensitive to the value $\delta = 0.13$ for the Lindemann criterion, with a larger δ leading to a better correspondence with the result

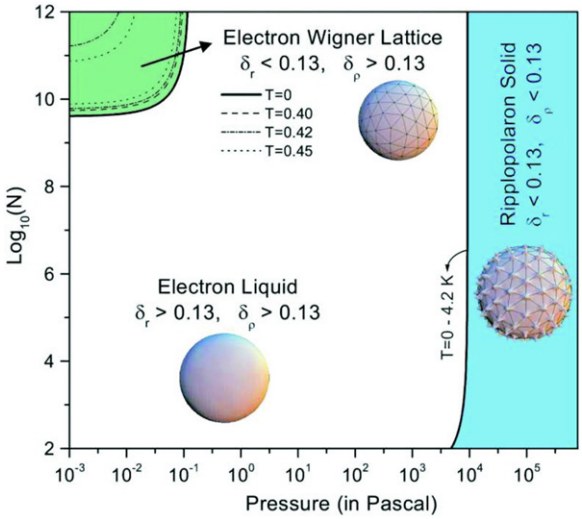

Fig. 37. The phase diagram shown in Fig. 36 is extended to reveal the relation of the ripplopolaron Wigner lattice to the Wigner lattice of electrons. These are distinct, not only in melting properties (the ripplopolaron Wigner lattice melts through dissociation of ripplopolarons), but also in their location on the phase diagram. The region for the Wigner lattice of electrons without dimples – in agreement with the observation of Grimes and Adams [8] – starts at large N and is quantum molten by pressurizing the bubble. (From Ref. [88].).

for quantum melting of the electron Wigner lattice on a flat helium surface.

The region of phase space where the electron Wigner lattice is present is separated from the region where the ripplopolaron Wigner lattice is present by a region where the predicted phase is an electron liquid. The ripplopolaron liquid phase, as mentioned before, does not exist. Since, as mentioned above, our method does not allow us to study the crystal structure, we cannot, in the electron Wigner lattice phase, distinguish between the crystalline and the hexatic phase [106].

Note that the coupled ripplon–phonon modes are a by-product of the Wigner solidification. The concept of a ripplopolaron does not a priori require Wigner solidification — the polaronic effect can in principle appear in the absence of Wigner solidification due to the electron–ripplon interaction only. However, in a bubble the ripplopolarons exist in a lattice so that we use the coupled modes rather than the bare ripplon modes.

In conclusion, owing to the difference in the ripplon and longitudinal plasmon frequencies [87], the ripplopolarons can exist in a Wigner crystallized state. This state differs from the Wigner lattice of electrons, in that the electrons in the ripplopolaron Wigner lattice are localized by the electron–ripplon interaction rather than the Coulomb repulsion, and in that the melting occurs through the dissociation of the ripplopolarons. As electron–ripplon interaction is weakened (for example by reducing the externally applied pressure on the multielectron bubble) the electrons can shed their localized dimple and the ripplopolaron Wigner state is destroyed. The melting transition occurs in a region of phase space that is accessible to recently proposed experiments for stabilizing multielectron bubbles.

The new phase that was predicted [58], the ripplopolaron Wigner lattice, will not be present for electrons on a flat helium surface. At the values of the pressing field necessary to obtain a strong enough electron–ripplon coupling, the flat helium surface is no longer stable against long wavelength deformations [11]. Multielectron bubbles, with their different ripplon dispersion and the presence of stabilizing factors such as the energy barrier against fissioning [38], allow for much larger electric fields pressing the electrons against the helium surface. The regime of N, p, T parameters, suitable for the creation of a ripplopolaron Wigner lattice, lies within the regime that would be achievable in recently proposed experiments aimed at stabilizing multielectron bubbles [27]. The ripplopolaron Wigner lattice and its melting transition might be detected by spectroscopic techniques [8,79] probing for example the transverse phonon modes of the lattice [107].

5. Superconductivity on a spherical surface

Thin films have been a subject of interest for a long time in the study of superconductivity. Superconducting films have been used [108,109] to determine the superconducting gap and to obtain measurements of the penetration depth. More recently, patterned two-dimensional superconductors have been used to probe the effects of nanoscopic confinement on superconducting properties (see for example [110]). Optical potentials can be used to confine ultracold atomic gases to two-dimensional layers. Superfluidity in these two-dimensional atomic gases occurs as a Bose–Einstein condensate (BEC) or Bardeen–Cooper–Schrieffer (BCS) states and is currently a subject of strong experimental and theoretical investigation [111,112].

The effect of surface curvature on the superconductivity of thin films has been less investigated, although there are tantalizing hints that the curvature enhances the critical temperature [113] or critical field [114]. Moreover, topological properties such as the 'hairy ball' theorem ("one cannot comb the hair on a ball in a smooth manner") ensure that vortices have to be present whenever the current is non-zero at some point on the sphere. When the curvature becomes large, so that the quantization of the angular momentum levels on the spherical surface becomes comparable to the characteristic energy scale of the BCS interaction, the superconducting properties (such as the density of states and the thermodynamic properties derived from it) become strongly modified from those of a flat, two-dimensional superconductor [59].

These differences are especially pronounced in the case of multielectron bubbles in helium. In a many-electron system on a helium surface, the mechanism that leads to superconducting pairing correlations is the electron–ripplon interaction. For flat films (electrons on a flat helium surface) ripplon-mediated superconductivity [93] would occur at a prohibitively low temperature since the electron–ripplon coupling is weak. However, as discussed in the previous section, in multielectron bubbles this interaction is stronger. In this section we therefore focus on the multielectron bubbles to illustrate the effects of curvature on superconductivity in a thin film.

5.1. Ripplon-mediated electron–electron interaction

The effective electron–electron interaction is the sum of the Coulomb interaction between the electrons and a ripplon-mediated attractive interaction between the electrons. A Feynman diagram can be used to represent the Coulomb interaction between the electrons. We can add another diagram with the same electron propagator lines, but instead of exchanging a virtual photon, exchanging a virtual ripplon. These two processes can be represented as a single exchange of energy and angular momentum using an effective interaction

$$V_{\rm eff}(\ell, m; \omega) = \frac{e^2}{2\varepsilon R}\frac{1}{2\ell+1} + M_\ell^2 \frac{2\hbar\omega_\ell}{(\hbar\omega)^2 - (\hbar\omega_\ell)^2 + i\eta}. \quad (257)$$

Both the Coulomb and the ripplon exchange interaction are given by a product of two vertex factors and one virtual particle propagator. The total electron–electron interaction Hamiltonian could be written as

$$H_{\rm int}(t) = \sum_{\ell,m}\sum_{\ell',m'}\sum_{j,n}\left[\int \frac{d\omega}{2\pi} V_{\rm eff}(j,n;\omega) e^{i\omega t}\right] \times (-1)^n \hat{c}^+_{(\ell,m)\otimes(j,n)} \hat{c}^+_{(\ell',m')\otimes(j,-n)} \hat{c}_{\ell',m'} \hat{c}_{\ell,m}.$$

Let's study for which regimes $V_{\rm eff}(j,n;\omega)$ is attractive; i.e. for which values of $(j,n;\omega)$ the ripplonic part dominates and is attractive. It is clear that small energy transfers make the ripplonic part attractive since $D^{(0)}(\ell, \omega \to 0) = -2/(\hbar\omega_\ell)$. This is good, since in general the ripplon exchange will occur with $\omega = 0$, because the ripplonic energies are much smaller than the electron level spacing. The absorption or emission of a ripplon cannot change the angular momentum of the electron due to energy conservation requirements. The effective interaction at $\omega = 0$ is

$$V_{\rm eff}(\ell, m; 0) = \frac{e^2}{2\varepsilon R}\frac{1}{2\ell+1} - \frac{2M_\ell^2}{\hbar\omega_\ell}. \quad (258)$$

The attractive interaction dominates strongly at small ℓ, as can be seen from the table below which compares $2g^2/(\hbar\omega_\sigma)$ to $e^2/2\varepsilon R$.

|attraction |/|repulsion| for small ℓ

	10^4	10^6	10^8
0 mbar	30.748	74.551	257.40
100 mbar	152.52	1419.1	14 086
3 bar	1269.0	12 594	125 841

. (259)

Yet as ℓ grows it decreases faster than the Coulomb part of the interaction: the large ℓ limit is

$$V_{\rm eff}(\ell \gg 1, m; 0) = \frac{e^2}{4\varepsilon R}\frac{1}{\ell} - \frac{2g^2}{\hbar\omega_\sigma}\frac{1}{\ell^2}.$$

The angular momentum value where the effective interaction turns from attraction into repulsion is $\ell_{V=0}$ given in the table

below.

$\ell_{V=0}$ such that $V_{\rm eff}(\ell, m; 0)$ is repulsive for $\ell \geqslant \ell_{V=0}$

	10^4	10^6	10^8
0 mbar	61	149	514
100 mbar	305	2837	28 172
3 bar	2538	25 187	251 683

.(260)

For $\ell \ll \ell_{V=0}$ the attractive part dominates. It is strongest for small ℓ and decreases roughly as ℓ^2:

$$V_{\rm eff}(\ell \leqslant \ell_{V=0}, m; 0) \approx -\frac{2M_\ell^2}{\hbar\omega_\ell} = -\frac{2g^2}{\hbar\omega_\sigma}\frac{(\ell+1/2)}{(\ell+1)(\ell^2+\ell+2+2pR/\sigma)}.$$

The strength of the effective interaction is

Effective interaction prefactor $2g^2/(\hbar\omega_\sigma)$ in K (!)

	10^4	10^6	10^8
0 mbar	228.76	25.700	4.1175
100 mbar	2302.0	2079.7	2058.1
3 bar	43 504	43 061	43 017

. (261)

The effective attractive interaction is huge (values are in K, not mK). We are clearly in a strong coupling regime, as noted in the previous section.

5.1.1. Level filling effects

Which pairs of electrons can participate in the attractive interaction though a ripplon exchange? This number will be limited because of the Fermi statistics. Electrons below the Fermi level need to be excited to an energy above the Fermi level (since their final state after interacting needs to be unoccupied). But even in order to excite an electron that was on the Fermi angular momentum L_F to angular momentum $L_F + 1$, a rather large energy $\hbar\omega$ is necessary ($\gg\hbar\omega_\sigma$), so that the ripplon-mediated interaction is no longer purely attractive. Indeed the ripplon-mediated interaction is purely attractive only for small energy transfers ($<\hbar\omega_\sigma$). At large $\hbar\omega$, the ripplon-mediated interaction has positive contributions from ripplon modes with $\omega_\ell < \omega$.

This means that the attractive interaction can only take place between two electrons on the Fermi level, and they will be scattered into final states also on the Fermi level. The energy gap to the other electronic levels is just too big to bridge. Furthermore, Fermi statistics demand that the initial states of the scattering pair are occupied and the final states are unoccupied. If the occupation of the Fermi level is $0 < f(L_F) < 1$, then the fraction of possible pairs of electrons that can participate is $f(L_F)^2[1 - f(L_F)]^2$. The important consequence of this is that if the number of electrons in the multielectron bubble is such that the Fermi level is completely filled up, the ripplon-mediated interaction is suppressed, and any superconductivity must vanish. In practice, this occurs every time the number of electrons divided by two (spin states) equals an integer squared. If superconducting correlations lower the energy substantially, it may be energetically advantageous to redistribute the electrons over several angular momentum states so more electrons can participate in pair formation.

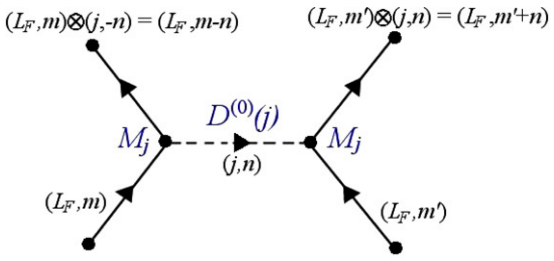

Fig. 38. The attractive BCS interaction: two electrons on the Fermi sphere are scattered into other states on the Fermi sphere by ripplon exchange.

5.1.2. Clebsch–Gordan suppression factor

The attractive interaction can only take place between two electrons on the Fermi level, and they will be scattered into final states also on the Fermi level. Fig. 38 shows a diagram which represent the attractive BCS interaction.

An electron in angular momentum state $|\text{initial}\rangle = |L_F, m\rangle$, which emits a spherical ripplon in angular momentum state $|j, n\rangle$ finds itself in the following superposition of angular momentum states

$$|\text{final}\rangle = \sum_{\ell=|L_F-j|}^{L_F+j}\sqrt{\frac{(2L_F+1)(2j+1)}{4\pi(2\ell+1)}}C \times [(L_F,0),(j,0);(\ell,0)] \times C[(L_F,m),(j,-n);(\ell,m-n)]\,|\ell,m-n\rangle\,.$$

In this expression $C[(L_F, m), (j, -n); (\ell, m - n)]$ is the Clebsch–Gordan coefficient for combining the angular momenta $\{L_F, m\}$ and $\{j, -n\}$ into $\{\ell, m - n\}$. The projection of this final state $|\text{final}\rangle$ on the Fermi level is

$$f_{CG}[(L_F,m),(j,-n)] = \sqrt{\frac{2j+1}{4\pi}}C[(L_F,0),(j,0);(L_F,0)] \times C[(L_F,m),(j,-n);(L_F,m-n)].$$

Thus, the scattering process between two electrons on the Fermi energy, with $m, m' \in \{-L_F, L_F\}$, can be described in second quantization as

$$\hat{V}_{\rm BCS} = \sum_{m=-L_F}^{L_F}\sum_{m'=-L_F}^{L_F}\sum_{j,n} f_{CG}[(L_F,m),(j,-n)] \times f_{CG}[(L_F,m'),(j,n)] \times f(L_F)^2[1-f(L_F)]^2 V_{\rm eff}(j,n;0) \times \hat{c}^+_{L_F,m-n}\hat{c}^+_{L_F,m'+n}\hat{c}_{L_F,m'}\hat{c}_{L_F,m}.$$

This interaction Hamiltonian derived for the multielectron bubble is already close to a BCS-like interaction Hamiltonian, as it involves only electrons on the Fermi surface and couples them with an attractive potential. We included the Fermi filling factor, as a 'statistical averaging' so that we can for this Hamiltonian always assume that the initial state is occupied and the final state unoccupied. In a statistical averaging over the ensemble of equivalent microscopic states there will always be members of the ensemble for which this is true. The fraction

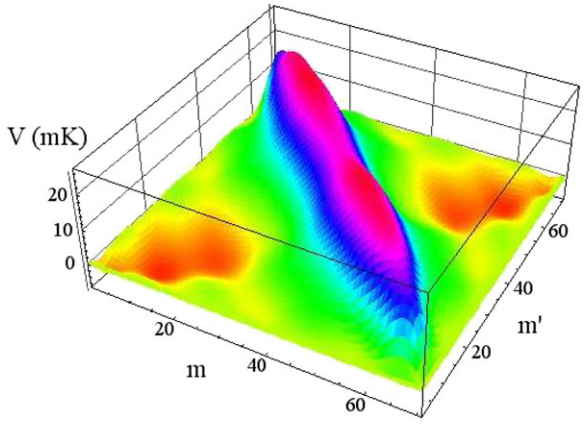

Fig. 39. The effective interaction strength between electrons on the Fermi level of a $N = 10^4$, $p = 0$ bubble for $\{m, m'\}$ pairs of electrons. (For interpretation of the references to colour in this figure legend, the reader is referred to the web version of this article.)

of such members with respect to the total is exactly our Fermi filling factor $f(L_F)^2[1 - f(L_F)]^2$.

An initial state with a pair characterized by $\{m, m'\}$ can be scattered into a pair with $\{m - n, m' + n\}$ in various ways: namely by the scattering of a virtual ripplon with $j = n, n + 1, n + 2, \ldots$. provided that j is an even mode to obey the triangle sum. All these processes are indistinguishable (initial and final states are exactly the same) and their diagrams should be added to get the overall amplitude. Different combinations of Clebsch–Gordan coefficients will occur, which can take either a positive or a negative sign: the different diagrams can interfere constructively but also destructively. The only $\{m, m'\}$ pairs where we are sure that the different contributions will interfere constructively, is for pairs of electrons with opposite angular momentum $m' = -m$. The reason for this is that $C[(L_F, m), (j, n); (L_F, m + n)]$ has the same sign as $C[(L_F, -m), (j, -n); (L_F, -m - n)]$.

Let's take a closer look at the example bubble with $N = 10^4$ and $p = 0$ to see what is going on with the electron pairs for which $m' \neq -m$. This is shown in Fig. 39. The pairs of electrons are characterized by the m, m' values which are shown on the x, y axis respectively. The z-axis, which is color-coded from red (low) over yellow, green, blue to violet and red again (high), shows the value of $V_{\text{eff}}(j, n; 0) \times f_{CG}[(L_F, m), (j, -n)] f_{CG}[(L_F, m'), (j, n)]$ added up for different values of the ripplon angular momentum j, n. The full sum (as defined in the next section) was broken off at a value $j = 10$, but the effect is already apparent: the total effective interaction is strongly reduced for pairs of electrons which do not have opposite angular momentum ($m' \neq -m$).

5.2. BCS theory for the multielectron bubble

As we have established that the properties of the ripplon-mediated electron–electron interaction lead to a BCS-type attractive interaction between the electrons, we can go through the motions of BCS theory mutatis mutandis. From the previous section we know that the interaction between the electrons can be written in the form of a BCS interaction term given by

$$\hat{H}_{\text{int}}^{(\text{BCS})} = -\sum_{m=-L_F}^{L_F} \sum_{m'=-L_F}^{L_F} \tilde{V}_{m,m'} \hat{c}^{+}_{L_F,-m'\downarrow} \times \hat{c}^{+}_{L_F,m';\uparrow} \hat{c}_{L_F,m;\uparrow} \hat{c}_{L_F,-m;\downarrow}, \tag{262}$$

where $\sigma = \uparrow, \downarrow$ denotes spin up and spin down and with

$$\tilde{V}_{m,m'} = f(L_F)^2[1 - f(L_F)]^2 \sum_{j=\max[2,|m-m'|]}^{2L_F} \frac{2g^2}{\hbar\omega_\sigma} \times \frac{(j + 1/2)}{(j + 1)(j^2 + j + 2 + 2pR/\sigma)} \times f_{CG}[(L_F, m), (j, m' - m)] \times f_{CG}[(L_F, -m), (j, m - m')]. \tag{263}$$

Due to the coefficients $C[(L_F, 0), (j, 0); (L_F, 0)]$ the summation cannot run further than $2L_F$ and only even values of j contribute. The summation starts from $n = |m - m'|$, or if this is less than 2, it starts at $\ell = 2$. The reason is that the $\ell = 0$ deformation is not taken into account (it is the radius of the bubble), and the $\ell = 1$ deformation is only a uniform translation which by definition cannot couple to the internal degrees of freedom.

The BCS variational wave function is given by

$$|\Phi_{\text{BCS}}\rangle = \prod_{\ell,m} (u^*_{\ell,m} + v_{\ell,m} \hat{c}^{+}_{\ell,m;\uparrow} \hat{c}^{+}_{\ell,-m;\downarrow}) |0\rangle, \tag{264}$$

where $|0\rangle$ is the electron vacuum. This wave function is a product of pair wave functions (and thus represents an even number of electrons). The Bogoliubov transformation is

$$\hat{\alpha}_{\ell,m;\sigma} = u^*_{\ell,m} \hat{c}_{\ell,m;\sigma} - \sigma v_{\ell,m} \hat{c}^{+}_{\ell,-m;-\sigma} \tag{265}$$

$$\Leftrightarrow$$

$$\hat{c}_{\ell,m;\sigma} = u_{\ell,m} \hat{\alpha}_{\ell,m;\sigma} + \sigma v_{\ell,m} \hat{\alpha}^{+}_{\ell,-m;-\sigma}, \tag{266}$$

where we impose that

$$u_{\ell,-m} = u_{\ell,m} \quad \text{and} \quad v_{\ell,-m} = v_{\ell,m},$$

and we use the convention that $\sigma = +1$ corresponds to spin up $\uparrow$ and $\sigma = -1$ corresponds to spin down $\downarrow$. The variational parameters must satisfy

$$u_{\ell,m} u^*_{\ell,m} + v_{\ell,m} v^*_{\ell,m} = 1, \tag{267}$$

so that the $\alpha^{+}_{\ell,m;\sigma}$ operators obey the Fermionic anticommutator rule given by $\left\{\hat{\alpha}_{\ell',m';\sigma'} \hat{\alpha}^{+}_{\ell,m;\sigma}\right\} = \delta_{\ell\ell'}\delta_{mm'}\delta_{\sigma\sigma'}$. The usefulness of these Bogoliubov transformed operators stems from the property that they have the BCS wave function as their vacuum. The expectation value of the kinetic energy is given by

$$E = \left\langle \Phi_{\text{BCS}} \left| \sum_{\ell m,\sigma} \xi_\ell \hat{c}^{+}_{\ell,m;\sigma} \hat{c}_{\ell,m;\sigma} \right| \Phi_{\text{BCS}} \right\rangle + \left\langle \Phi_{\text{BCS}} \left| \hat{H}_{\text{int}}^{(\text{BCS})} \right| \Phi_{\text{BCS}} \right\rangle. \tag{268}$$

Remember that $\xi_\ell = E_\ell - E_F$ is the energy measured from the Fermi surface. Using the Bogoliubov transformation, this yields

$$E = 2\sum_{\ell m}\xi_\ell \left|v_{\ell,m}\right|^2 - \sum_{m,m'=-L_F}^{L_F}\tilde{V}_{m,m'} \times \left[v^*_{L_F,m'}u^*_{L_F,m'}u_{L_F,m}v_{L_F,m} - |v_{\ell,m}|^4\delta_{m,m'}\right]. \quad (269)$$

In the last sum, the first term between square brackets corresponds to

$$v^*_{\ell,m'}u^*_{\ell,m'}u_{\ell,m}v_{\ell,m} = \left\langle \Phi_{\rm BCS}\left|\hat{c}^+_{\ell,-m';\downarrow}\hat{c}^+_{\ell,m';\uparrow}\right|\Phi_{\rm BCS}\right\rangle \times \left\langle \Phi_{\rm BCS}\left|\hat{c}_{\ell,m;\uparrow}\hat{c}_{\ell,-m;\downarrow}\right|\Phi_{\rm BCS}\right\rangle, \quad (270)$$

whereas the second term in corresponds to

$$|v_{\ell,m}|^4\delta_{m,m'} = \left\langle \Phi_{\rm BCS}\left|\hat{c}^+_{\ell,m';\uparrow}\hat{c}_{\ell,m;\uparrow}\right|\Phi_{\rm BCS}\right\rangle \times \left\langle \Phi_{\rm BCS}\left|\hat{c}^+_{\ell,-m';\downarrow}\hat{c}_{\ell,-m;\downarrow}\right|\Phi_{\rm BCS}\right\rangle. \quad (271)$$

The second term in (269) is incorporated into the single-particle energies ξ_ℓ and represents a mean-field correction to those energies. Introducing the usual gap

$$\Delta_{\ell,m} = \sum_{m'}\tilde{V}_{m,m'}u_{L_F,m'}v_{L_F,m'} \quad (272)$$

leads to

$$E = 2\sum_{\ell m}\xi_\ell\left|v_{\ell,m}\right|^2 - \sum_{m=-L_F}^{L_F}\Delta_{L_F,m}v^*_{L_F,m'}u^*_{L_F,m'} - \sum_{m=-L_F}^{L_F}\Delta^*_{L_F,m}v_{L_F,m'}u_{L_F,m'}. \quad (273)$$

This energy is minimized by

$$v_{\ell,m} = \sin(\theta_{\ell,m}/2) \quad \text{and} \quad u^*_{\ell,m} = \cos(\theta_{\ell,m}/2) \quad (274)$$

with

$$\sin\left(\theta_{L_F,m}\right) = \frac{\left|\Delta_{L_F,m}\right|}{\sqrt{\left|\Delta_{L_F,m}\right|^2 + \xi^2_{L_F,m'}}}, \quad (275)$$

$$\cos\left(\theta_{L_F,m}\right) = \frac{\xi'_{L_F,m}}{\sqrt{\left|\Delta_{L_F,m}\right|^2 + \xi^2_{L_F,m'}}}. \quad (276)$$

This leads to the gap equation

$$\left|\Delta_{L_F,m}\right| = \frac{1}{2}\sum_{m'}\tilde{V}_{m,m'}\frac{\left|\Delta_{L_F,m'}\right|}{\sqrt{\left|\Delta_{L_F,m'}\right|^2 + \xi^2_{L_F,m'}}}. \quad (277)$$

Noting that at the Fermi level $\xi^2_{L_F,m'} = 0$, we get

$$\left|\Delta_{L_F,m}\right| = \frac{1}{2}\sum_{m'}\tilde{V}_{m,m'}\frac{1}{\left|\Delta_{L_F,m'}\right|}. \quad (278)$$

From Fig. 39 in the previous subsection, we find that the potential energy of a pair of electrons is nearly constant along the $m = -m'$ ridge. This is what one would expect in a spherically symmetric system: no preferential direction should exist and the gap and $\xi'_{L_F,m}$ should be independent of m. So we use the averaged interaction

$$G = \frac{1}{(2L_F+1)^2}\sum_{m,m'}\tilde{V}_{m,m',L_F}. \quad (279)$$

Values for G for various configurations are given in Fig. 40.

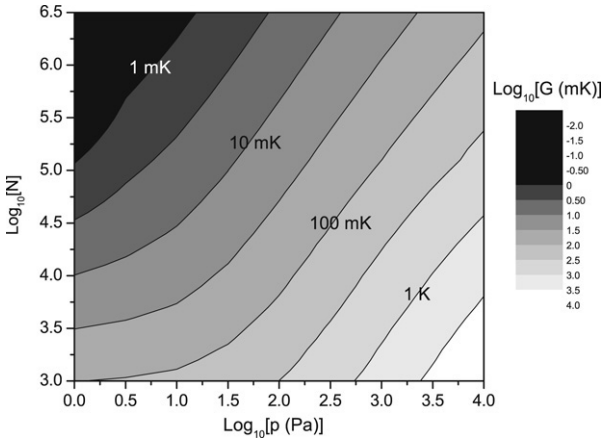

Fig. 40. BCS interaction strength G (in mK) as a function of pressure p and number of electrons N in the bubble (from [59]).

This yields the following result for the gap

$$\left|\Delta_{L_F}\right| = \left|(2L_F+1)G/2\right|. \quad (280)$$

The BCS energy in the superconducting state is

$$\begin{aligned} E_0 &= \sum_m\left[2\xi_{L_F}\sin^2(\theta_{\ell,m}/2) - \frac{1}{2}\left|\Delta_{L_F,m}\right|\sin(\theta_{\ell,m})\right] \\ &= E_N - \sum_m\left[\xi_{L_F}\cos(\theta_{\ell,m}) - \frac{1}{2}\left|\Delta_{L_F,m}\right|\sin(\theta_{\ell,m})\right] \\ &= E_N - \sum_m\left[\frac{(\xi_{L_F,m})^2}{\sqrt{\left|\Delta_{L_F,m}\right|^2 + (\xi_{L_F,m})^2}} + \frac{1}{2}\frac{\left|\Delta_{L_F,m}\right|^2}{\sqrt{\left|\Delta_{L_F,m}\right|^2 + (\xi_{L_F,m})^2}}\right]. \end{aligned} \quad (281)$$

Thus,

$$E_0 - E_N = \frac{1}{2}\left|(2L_F+1)G/2\right|. \quad (282)$$

As can be seen from the numerical values for G shown in Fig. 40, this energy gain can be larger than the level splitting between angular momentum states. Thus, it can be advantageous to redistribute the electrons on to different angular momentum state, even though for such a redistribution there is not enough thermal energy and even though ripplons cannot scatter electrons from one angular momentum state to another. To investigate this effect further, we employ Richardson's method yielding exact solutions for the case of a superconductor on a spherical surface.

5.3. Richardson method on the sphere

In the preceding subsections we argued that multielectron bubbles are a suitable candidate to observe pairing of electrons in a spherical two-dimensional system. Note that only electrons within the same angular momentum energy level L interact: only *intra*level interactions take place, but no *inter*level interactions. This is due to the fact that the relevant ripplon energies are much smaller than the interlevel energy splitting. So, the set of electrons with a given angular momentum L can be considered as an independent subsystem, described by the Hamiltonian (262). The full system is the collection of independent subsystems characterized by different L. The effective BCS Hamiltonian we obtained can be expressed as a sum over independent subsystems with different angular momentum,

$$\hat{H}_{\text{eff}} = \sum_L \hat{H}_L \tag{283}$$

with

$$\hat{H}_L = \sum_{m,\sigma} \epsilon_L \hat{c}^+_{L,m;\sigma} \hat{c}_{L,m;\sigma} - G \sum_{m,m'=-L}^{L} \hat{c}^+_{L,-m'\downarrow} \hat{c}^+_{L,m';\uparrow} \hat{c}_{L,m;\uparrow} \hat{c}_{L,-m;\downarrow}. \tag{284}$$

We introduce the notation ϵ_L rather than E_L to emphasize that the analysis described from here onwards can be applied to the general problem of a S2DEG with attractive interactions between electrons on the same angular momentum level. The previous section provides possible values for the coupling constant G (see Fig. 40) and for the relevant energy scales, and a justification for the applicability of the effective pairing Hamiltonian (262) to multielectron bubbles specifically. Nevertheless the results derived in this section can be used to investigate other systems such as the superconducting properties of thin electronic nanoshells, or can be investigated as an academic question regarding spherical electronic systems.

Setting $\forall(i) : \varepsilon_i = \epsilon_L$ and

$$\hat{b}_{m;\uparrow} = \hat{c}_{L,m;\uparrow}, \qquad \hat{b}_{m;\downarrow} = \hat{c}_{L,-m;\downarrow}, \tag{285}$$

in (284) we obtain the so-called reduced BCS Hamiltonian [116,117]:

$$\hat{H}_{\text{BCS}} = \sum_{i,\sigma} \epsilon_i \hat{b}^+_{i,\sigma} \hat{b}_{i,\sigma} - G \sum_{i,i'} \hat{b}^+_{i',\uparrow} \hat{b}^+_{i',\downarrow} \hat{b}_{i,\downarrow} \hat{b}_{i,\uparrow}. \tag{286}$$

Richardson [115] derived an exact solution for this reduced BCS Hamiltonian. The solution method amounts to solving a set of n non-linear coupled equations.

In general, the aforementioned set of equations can be solved only by numerical computation. However, in the particular case when all the involved single-particle states belong to one and the same energy level – as is the case for a spherical multielectron bubble – the energy of electron pairs can be easily found analytically [118]. The result for the energy of electrons in the subsystem characterized by angular momentum L can be written down as

$$E_{L,n_L,g_L,b_L} = (2n_L + b_L)\epsilon_L - G(n_L - g_L) \times (2L - b_L + 2 - n_L - g_L). \tag{287}$$

Three quantum numbers characterize the energy levels of the subsystem with angular momentum L. The quantum number n_L corresponds to the number of electron pairs, whereas b_L represents the number of unpaired electrons. The quantum number g_L indexes the number of elementary bosonic pair-hole excitations [119] in the system of n_L pairs. These are bosonic excitations that involve a redistribution of the amplitude for correlated pairs over the $2L + 1$ states with angular momentum L. Note that $g_L = 0$ corresponds to the ground state for the correlated pairs. The pair-hole excitations can be thought of intuitively as collective excitations of the condensate of Cooper pairs, whereas b_L rather represents the broken Cooper pairs. For example, if two bare single-electron states $|L, m; \uparrow\rangle$ and $|L, -m; \downarrow\rangle$ are occupied in level L, this electron pair should be counted in n_L, the total number of such pairs. It is clear that n_L has to be less than or equal to $2L + 1$. Now consider the 'broken pair' case where only one state of the pair $|L, m; \uparrow\rangle$ and $|L, -m; \downarrow\rangle$ is occupied. The unpaired electron cannot participate in the scattering described by the interaction term in (284) and electron pairs cannot scatter into the pair of states $|L, m; \uparrow\rangle, |L, -m; \downarrow\rangle$ because one of these states is already occupied. The states $|L, m; \uparrow\rangle, |L, -m; \downarrow\rangle$ are blocked for scattering of pairs. The number of these blocked spin degenerate bare states equals the number of unpaired electrons, and is denoted by b_L. The total number of electrons in angular momentum level L is then $2n_L + b_L \leq 2(2L + 1)$.

The total energy can be expressed as a sum of the energies for each independent subsystem:

$$E_{\{n_L,b_L,g_L\}_{L=1,2,3,\ldots}} = \sum_{L=0}^{\infty} E_{L,n_L,g_L,b_L}. \tag{288}$$

The state of the entire system is characterized by a large set of quantum numbers, three (n_L, b_L, g_L) for each angular momentum subsystem.

5.3.1. Ground state properties

Consider the ground state of a bubble with an even number of electrons. Given the constraint that the total number of electrons on the sphere is constant, the number of electrons on each angular momentum level can be adapted. As noted before, it can be energetically advantageous to redistribute the electrons over several angular momentum levels around L_F in order to achieve the lowest energy. The ground state in a bubble with even N is characterized by $g_L = 0$ and $b_L = 0$ for all L. In order to find the ground state configuration of n_L, let us consider the variation of the total energy, $\Delta E_{L,L+1}$, due to a transfer of an electron pair from the Lth energy level to the next higher level. Using (287) with $g_L = b_L = 0$, we find

$$\Delta E_{L,L+1} = 4\epsilon_1(L + 1) - 2G\,(n_L - n_{L+1})\,, \tag{289}$$

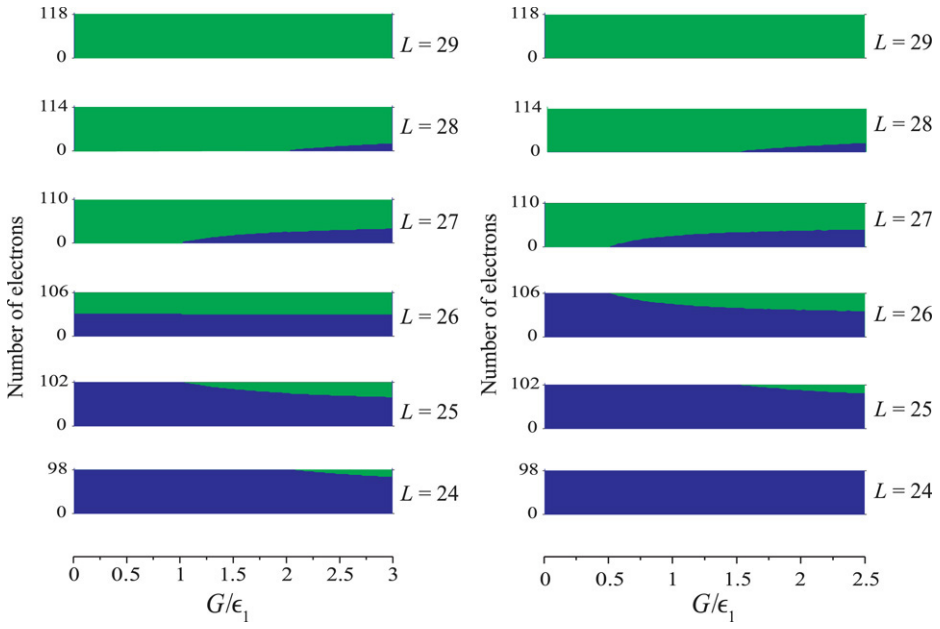

Fig. 41. The filling of single-particle states in the angular momentum subsystems is shown as a function of the BCS interaction strength G/ϵ_1 expressed in units $\epsilon_1 = \hbar/(m_e R^2)$. Dark (light) shade corresponds to filled (empty) levels. From Ref. [59].

with $\epsilon_1 = \hbar/(m_e R^2)$. Thus a transfer *reduces* the total energy if the inequality

$$G\,(n_L - n_{L+1}) > 2\epsilon_1(L+1) \tag{290}$$

is satisfied. Of course, this inequality is not satisfied at $n_L \leq n_{L+1}$, so that an inverted population of levels never appears in the ground state.

Condition (290) is never fulfilled also at weak interaction: the difference $(n_L - n_{L+1})$ cannot exceed the value $2L+1$, which corresponds to completely filled Lth level and empty level $L+1$. Therefore, condition (290) cannot be satisfied for $G < \epsilon_1(L+1)/(2L+1)$ which simplifies to $G < \epsilon_1/2$ for $L \gg 1$. Such a "weak interaction" case is realized in MEBs with the total number of electrons $N_{\rm tot} < 4 \times 10^3$ and $p = 0$. The opposite limit, $G \gg \epsilon_1/2$, will here be referred to as the strong coupling case. In this case, we deduce from condition (290) that ground state configuration will be such that the number of electron pairs gradually decreases from level to level by approximately $\epsilon_1 L_F/G$ for approximately $2G/\epsilon_1$ energy levels around the level $L = L_F$. In order to illustrate and further confirm this conclusion, drawn from the above analytical consideration, we show in Fig. 41 the ground state electron distributions, obtained by an exact numerical minimization of the total energy with respect to n_L. The results are shown as a function of G/ϵ_1 for fixed $L_F = 26$ and two different values of N_F, the ground state number of electrons on the level $L = L_F$ in the "normal" MEB (i.e., at $G = 0$): $N_F = 52$ (approximately half filling; left panel of Fig. 41) and $N_F = 106$ (closed shell; right panel of Fig. 41). We do not expect any qualitative changes of the electron distribution patterns with increasing L_F. Dark (light) color corresponds to filled (empty) states on the energy levels.

In order to get an idea of how important the redistribution of electron pairs is for the pairing characteristics, the difference in energy between the state with pairing correlations and the state with $G = 0$ can be examined. This energy difference is the condensation energy

$$E^{\rm C}(G) = E_{\rm gs}(0) - E_{\rm gs}(G) - nG,$$

where $E_{\rm gs}(G)$ is the ground state energy at a given G and n is the total number of electron pairs on the sphere. The condensation energy is always a non-decreasing function of the interaction strength. A less trivial result is that at $2G/\epsilon_1$ the slope of $E^{\rm C}(G)$ rapidly rises with G: in the absence of the electron redistribution between the energy levels the condensation energy would be merely a linear function of G as predicted by expression (282). Such a linear behavior of $E^{\rm C}$ versus G is seen indeed in the case $G < \epsilon_1/2$.

Another interesting result of the electron redistribution is that the condensation energy, which is strongly influenced by N_F at "weak interaction" $G < \epsilon_1/2$ (in particular, the condensation energy is zero in the case, when the shell $L = L_F$ is closed, and reaches a maximum for half-filling of this shell), becomes almost independent of N_F when G significantly exceeds $\epsilon_1/2$. The reason for insensitivity of the obtained $E^{\rm C}$ to N_F at large $2G/\epsilon_1$ is that for sufficiently strong interaction the ground state electron configuration is qualitatively the same independently of N_F: there is a set of approximately $2G/\epsilon_1$ energy levels, whose population linearly decreases with L from almost complete filling to zero.

5.3.2. *Density of states*

Having obtained the ground state, we analyze the effect of the pairing interaction on the density of (many-electron) states. This density of states can be written down as

$$D(E) = \sum_i J^{(i)} \delta(E - E^{(i)}), \tag{291}$$

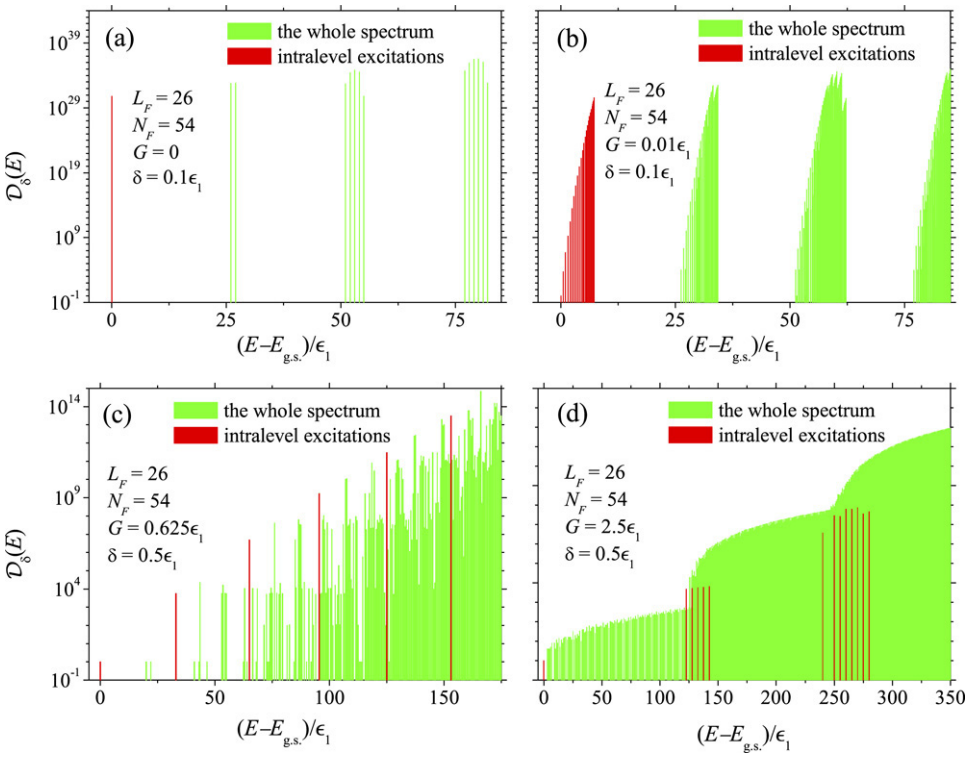

Fig. 42. The density of states $D_\delta(E)$ is shown as a function of the energy (above the ground state energy) for increasing BCS interaction strength G (from [59]).

where the energy levels $E^{(i)}$ and their degeneracy $J^{(i)}$ are given by the expressions

$$E^{(i)} = \sum_L E_{Ln_Lg_Lb_L}, \tag{292}$$

$$J^{(i)} = \prod_L J_{Ln_Lg_Lb_L}, \tag{293}$$

with

$$J_{Lg_Lb_L} = 2^{b_L} C_{b_L}^{2L+1} \times \begin{cases} 1, & g_L = 0 \\ \left(C_{g_L}^{2L+1-b_L} - C_{g_L-1}^{2L+1-b_L}\right), & g_L \geq 1. \end{cases} \tag{294}$$

where C_n^k are binomial coefficients. [118].

Instead of a sum of delta functions, it is more convenient to consider instead of $D(E)$ the quantity

$$D_\delta(E) = \int_{E-\delta/2}^{E+\delta/2} \mathrm{d}E\, D(E),$$

which gives the number of (many-electron) states in the energy range of width δ around the energy E. First we will restrict ourselves to the case of a bubble with an even number of electrons. The calculations are performed for fixed $L_F = 26$ and $N_F = 54$ (approximately half filling), where L_F is the orbital quantum number for the uppermost occupied single-electron energy level in the ground state at $G = 0$, while N_F is the ground state number of electrons on this level at $G = 0$.

In Fig. 42 the evolution of $D_\delta(E)$ with increasing G is shown. *Intralevel* excitations are characterized by either increasing b_L (creating broken pairs) or increasing g_L (creating pair-hole excitations) while keeping the total number of electrons in the angular momentum subsystem L constant. The energy required to break a Cooper pair can be found by setting $n_L \to n_L - 1, b_L \to b_L + 2$. The minimal energy required to break a Cooper pair is

$$\Delta_{\text{pair-breaking}} = E_{L,n_L-1,0,2} - E_{L,n_L,0,0} = G\,(2L+1)\,. \tag{295}$$

The energy required to form a pair-hole excitation of the pair condensate is found by setting $g_L \to g_L + 1$. The minimal energy required for a pair-hole excitation is

$$\Delta_{\text{pair-hole}} = E_{L,n_L,1,0} - E_{L,n_L,0,0} = G\,(2L+1)\,. \tag{296}$$

This is equal to the minimal energy for a pair-breaking excitation, and corresponds to the superconducting gap in the limit of a flat electron system. In Fig. 42 the intralevel excitations are shown as dark peaks; the distance between the first two peaks in the intralevel excitation density of states increases as G increases. In the weak coupling regime ($2G/\epsilon_1 \ll 1$) the energy required to transfer a Cooper pair from one angular momentum subsystem to another is much larger than the energy required for intralevel excitations. The density of states remains similar to the usual angular momentum level spectrum, broadened by the intralevel excitations as in panel (b) of Fig. 42. However, in the strong coupling regime ($2G/\epsilon_1 \gg 1$) the energy to break a Cooper pair or create a pair-hole excitation exceeds the energy necessary to transfer a pair from one L subsystem to another. In this regime, there exist excitations below the gap for breaking pairs or creating pair-hole excitations, as can be seem in panels (c) and (d) of Fig. 42. With increasing G, the excitation spectrum tends to become quasicontinuous, with jumps of several orders of magnitude

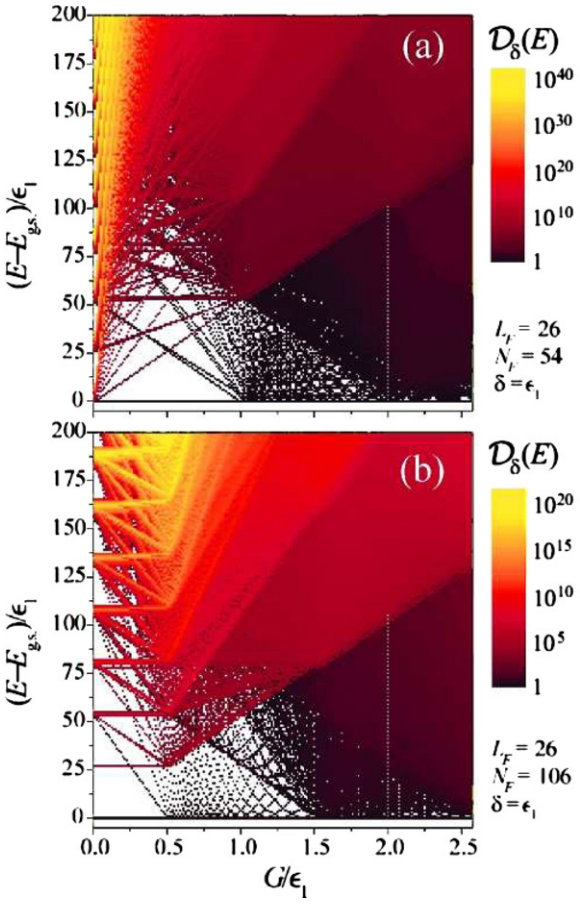

Fig. 43. The density of states is shown as a function of the excitation energy and of G. The evolution from a set of discrete bands close to the angular momentum level spectrum at small G towards a quasicontinuum at large G with steps at the pair-breaking energy can be seen (from Ref. [59]).

in $\mathcal{D}_\delta(E)$ near the energies corresponding to pair-breaking or pair-hole excitations. Between these jumps there is a more uniform distribution of excitations, corresponding to interlevel transitions of pairs. Even though the density of states does not tend to zero below the pair-breaking gap, this sudden jump still constitutes distinctive feature at the pair-breaking gap.

Fig. 43 provides an overview of the behavior of $D_\delta(E)$ as a function of both E and G. One can see an interplay between intralevel excitations, whose energies always increase with increasing G, and excitations, which correspond to interlevel transitions of pairs. For the latter, both an increase and a decrease in energy are possible with increasing G.

For $G = 2\epsilon_1$, a quite periodical pattern of $D_\delta(E)$ is seen in Fig. 43 at energies below the first intralevel excitation. The origin of such periodicity can be easily understood from (289) or the more general expression

$$\Delta E_{L,L+\Delta L} = 4\epsilon_1 \Delta L(L+\Delta L) - 2G\left(n_L - n_{L+\Delta L} + \Delta L - 1\right), \tag{297}$$

which gives the variation of the total energy due to a transfer of an electron pair from the Lth bare energy level to the level with the orbital quantum number $(L+\Delta L)$ (in the absence of broken pairs and pair-hole excitations). Thus, as seen from

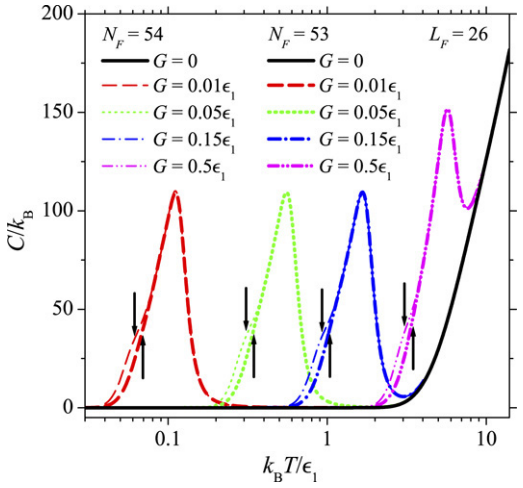

Fig. 44. The specific heat as a function of temperature, for different values of $G \leqslant \epsilon_1/2$ and for $G = 0$, for a system with an odd and an even number of electrons. The arrows indicate the estimates for the critical temperature discussed in the text. From Ref. [120].

(297), at $G = 2\epsilon_1$ only the excitation energies divisible by $2\epsilon_1$ are possible at any L, ΔL, n_L and $n_{L+\Delta L}$.

5.4. Specific heat and critical temperature

The expressions (292) and (293) for the energy levels E_j and their degeneracies J_j allow us to compute the specific heat straightforwardly

$$C = \frac{\mathrm{d}\langle E\rangle}{\mathrm{d}T}, \tag{298}$$

where $\langle E\rangle$ is the statistical average energy of the electrons in the MEB:

$$\langle E\rangle = \frac{\sum_j J_j E_j \exp\left[-E_j/(k_B T)\right]}{\sum_j J_j \exp\left[-E_j/(k_B T)\right]}. \tag{299}$$

The result for the specific heat [120] is shown in Fig. 44 in the weak interaction regime $2G/\epsilon_1 \leqslant 1$, and in Fig. 45 for the regime $2G/\epsilon_1 > 1$.

In the case of $G = 0$, the system behaves as a collection of quantum rotors and the specific heat capacity vanishes at low temperatures. An increase of C with T starts at temperatures which correspond to non-negligible occupation probabilities for the lowest excited (many-electron) states. These excited states are separated from the ground state by an energy of the order $\epsilon_1(L_F+1)$ and correspond to transitions of electrons between adjacent single-electron energy levels with different L. The aforementioned energy spacing – together with the ratio between the number of the lowest exited states and the degeneracy of the ground state – determine the characteristic temperature for the onset of non-zero C.

As seen from Fig. 44, at small non-zero G ($G \ll \epsilon_1$) an additional peak of $C(T)$ appears at a temperature lower than that at which the specific heat in the normal state (with $G = 0$) starts to increase. This peak due to the intralevel pair-breaking and pair-hole excitations: At $G \ll \epsilon_1$, these intralevel

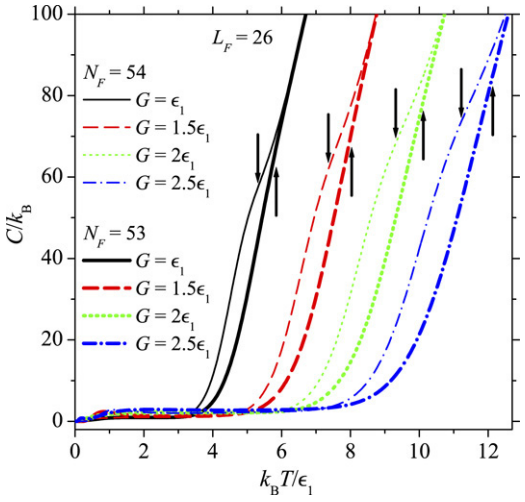

Fig. 45. The specific heat as a function of temperature, for different values of $G > \epsilon_1/2$, for a system with an odd and an even number of electrons. The arrows indicate the estimates for the critical temperature discussed in the text. From Ref. [120].

excitations are characterized by much smaller energies than the transitions between single-electron levels with different L. In the case of a closed shell configuration, no intralevel excitations from the ground state are possible, so that no additional peak of $C(T)$ appears at $G \ll \epsilon_1$. With increasing G, the peak of $C(T)$ which corresponds to pair-breaking and pair-hole excitations, shifts towards higher temperatures. For $G > \epsilon_1/2$ the pair-breaking and pair-hole excitation energy is larger than the interlevel transition energy, so that the extra peak is not present, cf. Fig. 45. Nevertheless, in the density of states there is still a marked increase in at the pair-breaking and pair-hole excitation energy, so that this energy can still be identified through the onset of a rapid increase in the specific heat as a function of temperature.

The behavior of the specific heat as a function of temperature allows us to identify a characteristic temperature T^* at which pair-breaking processes occur. Both for odd and even systems, the initial rise in the specific heat as a function of temperature is caused by pair-breaking excitations. For $G < \epsilon_1/2$ the characteristic temperature will correspond to the temperature at which the peak (see Fig. 44) in $C(T)$ appears. For $G > \epsilon_1/2$ the onset of the fast increase in $C(T)$ can be identified with this characteristic temperature. For temperatures larger than this characteristic temperature, many-body states with broken pairs or pair-hole excitations are populated and the pairing correlations become suppressed. Thus, the characteristic temperature T^* can be interpreted as the critical temperature for superconductivity.

It is possible to make an analytical estimate for T^*. The probability for the system to be in the ground state is proportional to $P_{\rm gs} = J_{\rm gs} \exp\left(-E_{\rm gs}/k_{\rm B}T\right)$, where $J_{\rm gs}$ is the degeneracy of the ground state. The probability for the system to break up one pair is proportional to $P_{\rm 1bp} = J_{\rm 1bp} \exp\left[-\left(E_{\rm gs} + \Delta_{L_F}\right)/k_{\rm B}T\right]$, since Δ_{L_F} is the first pair-breaking energy. Here, $J_{\rm 1bp}$ is the total number of states with one broken pair. An appreciable contribution of states with one broken pair to the specific heat appears when $P_{\rm 1bp}$ becomes comparable to $P_{\rm gs}$, i.e. at a temperature

$$k_{\rm B}T^* = \frac{\Delta_{L_F}}{\ln(J_{\rm 1bp}/J_{\rm gs})}. \tag{300}$$

The degeneracy of states, which correspond to the first intralevel pair breaking (at $g_L = 0$), exceeds that for the ground state by a factor of $2^2 C_2^{2L+1}$. In this connection, one could recall that the energy of the first pair-hole excitation ($g_L = 1$) coincides with that of the first pair-breaking excitation (see Eqs. (295) and (296)). It is worth noting however that an increase in the degeneracy of states due to the first pair-hole excitation (from the ground state) is characterized by the factor $(C_1^{2L+1} - 1)$ which is much smaller than $2^2 C_2^{2L+1}$ in the case of $L \gg 1$. That is why the pair-hole excitations are much less important – as compared to the first pair-breaking excitation – for the initial stage of the fast increase of C with T. So, in the case of $G < \epsilon_1/2$, the temperature T^* is determined by the first intralevel pair breaking on the level $L = L_F$.

5.5. Parity effects

The qualitative behavior of $C(T)$ is similar for spherical systems with odd and even numbers of electrons. Nevertheless, two observations can be made from Figs. 44 and 45: (i) for odd numbers of electrons a fast increase of C with T takes place at higher temperatures as compared to the even case; (ii) a shoulder, which is clearly seen on the curves of $C(T)$ for the system with an even number of electrons is not pronounced for odd numbers of electrons.

The shoulder of $C(T)$, indicated by the arrows in Figs. 44 and 45, corresponds to the first pair-breaking excitation. The appearance of this shoulder arises from the fact that the relative increase of D_δ due to the first pair breaking is significantly larger than that for further pair-breaking transitions. For systems with an even number of electrons and $G < \epsilon_1/2$, the increase of D_δ can be characterized by the factor $\sim 4C_2^{2L_F+1} \approx 8L_F^2$. In the odd case, due to the presence of one unpaired electron in the ground state, the ground state degeneracy is $2C_1^{2L_F+1}$, so that the relative increase of D_δ becomes $4C_3^{2L_F+1}/C_1^{2L_F+1} \approx 8L_F^2/3$. This is 3 times smaller than in the even case. Also for $G > \epsilon_1/2$, a jump of D_δ due to the first pair breaking is appreciably less pronounced for systems with odd numbers of electrons as compared to those with even numbers. This parity effect in the specific heat also translates into a parity effect for the critical temperature derived from $C(T)$.

Moreover, for $G < \epsilon_1/2$ only the Fermi level is involved in the pairing correlations, but at $G > \epsilon_1/2$, the situation is a bit more complicated. In this case, approximately $\mu = 2G/\epsilon_1$ single-particle energy levels around the level $L = L_F$ are partially occupied in the ground state configuration. Moreover, for the interaction strength G significantly larger than $\epsilon_1/2$, interlevel pair-breaking excitations (within the aforementioned set of μ single-electron energy levels) have energies close to those of intralevel pair-breaking excitations. Taking the above into account, we can approximate, for the even case

$\ln(J_{1bp}/J_{gs})$ as $\ln(4C_2^{\mu(2L_F+1)}) \approx \ln(8L_F^2\mu^2)$. As discussed in the previous paragraph, the degeneracy ratio in the case of an odd system is three times smaller, so that the expression (300) becomes

$$k_B T^*_{even} \approx \frac{(2L_F+1)G}{\ln(8L_F^2\eta^2)}, \tag{301}$$

with $\eta = \max[1, 2G/\epsilon_1]$ for even systems, and for the odd case

$$k_B T^*_{odd} \approx \frac{2L_F G}{\ln(8L_F^2\eta^2/3)}. \tag{302}$$

This shows that (at a fixed $L_F \gg 1$): $(T^*_{odd} - T^*_{even})/T^*_{even} \approx \ln 3/\ln(8L_F^2\eta^2)$. So, the characteristic temperature increases due to the presence of an unpaired electron in the ground state. As we discussed above, this result is related to the fact that the many-electron ground state in an odd MEB is highly degenerate due to degeneracy of single-electron energy states with a definite L. In this connection, it may be of some relevance to recall one of our results for grains with degenerate single-electron states in the interaction band (see App. A in [118]). For those grains with an odd number of electrons, degeneracy of the many-electron ground state leads to a re-entrant behavior of magnetization: slightly above the "critical magnetic field", an increase of T from zero results in a transition from the fully spin polarized ("normal") state to the maximally paired state (see Fig. 7(a) and the related text in [118]).

In Fig. 46 the critical temperature is shown for the case of multielectron bubbles with N electrons, subjected to different pressures (the higher the pressure, the more compressed the bubble is and the smaller the radius). In the bottom panel for this figure, the parity effect is shown through $(T^*_{odd} - T^*_{even})/T^*_{even}$. This relative difference in the odd–even critical temperatures is seen to vary slowly as a function of an increasing number of electrons in a bubble.

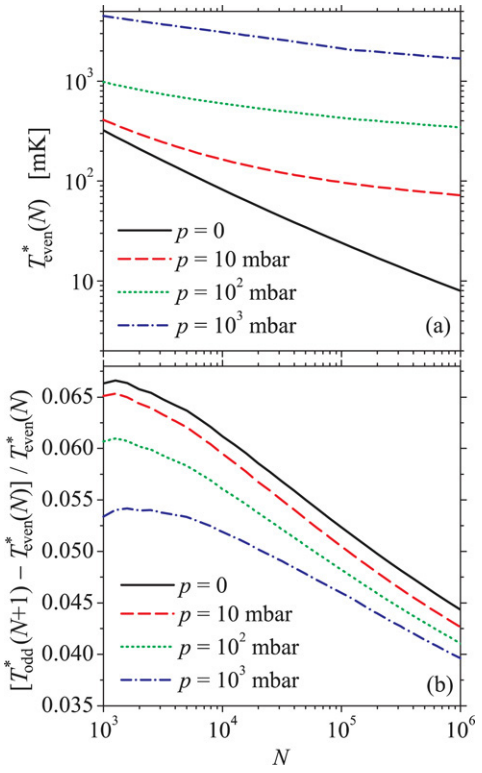

Fig. 46. In the top panel, estimates for the critical temperature for pair formation is shown as a function of the number of electrons for multielectron bubbles in helium subjected to different pressures. The bottom panel shows the parity effect in the critical temperature. From Ref. [120].

5.6. Ginzburg–Landau on the sphere

In the preceding sections, we investigated the microscopic theory describing the state with (superconducting) pairing correlations. Alternatively, a description based on interpreting the superconducting order parameter as a macroscopic wave function can be set up, allowing to set up a hydrodynamic theory for the dynamics of the superconductor. This description is more suitable to describe the superconducting dynamics (such as vortex dynamics), and can be readily applied to superconducting nanoshells with finite thickness.

The superconducting state is described by a macroscopic wave function $\psi = |\psi|\, e^{i\phi}$ whose modulus squared represents the density of pairs. The gradient of the phase ϕ is proportional to the pair velocity field. The macroscopic wave function couples to the vector potential $\mathbf{A}$ of the magnetic field. The Ginzburg–Landau equations which ψ and $\mathbf{A}$ have to satisfy are

$$\begin{cases} [\nabla_{\mathbf{r}} - i\mathbf{A}(\mathbf{r})]^2\, \psi(\mathbf{r}) + 2\kappa^2 \psi(\mathbf{r})[1 - |\psi(\mathbf{r})|^2] = 0 \\ \nabla \times (\nabla \times \mathbf{A}(\mathbf{r})) = 2\,|\psi(\mathbf{r})|^2\, [\nabla_{\mathbf{r}}\phi - \mathbf{A}(\mathbf{r})]\,. \end{cases} \tag{303}$$

Here, $\kappa = \lambda_L/\xi$ is the ratio of London penetration depth λ_L and the coherence length ξ. The boundary condition states that there is no net superflow out of the superconductor:

$$[\nabla_{\mathbf{r}} - i\mathbf{A}(\mathbf{r})]\, \psi(\mathbf{r})|_{n,\text{boundary}} = 0. \tag{304}$$

Here, we used units that simplify the equations, namely $\sqrt{2}\lambda_L$ for lengths, $\phi^2/[4(2\pi)^2\mu\lambda_L^4]$ for energy densities (where $\phi = h/(2e)$ is the fluxoid quantum and μ is the permeability). The vector potential is expressed in units $\phi/[2\pi\sqrt{2}\lambda_L]$. In these units, the difference in Gibbs free energy density between normal and superconducting state is:

$$g_s - g_n = \frac{1}{2}(\mathbf{B}(\mathbf{r}) - \mathbf{H}(\mathbf{r}))^2 - \kappa^2\, |\psi(\mathbf{r})|^4 \tag{305}$$

where $\mathbf{H}(\mathbf{r})$ is the externally applied magnetic field and $\mathbf{B} = \mu(\mathbf{M} + \mathbf{H})$ is the magnetic induction field ($\mathbf{M}$ is the magnetization).

5.6.1. Thin nanoshells

In a nanoshell of thickness smaller than the penetration depth, the variation of $\psi(\mathbf{r})$ can be neglected in the radial direction in the shell. When a magnetic field parallel to the z direction is present, the axial symmetry allows us to set

$$\mathbf{A} = A_\phi(r, \theta)\mathbf{e}_\phi; \tag{306}$$

then this can indeed describe the induction field $\mathbf{B}$ when this lies in the r, θ plane. We have $\mathbf{B} = B_r \mathbf{e}_r + B_\theta \mathbf{e}_\theta$ with

$$B_r = \frac{1}{r\sin\theta}\frac{\partial(A_\phi \sin\theta)}{\partial\theta} \tag{307}$$

$$B_\theta = -\frac{1}{r}\frac{\partial(rA_\phi)}{\partial r} \tag{308}$$

and $B_\phi = 0$ as it should be. Moreover, this gauge for the vector potential immediately satisfies the GL boundary condition $\mathbf{A}\cdot\mathbf{n} = 0$ since $\mathbf{n} = \mathbf{e}_r$. If no vortex is present, we need to solve

$$\nabla \times \nabla \times \mathbf{A} = -2\,|\psi|^2\,\mathbf{A} \tag{309}$$

both in the regions inside ($|\psi|^2 = 1$) and outside ($|\psi|^2 = 0$) the sphere. The solution outside the shell is

$$A_\phi^{\text{out}} = \frac{\mu H}{2}(r + c_1 r^{-2})\sin\theta. \tag{310}$$

In the region inside the shell we get

$$A_\phi^{\text{shell}} = \left[c_2\frac{\cosh(\sqrt{2}r) - \sqrt{2}r\sinh(\sqrt{2}r)}{2r^2} + c_3\frac{\sqrt{2}r\cosh(\sqrt{2}r) - \sinh(\sqrt{2}r)}{2r^2}\right]\sin\theta. \tag{311}$$

Finally, in the region inside the shell the result is

$$A_\phi^{\text{in}} = c_4 r\sin\theta. \tag{312}$$

Here, c_1, c_2, c_3 and c_4 are integration constants; in the limit of a very thin shell with radius R, they become

$$c_1 \to 0 \tag{313}$$

$$c_2 \to -2R\cosh(\sqrt{2}R) + (\sqrt{2} + \sqrt{2}R^2)\sinh(\sqrt{2}R) \tag{314}$$

$$c_3 \to (\sqrt{2} + \sqrt{2}R^2)\cosh(\sqrt{2}R) - 2R\sinh(\sqrt{2}R) \tag{315}$$

$$c_4 \to 1. \tag{316}$$

This gives us the same solution for A in all regions, namely

$$A_\phi = \frac{\mu H}{2} r\sin\theta. \tag{317}$$

This means that for a thin shell, the external field is not perturbed by the presence of the shell and the magnetic field penetrates the superconductor, as we expect. The difference in Gibbs free energy between the superconducting state with order parameter ψ and the non-superconducting state in the same external magnetic field $\mathbf{H}$ is given by the sum of the following to terms:

$$\Delta G_\Psi = \int \mathrm{d}\mathbf{x}\left\{\left|\left(\nabla - \mathrm{i}\frac{\mathbf{A}}{A_0}\right)\psi\right|^2 - 2\kappa^2\,|\psi|^2\left(1 - \frac{1}{2}\,|\psi|^2\right)\right\} \tag{318}$$

$$\Delta G_{\mathrm{B}} = \frac{1}{2}\int \mathrm{d}\mathbf{x}\,(\mathbf{B} - \mu\mathbf{H})^2\,. \tag{319}$$

The first line represents the lowering in energy due to the order parameter, and the second line represent the change in magnetic energy due to the magnetization.

5.6.2. Critical magnetic field

First, we consider the case of uniform order parameter ($\psi = f$ with f constant), and calculate the difference in Gibbs free energy between the superconducting and the normal state:

$$\begin{aligned}\Delta G &= 2\pi f^2\int_0^\pi \mathrm{d}\theta\sin\theta\left\{\left(-\frac{1}{2}\mu H R^2\sin\theta\right)^2 - 2(\kappa R)^2\left(1 - \frac{1}{2}f^2\right)\right\}\\ &= \frac{2\pi f^2}{3}(\mu H R^2)^2 - 4\pi(\kappa R)^2(2f^2 - f^4).\end{aligned} \tag{320}$$

This is minimized as a function of f for f satisfying

$$\frac{4\pi f}{3}(\mu H R^2)^2 - 4\pi(\kappa R)^2(4f - 4f^3) = 0. \tag{321}$$

This solves for $f = 0$ or

$$\frac{1}{3}(\mu H R^2)^2 - 4(\kappa R)^2(1 - f^2) = 0 \tag{322}$$

$$\Leftrightarrow \frac{1}{12}\left(\frac{\mu H R}{\kappa}\right)^2 = (1 - f^2)$$

$$\Leftrightarrow \sqrt{1 - \frac{1}{12}\left(\frac{\mu H R}{\kappa}\right)^2} = f. \tag{323}$$

This results in a critical magnetic field given by

$$\mu H_c = \sqrt{12}\frac{\kappa}{R}. \tag{324}$$

With the magnetic field (324) the energy is

$$\begin{aligned}\Delta G = {} & \frac{2\pi}{3}\left[1 - \frac{1}{12}\left(\frac{\mu H R}{\kappa}\right)^2\right](\mu H R^2)^2\\ & - 4\pi(\kappa R)^2\left(2\left[1 - \frac{1}{12}\left(\frac{\mu H R}{\kappa}\right)^2\right]\right.\\ & \left. - \left[1 - \frac{1}{12}\left(\frac{\mu H R}{\kappa}\right)^2\right]^2\right)\end{aligned}$$

then

$$\Delta G = \begin{cases} -4\pi(\kappa R)^2\left(1 - \dfrac{H^2}{H_c^2}\right)^2 & \text{for } H < H_c\\ 0 \quad \text{for } H > H_c. \end{cases} \tag{325}$$

This indeed remains negative as long as $H < H_c$. It becomes zero for $H = H_c$, and since the order parameter vanishes above H_c, it remains zero afterwards.

5.6.3. Vortex state

If we assume that the vortex is parallel to the z-axis (and thus to the magnetic field), and that it is located at the poles of the sphere, the axial symmetry is still satisfied. We can write the order parameter as

$$\psi = f(\theta)\mathrm{e}^{\mathrm{i}m\phi} \tag{326}$$

with m equal to the number of vortex quanta. For a single quantum of vorticity, we have $m = \pm 1$, and f can no longer be independent of θ. Indeed, we need to impose $f(\theta = 0, \pi) = 0$. The simplest way to achieve this is by setting $f(\theta) = \sin\theta$ — which would be the ground state solution of a free particle on a sphere under the given condition $f(\theta = 0, \pi) = 0$. It will be valid for spheres with $R < \xi$. However, for spheres with $R > \xi$, we expect $f(\theta)$ to be different from 1 only in a region of size ξ around the poles. So, the ratio R/ξ or $R\kappa$ will be of importance for the form of $f(\theta)$.Then,

$$|\psi| = f\sin(\theta) \tag{327}$$

$$\nabla|\psi| = \frac{1}{r}\frac{\partial f}{\partial\theta}\mathbf{e}_\theta = \frac{1}{r}\cos(\theta)\mathbf{e}_\theta \tag{328}$$

$$\nabla\varphi = \frac{1}{r\sin\theta}\mathbf{e}_\phi. \tag{329}$$

The vector potential will be influenced by the current flowing around. Nevertheless, we hope that this gives only a small extra contribution to $\mathbf{A}$, and use expression (317). The difference in Gibbs free energies of the normal and superconducting states becomes

$$\begin{aligned}\Delta G &= 2\pi f^2 R^2 \int_0^\pi \mathrm{d}\theta \sin\theta \left\{ \frac{\cos^2(\theta)}{R^2} \right. \\ &\quad + \sin(\theta)^2 \left(\frac{1}{R\sin\theta} - \frac{\mu H}{2} R\sin\theta\right)^2 \\ &\quad \left. - 2(\kappa R)^2 \sin^2(\theta)\left(1 - \frac{1}{2}f^2\sin^2(\theta)\right)\right\} \qquad (330) \\ &= 2\pi f^2 \left\{ \frac{2}{3} + \left(2 + \frac{4}{15}(\mu H R^2)^2 - \frac{4}{3}(\mu H R^2)\right) \right. \\ &\quad \left. - 2(\kappa R)^2\left(\frac{4}{3} - \frac{8}{15}f^2\right)\right\}. \qquad (331)\end{aligned}$$

From this, we can extract a optimal f:

$$\begin{aligned}&2\left(\frac{8}{3} + \frac{16}{15}\left(\frac{\mu H R^2}{2}\right)^2 - \frac{8}{3}\left(\frac{\mu H R^2}{2}\right) - \frac{8}{3}(\kappa R)^2\right) f \\ &\quad + 4(\kappa R)^2 \frac{16}{15} f^3 = 0 \\ &\Leftrightarrow \left(1 + \frac{2}{5}\left(\frac{\mu H R^2}{2}\right)^2 - \left(\frac{\mu H R^2}{2}\right) - (\kappa R)^2\right) f \\ &\quad + \frac{4}{5}(\kappa R)^2 f^3 = 0. \qquad (332)\end{aligned}$$

Then, either $f = 0$ or

$$f = \sqrt{\frac{5}{4(\kappa R)^2}\left[\left(\frac{\mu H R^2}{2}\right) + (\kappa R)^2 - 1 - \frac{2}{5}\left(\frac{\mu H R^2}{2}\right)^2\right]}. \tag{333}$$

This only has a solution for

$$\frac{5}{2R^2}\left(1 - \sqrt{\frac{8}{5}(\kappa R)^2 - \frac{3}{5}}\right) < \mu H < \frac{5}{2R^2}\left(1 + \sqrt{\frac{8}{5}(\kappa R)^2 - \frac{3}{5}}\right).$$

So, there are two critical fields,

$$\mu H_{c+} = \frac{5}{2R^2}\left(1 + \sqrt{\frac{8}{5}(\kappa R)^2 - \frac{3}{5}}\right) \tag{334}$$

$$\mu H_{c-} = \frac{5}{2R^2}\left(1 - \sqrt{\frac{8}{5}(\kappa R)^2 - \frac{3}{5}}\right). \tag{335}$$

First, we see that when $(\kappa R)^2 < \frac{3}{8}$, there is no solution. So, to have a vortex solution, the radius needs to be larger than $R > \sqrt{3/8}\kappa^{-1}$, or in SI units

$$R > \sqrt{\frac{3}{4}}\xi. \tag{336}$$

This seems acceptable, since indeed if the radius is much smaller than the healing length, making a vortex destroys too much order parameter. So, we find a first critical radius. There is a second critical radius, given by

$$1 - \sqrt{\frac{8}{5}(\kappa R)^2 - \frac{3}{5}} = 0 \Leftrightarrow \kappa R = 1. \tag{337}$$

When the radius becomes larger than $R > \sqrt{2}\xi$, then the vortex solution will be present up to a critical field

$$\mu H_c = \frac{5}{2R^2}\left(1 + \sqrt{\frac{8}{5}(\kappa R)^2 - \frac{3}{5}}\right). \tag{338}$$

When on the other hand, the radius is between those values, $\sqrt{2}\xi > R > \sqrt{\frac{3}{4}}\xi$, then also the lower critical field μH_{c-} matters: below this the vortex solution is unstable. The solution without a vortex (i.e. with constant f) may be stable though. Putting the result back in the Gibbs free energy, we get

$$\Delta G = \begin{cases} -\dfrac{\pi(\mu R^2)^4}{2(\kappa R)^2}\left[(H - H_{c+})(H - H_{c-})\right]^2 & \text{for} \\ \quad H_{c-} < H < H_{c+} \\ 0 \quad \text{for } H > H_{c+} \text{ or } H < H_{c-}. \end{cases} \tag{339}$$

This result is summarized in Fig. 47. Below the blue line, the superconducting state without vortex exists. And to the right of the black curve, the superconducting state with a vortex, $\psi = f\sin(\theta)\mathrm{e}^{\mathrm{i}\phi}$ exists. In the region where they coexist, they compete for the lowest energy. The red curve separates the region where the vortex state is stable from the region where the no-vortex state wins. At low magnetic field (blue zone) the no-vortex state exists. At higher magnetic field (green zone) the vortex state has lowest energy. Finally, in the white regions the superconductivity is destroyed and the normal state wins.

6. Conclusions

In this review, we considered various aspects of the curved, two-dimensional electron gas, focusing particularly on the electronic and vibrational properties of multielectron bubbles.

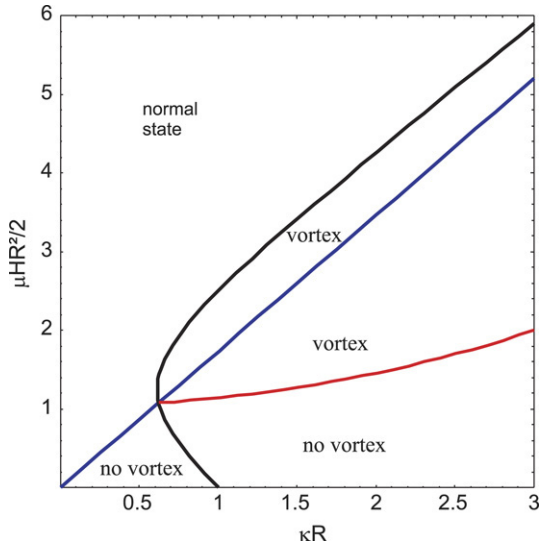

Fig. 47. Phase diagram of a spherical superconducting film, as a function of sphere radius and applied magnetic field. In the zones indicated 'no vortex', the superconducting state without vortex has the lowest energy. In regions indicated 'vortex', the vortex state has lower energy. (For interpretation of the references to colour in this figure legend, the reader is referred to the web version of this article.)

Both the electronic states and the vibrational modes of the MEB are thoroughly derived and discussed.

The modes of oscillation of the bubble are important not only for influencing the electronic properties, but also for analyzing the stability of multielectron bubbles. We have analyzed the effect of positive and negative pressure on the modes of oscillation of a multielectron bubble. We find that small negative pressures can stabilize the bubble against dynamic instability, whereas positive pressures can soften the ripplon modes. The fissioning of a MEB is studied within the liquid drop model. We found that, although a mode of deformation exists which can grow without increasing the total energy of the bubble, there is still an energy barrier present which prevents fissioning of the bubble. This barrier was explained by the intermediate shapes that the fissioning bubble has to assume in order to create a neck between the emerging fission fragment and the parent bubble. At negative pressure, when all the modes of deformation have a non-vanishing frequency, there is an additional element of stability in that there is a restoring force which counteracts small amplitude deformations. Also at zero pressure the MEB is metastable.

To investigate the basic electronic properties of the spherical two-dimensional electron gas, a second-quantization formalism based on the spherical harmonics rather than plane waves is introduced. Within this framework, the dynamic structure factor is derived in the RPA framework and both the single-particle excitations and collective excitations are analyzed for S2DEGs. The dynamic structure factor in the RPA approximation reveals collective excitations, "spherical plasmon modes", which differ from the collective modes of the flat 2DEG in that the spherical plasmon modes of the S2DEG are discrete in frequency and the smallest spherical plasmon frequency is larger than zero. When a magnetic field is present, the difference between the spherical electron gas and the flat 2DEG becomes more pronounced. In a flat 2DEG Landau levels appear, while in the spherical case Landau bands of equally spaced, doubly degenerate levels are formed. The electron density tends to collect at latitudes on the sphere that correspond to cyclotron radii. The plasmon branch also broadens. For typical multielectron bubbles with $N < 10^4$, the plasmon modes of the S2DEG lie in the far infrared, and their frequency increases with decreasing number of electrons in the MEB or with decreasing radius of the bubble, such that these novel collective modes may be detectable in forthcoming experiments on stabilized multielectron bubbles.

When vibrational modes – such as ripplons in the MEB – couple to the electronic properties of the S2DEG, this can leads to polaronic effects and to an attractive effective potential between the electrons. We have investigated the properties of ripplonic polarons in a multielectron bubble in liquid helium on the basis of the all-coupling path integral variational method. We have shown that the ripplopolaron state formed by an electron together with its accompanying deformation of the helium surface can exist in a MEB in the solid phase localizing electron charges in a Wigner lattice on a spherical surface. The ripplopolaron state in a MEB is distinct both from the usual Wigner lattice of electrons and from the Wigner lattice of ripplopolarons on a flat helium surface. It melts by dissociation of the ripplopolarons when the electrons shed their localizing dimple as the pressure on the multielectron bubble drops below a critical value. This ripplopolaron solid can melt into an electron liquid, and as the surface density is decreased this may become an electron Wigner lattice. The phase diagram for the ripplopolaron solid may be determined experimentally by measuring the vibrational spectra of the MEB while varying the pressure.

We have analyzed how the electron–ripplon interaction on a spherical surface may lead to an attractive effective electron–electron interaction and give rise to a Cooper pairing scenario. The effective Hamiltonian of the two-dimensional spherical electron system is mapped on a BCS-type Hamiltonian and typical values of energies, length scales, and interaction strengths are estimated. Richardson's method is used to investigate pairing properties of a two-dimensional spherical electron system. We find that when the condensation energy per pair is larger than the bubble energy scale $\hbar^2/(m_e R^2)$, the ground state of the system acquires unique properties that set it apart from pairing in conventional superconductors or superconducting nanograins. Moreover, the many-body eigenenergy spectrum can be calculated analytically. The resulting density of states no longer has a gap, but nevertheless a strong step-like increase occurs in the density of state as a function of the energy when the energy exceeds the pair-breaking energy. This can be used to define a critical temperature. The critical temperature reveals pronounced odd–even effects that persists for large (10^6) numbers of electrons.

In conclusion, we have shown that spherical electron systems reveal particularly interesting pairing properties, distinct from their bulk or flat-surface counterparts, combining both topological effects and confinement effects. MEBs are a

particularly pure realization of the two-dimensional electron system just as an electron film on helium forms a pure realization of a flat 2DEG.

Acknowledgments

The authors acknowledge fruitful discussions with S.N. Klimin, V.N. Fomin and V. Gladilin. This work was supported financially by the Department of Energy, Grant No. DE-FG02-ER45978, and by the Fonds voor Wetenschappelijk Onderzoek – Vlaanderen, project nos. G.0356.06, G.0115.06, G.0435.03, G.0306.00, the W.O.G. project WO.025.99N, the GOA BOF UA 2000 UA. J.T. gratefully acknowledges support of the Special Research Fund of the University of Antwerp, BOF NOI UA 2004.

References

[1] C.C. Grimes, G. Adams, Phys. Rev. B. 41 (1990) 6366.
[2] W.T. Sommer, Phys. Rev. Lett. 12 (1964) 271–273.
[3] M.A. Woolf, G.W. Rayfield, Phys. Rev. Lett. 15 (1965) 235–237.
[4] J.W. Rayleigh, Philos. Mag. 14 (1882) 184.
[5] A.P. Volodin, M.S. Khaikin, V.S. Edel'man, JETP Lett. 26 (1978) 543; Zh. Eksp. Teor. Fiz. 26 (1977) 707.
[6] R.S. Crandall, R. Williams, Phys. Lett. 34A (1971) 404.
[7] W. Wigner, Phys. Rev. 46 (1934) 1002.
[8] C.C. Grimes, G. Adams, Phys. Rev. Lett. 42 (1979) 795.
[9] R.S. Crandall, R. Williams, Phys. Rev. A 5 (1972) 2183–2190.
[10] M.W. Cole, M.H. Cohen, Phys. Rev. Lett. 23 (1969) 1238–1241.
[11] L.P. Gor'kov, D.M. Chernikova, JETP Lett. 18 (1973) 68; Zh. Eksp. Teor. Fiz. 18 (1973) 119.
[12] U. Albrecht, P. Leiderer, Europhys. Lett. 3 (1987) 705.
[13] V.B. Shikin, JETP Lett. 27 (1978) 39.
[14] M.M. Salomaa, G.A. Williams, Phys. Rev. Lett. 47 (1981) 1730.
[15] K.W.-K. Shung, F.L. Lin, Phys. Rev. B 45 (1992) 7491.
[16] A.A. Artem'ev, A.G. Khrapak, I.T. Yakubov, Fiz. Nizk. Temp. 11 (1985) 1011; Sov. J. Low Temp. Phys. 11 (1985) 10.
[17] J. Tempere, I.F. Silvera, J.T. Devreese, Phys. Rev. Lett. 87 (2001) 275301.
[18] H.J. Marus, Q. Xiong, Phys. Rev. Lett. 63 (1989) 1078.
[19] P.M. Platzman, H. Fukuyama, Phys. Rev. B 19 (1974) 3150.
[20] F.M. Peeters, P.M. Platzman, Phys. Rev. Lett. 50 (1983) 2021.
[21] F.M. Peeters, in: E.Y. Andrei (Ed.), Two-dimensional Electron Systems, Kluwer Academic Publishers, Dordrecht, The Netherlands, 1997, p. 17.
[22] V.M. Bedanov, G.V. Gadiyak, Y.E. Lozovik, Phys. Lett. A 109 (1985) 289.
[23] V.M. Bedanov, F.M. Peeters, Phys. Rev. B 49 (1994) 2667–2676.
[24] V.B. Shikin, Sov. Phys. JETP 33 (1971) 387.
[25] A. Pérez-Garrido, M.J.W. Dodgson, M.A. Moore, Phys. Rev. B 56 (1997) 3640.
[26] M. Bowick, A. Cacciuto, D.R. Nelson, A. Travesset, Phys. Rev. Lett. 89 (2002) 185502.
[27] I.F. Silvera, Bull. Amer. Phys. Soc. 46 (2001) 1016.
[28] T.R. Brown, C.C. Grimes, Phys. Rev. Lett. 29 (1972) 1233.
[29] H. Etz, W. Gombert, W. Idstein, P. Leiderer, Phys. Rev. Lett. 53 (1984) 2567.
[30] E.R. Generazio, R.W. Reed, J. Low Temp. Phys. 56 (1984) 355.
[31] D.L. Dexter, W.B. Fowler, Phys. Rev. 183 (1969) 307.
[32] M. Pi, R. Mayol, M. Barranco, V. Grau, Phys. Rev. B 73 (2006) 064502.
[33] M.M. Salomaa, G.A. Williams, Phys. Scripta T4 (1983) 204.
[34] I.F. Silvera, J. Blanchfield, J. Tempere, Phys. Status Solidi B 237 (2003) 274.
[35] H.J. Maris, Q. Xiong, Phys. Rev. Lett. 63 (1989) 1078.
[36] S.T. Hannahs, G.A. Williams, M.M. Salomaa, 1995 IEEE Ultrasonics Symposium Proceedings, vol. 1, 1995, p. 2.
[37] N. Bohr, J.A. Wheeler, Phys. Rev. 56 (1939) 426–450.
[38] J. Tempere, I.F. Silvera, J.T. Devreese, Phys. Rev. B 67 (2002) 35402.
[39] J. Tempere, I.F. Silvera, S. Rekhi, J.T. Devreese, Phys. Rev. B 70 (2004) 224303.
[40] M.S. Plesset, A. Prosperetti, Ann. Rev. Fluid Mech. 9 (1977) 145.
[41] M.P. Brenner, S. Hilgenfeldt, D. Lohse, Rev. Modern Phys. 74 (2002) 425–484.
[42] R.D. Averitt, D. Sarkar, N.J. Halas, Phys. Rev. Lett. 78 (1997) 4217.
[43] S.J. Oldenburg, R.D. Averitt, S.L. Westcott, N.J. Halas, Chem. Phys. Lett. 288 (1998) 243.
[44] S.L. Westcott, S.J. Oldenburg, T.R. Lee, N.J. Halas, Langmuir 14 (19) (1998) 5396.
[45] S.J. Oldenburg, J.B. Jackson, S.L. Westcott, N.J. Halas, Appl. Phys. Lett. 75 (1999) 2897.
[46] E. Prodan, P Nordlander, Nano Lett. 3 (4) (2003) 543.
[47] E. Prodan, C. Radloff, N.J. Halas, P. Nordlander, Science 302 (2003) 419.
[48] S.J. Oldenburg, S.L. Westcott, R.D. Averitt, N.J. Halas, J. Chem. Phys. 111 (1999) 4729.
[49] D.P. O'Neal, L.R. Hirsch, N.J. Halas, J.D. Payne, J.L. West, Cancer Lett. 209 (2004) 171.
[50] E. Prodan, P. Nordlander, J. Chem. Phys. 120 (11) (2003) 5444.
[51] Y.A. Vlasov, V.N. Astratov, O.Z. Karimov, A.A. Kaplyanskii, V.N. Bogomolov, A.V. Prokofiev, Phys. Rev. B 55 (1997) R13357.
[52] Lord J.W. Rayleigh, Proc. R. Soc. Lond. 29 (1879) 71.
[53] Y. Sasaki, Y. Nishina, M. Sato, K. Okamura, Phys. Rev. B 40 (1989) 1762.
[54] M.W. Cole, Phys. Rev. B 2 (1970) 4244.
[55] P. Lenz, D.R. Nelson, Phys. Rev. Lett. 87 (2001) 125703.
[56] S.A. Jackson, P.M. Platzman, Phys. Rev. B 24 (1981) 499.
[57] Hipólito, G.A. Farias, N. Studart, Surf. Sci. 113 (1982) 394.
[58] J. Tempere, S.N. Klimin, I.F. Silvera, J.T. Devreese, Eur. Phys. J. B 32 (2003) 329.
[59] J. Tempere, V. Gladilin, I.F. Silvera, J.T. Devreese, Phys. Rev. B 72 (2005) 094506.
[60] J. Tempere, I.F. Silvera, J.T. Devreese, Phys. Rev. B 65 (2002) 195418.
[61] L. Fetter, J.D. Walecka, Quantum Theory of Many-Particle Systems, McGraw-Hill, New York, 1971.
[62] G.D. Mahan, Many-Particle Physics, Kluwer-Plenum, Dordrecht, 2000.
[63] T. Inaoka, Surf. Sci. 273 (1992) 191.
[64] D. Pines, The Many-Body Problem, Benjamin, New York, 1961.
[65] C. Niven, Philos. Trans. Roy. Soc. London 171 (1880) 117.
[66] J. Tempere, I.F. Silvera, J.T. Devreese, J. Low Temp. Phys. 138 (2005) 457.
[67] D.N. Aristov, Phys. Rev. B 59 (1999) 6368.
[68] M. Encinosa, Phys. Rev. A 73 (2006) 012102.
[69] A.I. Goker, P. Nordlander, J. Phys. – Condens. Matter 16 (2004) 8233–8241.
[70] A nice review can be found in Theory and Computation of Spheroidal Harmonics with General Arguments, Peter Falloon, University of Western Australia, 2001.
[71] E.Y. Andrei (Ed.), Two-Dimensional Electron Systems on Helium and Other Cryogenic Substrates, Kluwer Acad. Publ., Dordrecht, The Netherlands, 1997.
[72] V.B. Shikin, Zh. Eksp. Teor. Fiz. 58 (1970) 1140; Sov. Phys. JETP 31 (1970) 936.
[73] S.A. Jackson, P.M. Platzman, Phys. Rev. B 25 (1982) 4886.
[74] G.E. Marques, N. Studart, Phys. Rev. B 39 (1989) 4133.
[75] C.Y. Chen, P.W. Jin, D.L. Lin, R. Chen, Phys. Rev. B 50 (1994) 3129.
[76] G.A. Farias, R.N. Filho, F.M. Peeters, N. Studart, Phys. Rev. B 64 (2001) 104301.
[77] F.F. Mende, Yu.Z. Kovdrya, V.A. Nikolaenko, Fiz. Nizk. Temp. 11 (1985) 646; Sov. J. Low Temp. Phys. 11 (1985) 355.
[78] E.Y. Andrei, Phys. Rev. Lett. 52 (1984) 1449.
[79] D.S. Fisher, B.I. Halperin, P.M. Platzman, Phys. Rev. Lett. 42 (1979) 798.
[80] Yu.P. Monarkha, V.B. Shikin, Fiz. Nizk. Temp. 9 (1983) 913; Sov. J. Low Temp. Phys. 9 (1983) 471.
[81] M.I. Dykman, Yu.G. Rubo, Phys. Rev. Lett. 78 (1997) 4813.

[82] Yu.P. Monarkha, K. Kono, J. Phys. Soc. Japan 74 (2005) 960.
[83] S. Yusel, L. Menna, E.Y. Andrei, Phys. Rev. B 47 (1993) 12672.
[84] K. Shirahama, K. Kono, Phys. Rev. Lett. 74 (1995) 781.
[85] V.E. Syvokon, Yu.Z. Kovdrya, K.A. Nasyedkin, J. Low Temp. Phys. 144 (2006) 35.
[86] K. Shirahama, Yu.P. Monarkha, K. Kono, Phys. Rev. Lett. 93 (2004) 176805.
[87] S.N. Klimin, V.M. Fomin, 1, J. Tempere, I.F. Silvera, J.T. Devreese, Solid State Commun. 126 (2003) 409.
[88] J. Tempere, S.N. Klimin, I.F. Silvera, J.T. Devreese, Eur. Phys. J. B 32 (2003) 329.
[89] J. Tempere, I.F. Silvera, J.T. Devreese, Physica E 22 (2004) 771.
[90] I.F. Silvera, H. Kim, J. Tempere, J. Devreese, J. Low Temp. Phys. 139 (2005) 495.
[91] R.P. Feynman, Phys. Rev. 97 (1955) 660;
R.P. Feynman, A.R. Hibbs, Quantum Mechanics and Path Integrals, McGraw-Hill, New York, 1965.
[92] H. Falakshahi, X. Waintal, Phys. Rev. Lett. 94 (2005) 046801.
[93] B. Tanatar, T. Hakioglu, Solid State Commun. 88 (1993) 115.
[94] G. Rastelli, S. Ciuchi, Phys. Rev. B 71 (2005) 184303.
[95] K.R. Atkins, Liquid Helium, Cambridge University Press, London, 1959.
[96] P.M. Platzman, H. Fukuyama, Phys. Rev. B 10 (1974) 3150.
[97] V.B. Shikin, Yu.P. Monarkha, Zh. Eksp. Teor. Fiz. 65 (1973) 751; Sov. Phys. JETP 38 (1973) 373.
[98] H. Fröhlich, Adv. Phys. 3 (1954) 325.
[99] S.A. Jackson, F.M. Peeters, Phys. Rev. B 30 (1984) 4196.
[100] S. Fratini, P. Quémerais, Eur. Phys. J. B 14 (2000) 99;
S. Fratini, P. Quémerais, Eur. Phys. J. B 29 (2002) 41.
[101] F. Lindemann, Z. Phys. 11 (1910) 609.
[102] C.M. Care, N.H. March, Adv. Phys. 24 (1975) 101.
[103] H. Ikezi, R.W. Gianetta, P.M. Platzman, Phys. Rev. B 25 (1982) 4488.
[104] S.N. Klimin, V.M. Fomin, F. Brosens, J.T. Devreese, Phys. Rev. B 69 (2004) 235324.
[105] J.J. Thomson, Philos. Mag. 7 (1904) 237.
[106] D.R. Nelson, B.I. Halperin, Phys. Rev. B 19 (1979) 2457.
[107] G. Deville, et al., Phys. Rev. Lett. 53 (1984) 588.
[108] R.E. Glover, M. Tinkham, Phys. Rev. 104 (1956) 884.
[109] H. Meissner, R. Zdanis, Phys. Rev. 113 (1959) 1435–1445.
[110] V.V. Moshchalkov, L. Gielen, C. Strunk, R. Jonckheere, X. Qiu, C. Van Haesendonck, Y. Bruynseraede, Nature 373 (1995) 319.
[111] S. Burger, F.S. Cataliotti, C. Fort, F. Minardi, M. Inguscio, M.L. Chiofalo, M.P. Tosi, Phys. Rev. Lett. 86 (2001) 4447.
[112] J.K. Chin, D.E. Miller, Y. Liu, C. Stan, W. Setiawan, C. Sanner, K. Xu, W. Ketterle, Nature 443 (2006) 961–964.
[113] E. Montevecchi, J.O. Indekeu, Phys. Rev. B 62 (2000) 14359.
[114] Y.A. Genenko, H. Rauh, Appl. Phys. Lett. 82 (2003) 2115.
[115] R.W. Richardson, Phys. Lett. 3 (1963) 277.
[116] J. von Delft, A.D. Zhaikin, D.S. Golubev, W. Tichy, Phys. Rev. Lett. 77 (1996) 3189.
[117] K.A. Matveev, A.I. Larkin, Phys. Rev. Lett. 79 (1997) 3749.
[118] V.N. Gladilin, V.M. Fomin, J.T. Devreese, Phys. Rev. B 70 (2004) 144506.
[119] J.M. Román, G. Sierra, J. Dukelsky, Phys. Rev. B 67 (2003) 064510.
[120] V.N. Gladilin, J. Tempere, I.F. Silvera, J.T. Devreese, Phys. Rev. B 74 (2006) 104512.